TRANSITION METAL CARBIDES AS ACTIVE PHASE AND AS SUPPORT IN CATALYSIS: INSIGHTS FROM FIRST PRINCIPLES THEORETICAL MODELLING.

Gian Giacomo Asara

Dipòsit Legal: T 1924-2014

Gian Giacomo Asara

Transition metal carbides as active phase and as support in catalysis:

Insights from first principles theoretical modelling

Ph. D. Thesis

Supervised by:

Prof. Josep Manel Ricart Pla

Prof. Francesc Illas Riera

Grup Química Quàntica

Departament de Química Física i Inorgànica

UNIVERSITAT ROVIRA I VIRGILI

Tarragona, October 2014

Departament de Química Física i Inorgànica

Josep Manel Ricart Pla, Catedràtic del Departament de Química Física i Inorgànica de la Universitat Rovira i Virgili i Francesc Illas Riera, Catedràtic del Departament de Química Física de la Universitat de Barcelona

Fem constar que la present memòria titulada:

Transition metal carbides as active phase and as support in catalysis:

Insights from first principles theoretical modelling

Ha estat realitzada sota la nostra direcció al Departament de Química Física i Inorgànica de la Universitat Rovira i Virgili per Gian Giacomo Asara per a l'obtenció del títol de Doctor, i que acompleix els requeriments per poder optar a la Menció Internacional.

Tarragona, 10 de Octubre de 2014.

Els directors de la tesis doctoral:

Josep Manel Ricart Pla Francesc Illas Riera

Contents

Index

Chapter 1

Heterogeneous catalysis in everyday life

1.1 Introduction

Catalysis is nowadays a fundamental and essential tool for our society allowing the production and treatment of chemicals at the industrial level that will turn to be used in an incredibly high number of processes, from fertilizers production to the textile or drug industry.

It is not possible to imagine the world we know without what does not come straight from the nature but have been synthesized, treated or at least processed in an industry.

These transformations have been (in most cases) performed using a catalyst which changes the mechanism of the reaction increasing its rate (see Fig. 1).

Whereas homogeneous catalysis is mostly used for production of fine chemicals, drugs precursors and medicines,[1] intensive production of simple small organic or inorganic molecules used as solvents or reactants has been prerogative of heterogeneous catalysis from long time. Homogeneous catalysis refers to the complete miscibility of the catalyst and the reactants – for example two miscible liquids – where heterogeneous catalysis identifies multi-phase systems composed by a solid catalyst and reactants in gas or liquid state, or also by two immiscible liquids. Thousands of years before the development of the chemical industry, catalysts were already used by human beings around the world to produce food and beverages (see Fig. 2). Brewing was dated about 6000 B. C., where wine production from grapes was estimated to begin after (~3000 B. C.). In both cases the homogeneous catalyst is the yeast, the mixture of enzymes that allow the transformation of carbohydrates and sugars contained in grapes and malt into ethanol and carbon dioxide during the fermentation process. The same happens

during dough leavening. Here the increment in volume is due to the CO_2 produced in the fermentation that permeates in the porosities of the mixture.

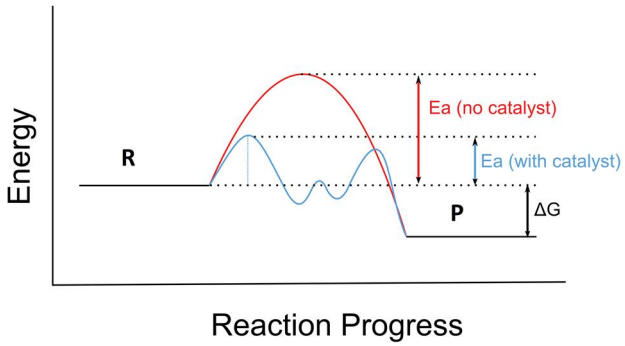

Figure 1: Energy diagram of the progress of the reaction R -> P. The catalyst changes the mechanism leading to a lower activation barrier.[2]

Catalysts are not only necessary in a variety of common processes, but they are also essential part of objects of everyday use. One nice and not so common example is the catalytic combustion of methanol in cordless hair curlers. Quartz wool coated with platinum serves as catalyst for the combustion, heating up the curler and allowing its usage.[3] Another interesting application of heterogeneous catalysts is carbon monoxide detectors, helpful to prevent accidents caused by this extremely poisonous gas. The device is composed by a fuel cell paired to an alarm. The catalytic oxidation of CO at the anode occurs when the gas diffuses in the porous platinum electrode. Sufficient concentration of gas in the air flow supply the electrons needed to activate the alarm of the detector.[3]

Important examples of heterogeneous catalyzed processes used in chemical industry are the synthesis of sulfuric acid at large scale[4] and the Haber-Bosch process, the hydrogenation of nitrogen to produce ammonia on an iron based catalyst, performed for the first time in 1913.[4] These want to be just two of a large number of processes developed at industrial scale from the 19th century.

In all cases, from brewing to sulfuric acid production, the essential role of the catalyst is always the same, resumed in Fig. 1. It gives a new more favorable path between reactants and products, where the activation energy for the rate

determining step is lower compared to the non-catalyzed reaction. The result is an increment of the reaction rate.

Figure 2: A Syrian mercenary drinking beer in the company of his Egyptian wife and child, 1350 B. C.[5]

In 1740 large scale H_2SO_4 production was performed burning niter (KNO_3) with sulfur in a glass bell jar, but a clear definition of the essential role of the potassium nitrate in the process would be given more than sixty years after, in 1806, by Clement and Desormes: "…nitric acid is only the instrument of the complete oxygenation of the sulfur: it is the base, nitric oxide, that takes the oxygen from the atmospheric air to offer it to the sulfurous acid in the state which suits it best…".[6] Nowadays sulfuric acid is one of the most important compounds made by chemical industry, whose annual world production is ~200 million tons per year.[7] It is now produced using a catalyst of vanadium oxide (V_2O_5) supported on silica and its main use reside in phosphate fertilizers production and in metal processing (e. g. manufacture of copper and zinc).

Another important chemical process with a long past history is the synthesis of ammonia from its constituents N_2 and H_2 which is called "Haber process". This compound comes second after sulfuric acid as the chemicals with larger tonnage per year. The most important purpose is (again) the production of fertilizers, which adsorb more than 80% of the total world production, estimated to be about 140 million tons per year. The Haber process was introduced in 1913, being one of the first examples where the thermodynamic knowledge led scientists to some practical industrial solution.[8] In fact, although the overall process is exothermic,

very high pressure are needed due to the stability of the N-N bond and the high fugacity of hydrogen. The original catalyst used by Haber was iron oxide (Fe_3O_4), but now much work has been done seeking for promoters and alternative catalysts. In this sense graphite supported ruthenium seems one promising possible substituent.[7]

1.2 From industrial catalysts to virtual models: rational design versus trial and error procedure.

Fermentation was discovered long time before the development of the concepts of chemical reactions and catalysis.

After Berzelius formulates the first definition of catalysis in 1836[9] and Sabatier qualitatively defined a "good" and a "bad" heterogeneous catalyst[10] long time have to pass until catalytic reactions were performed with a deep knowledge of the atomistic details of the transformation occurring and only recently it become possible to explain how matter is arranged from the subatomic level to atoms and molecules.

For centuries "recipes" were obtained only by serendipity or with many trials and errors, but obviously these procedures do not offer a clear way to improve the production of a certain compounds. Nowadays scientists have deep knowledge of how atoms form molecules and experimental techniques actually allow "seeing" the atomic detail of many chemical systems. Unfortunately real systems are by far too difficult to study and their complexity does not allow distinguish between characteristics that are of crucial importance for the chemical activity and those who are not. In this case it is hard to obtain the necessary information for a systematic improvement of catalyst and increase its activity.

Industrial catalysts are often composed by some noble metal nanoparticle (NMNP) dispersed on a matrix (some metal or metal oxide). The noble metal is the active phase of the catalyst where the reaction occurs, but it cannot just be used alone, because of its extremely high price, and often because the activity depends from both structural and electronic nano-size effects. For these reasons in most cases a support is used, mostly composed by a metal oxide such cerium oxide (CeO_2), silica (SiO_2), titania (TiO_2) or alumina (Al_2O_3) nanoparticles exposing all kind of facets and defects.[4] The support can be an active catalyst itself, a promoter of the chemical reaction of interest or an inhibitor of some side reactions, but also just an inert matrix on which NMNPs are dispersed.

Promotion or inhibition depends of the influence of the support on the NMNPs, allowing just specific active conformations or modifying the electronic structure of the system. Supports inhibit unwanted side reactions (de)stabilizing important intermediates. Sometimes the interaction with the support largely affects the catalytic properties of the metal by changing both structural and electronic properties of the NMNP and leading to an increment (or a reduction) of its catalytic activity. This is commonly referred as strong metal-support interaction (SMSI).[11,12]

The goal of the investigations in heterogeneous catalysis is on one side to discover new active catalysts for the production of some valuable and on the other, understand which relation exists between structural and electronic properties of the real catalysts and its activity. Experiments are performed on model catalysts in order to shed light on these points, and advanced computational techniques are employed to study reactions in a "virtual" laboratory.

Model catalysts are normally composed by a support material, where well-determined surfaces are grown (called *single crystal*), on which NMNPs are deposited.

A variety of surface sensitive techniques are used to identify the structure of the surface, presence of possible defects, height, size and shape of the NMNPs. On this well-defined system, reactions are performed in ultra-high vacuum (UHV) conditions, obtaining information about adsorption sites and energies, nature of reaction intermediates, products and by-products. Information will be useful for the "real world" catalysis elucidating the importance of a certain characteristic in spite of others. However interpretation of experimental results is not easy, single crystal growth is an expensive process and sometimes important information cannot be obtained without using plenty of different instruments. For this reason it is nowadays common to support experiments with computer simulations, where the model catalyst is virtually recreated using several approximations to reproduce as much as possible the real physical and chemical properties of the system. In this way (within the error of the approximations used) it is possible to access easily to information that are impossible to obtain experimentally and unravel experimental controversies. Also, the always higher accuracy of the available computational techniques allows *predicting* trends for the catalytic activity obtained screening a number of similar but different chemical systems, with just a fraction of the money needed to synthesize and study experimentally each model.

A class of compounds subject of an intense screening in the last decade are transition metal carbides (TMC), main subject of the next section and of this manuscript.

1.3 Systems under study: Noble metals supported by early Transition Metal Carbides (TMC)

The carbides of the *early* transition metals exhibit chemical and catalytic properties that in many aspects are very similar to those of expensive noble metals.[13] This new important discovery comes from the landmark work of Levy and Boudart showing that the catalytic properties of tungsten carbide (WC) are similar to those of Pd or Pt in the conversion of n-pentane to iso-pentane.[14] This discovery triggered plenty of experimental and theoretical studies unrevealing their unique catalytic properties. Indeed TMC can be considered a possible substituent of expensive noble metals used in many industrial reactions not only for their low price but because of their peculiar chemical properties that make their usage even more convenient.

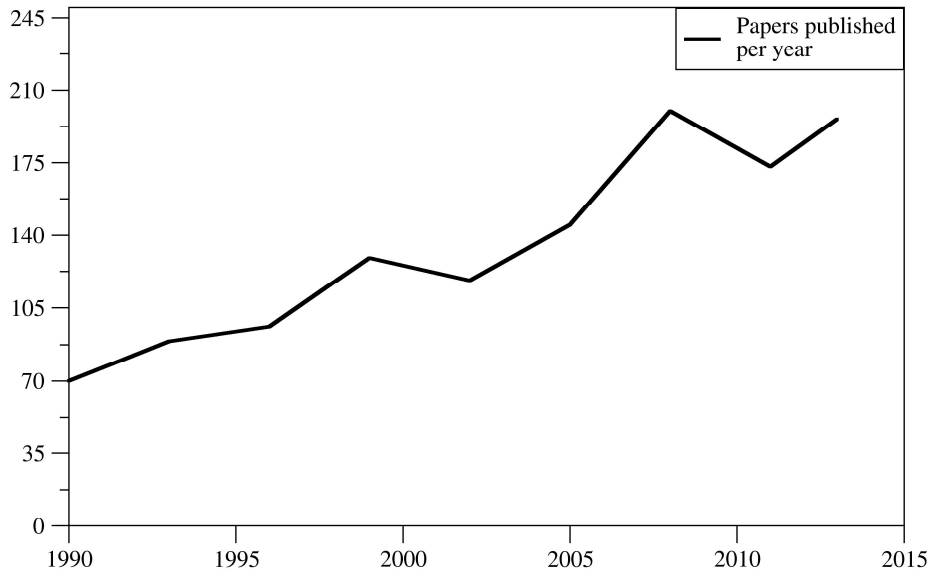

Figure 3: Papers published per year containing the word "transition metal carbide". Data from Web of Science.

1.4 TMC catalysis

The catalytic properties of many possible TMC combinations have been extensively and systematically studied in the last decade, with numerous experimental and theoretical works (see Fig. 3). A number of important reactions like alcohol conversion, hydrogenation of olefins and many others demonstrated that these compounds are suitable for application in industrial processes.[15,16,17] By way of example it will be described some studies performed on several TMC.

Molecular oxygen adsorption and dissociation on the (001) surface of carbides of groups IV-VI was studied by Viñes et al.[18] These authors found two different adsorption sites with similar adsorption energy where O_2 bridges two surface metal (M) atoms or it is placed directly on top of a surface metal atom. Just on δ-MoC the bridge adsorption between surface Mo is largely preferred. In the same work a different preferred reaction paths leading to O_2 dissociation have been found depending on the TMC considered (TM = Ti, Zr, Hf, V, Nb, Ta, Mo). On group IV TMC at low temperatures O_2 dissociation can only occur via one mechanism from an M-M bridge situation leading to a final state where O atoms are adsorbed on 3-fold hollow sites neighboring two M and one C surface atoms (MMC). At high temperatures the same products can be obtained beginning from an on top molecular adsorption situation. For the rest of the carbides only paths from on-top adsorption structures leading to products where oxygen atoms interact directly with surface metals or occupying MMC sites are possible. The calculated rate constants reveal that TMCs of groups IV and V are easy to oxidize whereas this is especially difficult for δ-MoC.

Later on, Zhang et al.[19] focused on the surface chemistry of TiC and VC (100) revealing differences and important kinetic effects introduced by one additional d electron of the V atoms.

Another interesting reaction deeply investigated on clean TMC is the water gas shift reaction (WGSR) that converts water and carbon monoxide to carbon dioxide and molecular hydrogen. Rodriguez et al.[20] studied the reaction on the clean (001) surface of the Mo_2C carbide C - and Mo - terminated, comparing with (111) Cu surface which is an active catalyst for the reaction. Here again the interaction of the catalyst with atomic oxygen is extremely important. In fact the activity for the clean surfaces decreases in the order Cu > Mo_2C (C terminated) > Mo_2C (Mo terminated), but this order is changed by adsorption of a rather small amount of oxygen (0.25 ML) produced by H_2O dissociation. In this case the C terminated, oxidized (001)

surface of Mo_2C become the most active one, where the same oxygen covered Mo terminated surface is by far inert.

The same reaction has been later studied by Viñes et al.[21] on the (001) surface of titanium carbide. In this theoretical study several models have been used including extended periodic systems as well as cluster models of various sizes. The catalytic activity on the perfect (001) surface of TiC was found to be the highest, and reaction was predicted through the carboxyl formation route, where (although with a smaller extent) on TiC nanoparticles the reaction is expected to occur through the redox mechanism. Reaction rates estimated for the reaction on TiC (001) infer that this can be a potential substitute for catalysts commonly used at low-temperatures.

The interesting results obtained motivated another work exploring the dissociation of H_2 on carbides of Ti, Zr, V, Mo with 1:1 stoichiometry and FCC structure. [22] In the same work was also compared the effect of the various TMC on a supported small Au_4 cluster looking for the best catalyst for H_2 dissociation.(see below) Molecular hydrogen interacts rather strongly with the clean TiC(001) and ZrC(001) substrate, but quite weakly with VC(001) and δ-MoC(001). The first two carbides are the only ones supposed to be active catalysts for hydrogenation. In fact atomic hydrogen adsorption on surface carbon atoms of both VC and δ-MoC(001) causes an important distortion of the surface with a subsequent protrusion of the surface carbon out of the plane of the uppermost layer, and it is predicted to destabilize the carbide. However on TiC, ZrC and δ-MoC(001) substrates molecular hydrogen dissociation seems to be possible because of its exothermicity (about -0.4 eV). The authors calculated a barrier of 0.80 eV for dissociation on ZrC (001) and of 0.52 eV on TiC.

1.5 Reactivity of TMC supported noble metal nanoparticles

A new important field of research is the application of TMC as active supports for noble metal nanoparticles (NMNPs).[23,24]

This important effect derives from the perturbation of the electronic density of the NMNPs interacting with the carbide support. In some cases the electron density is redistributed around the adsorbed metal atoms obtaining a formal net charge transfer from the substrate to the nanoparticle with subsequent polarization above the noble metal atoms, crucial for the activation of organic and inorganic molecules in contact with the metallic centers of the catalyst.[25] In some case it is observed the

opposite, and adsorbed metal atoms get positively charged transferring electronic density to the substrate.

Scanning tunneling microscopy (STM) images of Au, Cu, Ni and Pt adsorbed on carbides of group IV and V showed that these noble metals form flat islands at very low coverage and 3D shaped nanoparticles at medium and large coverage. DFT calculations predicted the preferential formation of bonds between the noble metal atoms and the surface carbon atoms. The significant electronic perturbation together with the net charge transfer facilitates bonding of the NMNP with electron-acceptor molecules allowing their activation.[26] For example, Au/TiC(001) and Cu/TiC(001)systems are able to cleave both S–O bonds of SO_2 at a temperature as low as 150 K, displaying a reactivity much larger than that of TiC(001) or extended surfaces of bulk copper and gold. Due to their higher activity in the first or second S-O bond cleavage, a mixed Au-Cu catalyst supported on TiC (001) is predicted to be an efficient $DeSo_x$ catalyst. The high activity depends by the Au-TiC interaction showing high activity for hydrodesulfurization of thiophene in spite of the very poor activity showed by either TiC (001) or Au (111), but also higher than conventional Ni/MoS_x catalysts. For this reason the extent of the electron density polarization from the substrate to the NMNP can be used as a descriptor helping estimating the catalytic activity of a generic NMNP/TMC system.[27]

Molecular hydrogen dissociation is another important process that has numerous applications in the chemical and petrochemical industry concerning both the hydrogenation reactions and hydrogen carrying and storage.[28] Recent studies showed the interesting catalytic activity of several NMNP/TMC systems. Florez et al.[29] studied molecular hydrogen dissociation by mean of periodic DFT calculations firstly on the clean TiC (001) surface and then on gold clusters of 4, 9 and 13 atoms supported by TiC(001). In fact in spite of the moderate activation barrier of 0.52 eV calculated for the dissociation on the clean TiC (001), small gold cluster in contact with the surface shows high catalytic activity, decreasing the activation barrier to 0.20 eV on the Au_9/TiC system and leading to the final value of 0.08 eV for the smallest Au_4 cluster. The same reaction is found to be highly impeded on bigger supported clusters like the Au_{13}, where the calculated energy barrier increases to nearly 1 eV. On the clean substrate H_2 adsorbs molecularly with the molecule center on top of a C atom and the H-H axis along the diagonal connecting C atoms. Calculated adsorption energy is of -0.48 eV placing the system 0.42 eV above the fully dissociated molecule. In the transition state one H atom continues interacting with the surface carbon where the other diffuses to the nearest neighbor surface

carbon leading to the product where both H are adsorbed on top. The energy barrier of only 0.52 eV is consistent with experimental measurements that found cleavage of the molecule upon adsorption on TiC(001) at room temperature. [30,31] On the most active Au_4/TiC supported on TiC(001) reaction starts from the edge of the cluster ending with one H atom on top of the same gold and another transferred to a surface carbon atom. Although adsorption on gold atoms is slightly endothermic, moderate H_2 pressure allows achieve the complete dissociation of the molecule. The H atoms spill to the substrate creating a reservoir of atomic hydrogen.

This work clearly confirmed Au/TiC system to be an excellent catalyst for several reactions and highlights the effect of the substrates on gold nanoclusters. Gold atoms not in direct contacts with the substrate show a much lower catalytic activity that extremely increases when the support directly interacts with all the atoms of the cluster as in the Au_4/TiC(001) system. The extent of the polarization due to the adsorption of the carbide rapidly drops down increasing the number of gold layers in the cluster, fact that motivates deactivation.

The interesting results motivated another work exploring the effect of others TMC (TM = Ti, Zr, V, Mo) substrates on the smallest Au_4 cluster looking for the best catalyst for H_2 dissociation.[32] The activation barrier calculated largely decreases compared to the reaction studied on the bare support, confirming Au_4/TiC (001) as the most active one (E_{act} = 0.08 eV), and VC as the less active (E_{act} = 0.36 eV) and the reaction is predicted to be exothermic for all Au_4/TMC systems. However only for Au_4/TiC and Au_4/ZrC the atomic hydrogen produced is expected to diffuse to the support.

In general, gold nanoparticles supported by TiC are more active if compared with systems where Au nanoparticles are supported by metal oxides. An important example is the low temperature oxidation of CO.

On metal-oxide supported gold nanoparticles, temperature around 300 K is needed to break up the double bond of the oxygen molecule obtaining the atomic oxygen that finally performs the oxidation. The Au/TiC system is able to dissociate O_2 and oxidize CO to CO_2. at temperatures below 200 K, and it has been shown that this activity derive from the Au-TiC interaction, as the cleavage of the O-O bond on unsupported nanoparticles as well as on gold adsorbed on MgO(100) or TiO_2(110) is quite difficult.[33,34] Experiments supported by periodic DFT calculations showed that the O_2 molecule breaks up easily when in contact with the supported small Au

nanoparticle, and atomic oxygen diffuses on the support interacting strongly with surface carbon atoms. Experiments also confirm again that highest activity is reached for smaller flat nanoparticles adsorbed.[35,36]

All these results compose a picture that substantiates the metal-support interaction as the key point of the incredible activity showed by the Au/TiC system. However newer experiments have demonstrated that the interaction with other noble metals is even stronger, with a resulting higher catalytic activity.

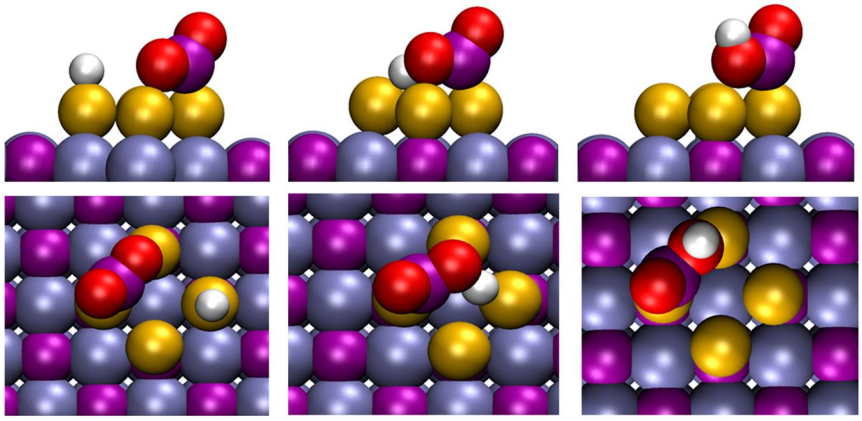

Figure 4: Minimum energy path for the hydrogenation of CO_2 on Au_4/TiC(001) catalyst. From left to right: reactants, transition state and product. Color key: purple (C), iceblue (Ti), red (O), white (H), yellow (Au). Adapted from ref (37).

The CO_2 activation and hydrogenation is an important example. In fact it allows reduce the amount of this green-house gas obtaining valuable chemicals like methanol or higher alcohols. Experiments and theoretical calculations performed by Vidal et al.[38,39] showed that methanol production is higher on Au/TiC system than on Cu (111), an active catalyst commonly used as a benchmark, or on TiC(001). The most surprising results concern methanol production on Cu/TiC catalysts that is constantly about two orders of magnitude faster than on Au/TiC. For all metal (Au, Cu and Ni) nanoparticle studied the production of CO by reverse water gas shift was always higher than methanol. For Au and Cu no methane was detected, as happened for Ni/TiC(001) system. For all three metals the catalytic activity largely depends by the relative height of the nanoparticles, confirming higher activity for the most dispersed two dimensional systems. The DFT calculation performed

identified surface carboxyl as a key intermediate for CO formation, pointing to the hydrogenation of CO or COOH as possible pathways for methanol synthesis.

1.6 Objectives and contents of this thesis

After the important discoveries about TMC reactivity and activation of noble metal clusters delineated in the introduction the initial perspective of this thesis was to perform a systematic study of the catalytic properties of small noble metal nanoparticles supported by early transition metal carbides. The main idea was to use such model systems for the hydrogenation of small inorganic molecules. This has been done indeed when studying the adsorption of small molecules (CO, CO_2, H_2) considering extended models for perfect surfaces but also finite models to reproduce defective adsorption sites and their extended possible reaction network on TiC and on several small supported clusters (Au_4, Au_6).

The results in agreement with the available experiments performed made us confident about the theoretical methods employed extending our research also to others materials like the less-investigated molybdenum carbides. In prospect of study CO hydrogenation on supported noble metal nanoparticles a previous necessary step was proposed and completed: gain detailed knowledge of the interaction of single noble metal atoms with the perfect non polar (001) surface of δ-MoC. However there are other more stable molybdenum carbide phases whose detailed surface structure is still controversial. For this reason we considered interesting to predict possible morphologies for the C-terminated (001) surface of the novel Mo_2C catalyst. All original results produced in this thesis are reported in chapters 3-7.

Chapter 1 reports this introduction: the generic sense of catalysis and heterogeneous catalyzed processes, interesting examples of processes catalyzed by TMC and NMNPs adsorbed on TMC and the objectives of this thesis.

Chapter 2 presents the computational methods used in the work reported in this thesis. The main basis of Density Functional Theory is outlined together with its application in condensed matter physics. Some central quantities concerning ab initio modelling of extended system are used as examples to explain physical concepts or their importance is highlighted when practically setting up the calculations.

Chapter 3 introduces the first results obtained studying the interaction of CO with TiC(001), several small Au cluster models and few defects commonly found on the clean carbide support. Defects were modelled using finite and extended models. Results obtained for adsorption on the clean support for various coverage have been used later to simulate CO thermal desorption profiles.

Chapter 4 and **chapter 5** relay on the results obtained studying hydrogenation reactions on the Au_4/TIC (001) catalyst model. **Chapter 4** focuses on the investigation about the water gas shift reaction (WGSR) on the Au/TiC model catalyst. In this case the minimum energy path for the reaction on the small Au_4 model cluster supported on TiC(001) has been identified estimating the reaction rates at industrial conditions. **Chapter 5** concerns about the hydrogenation of CO on the clean TiC(001) surface and on the small Au_4 cluster supported as well as on small Au clusters supported on the bulk TiC(001) surface.

Chapter 6 describes a study of a new system, the δ-MoC. Here we focused on the adsorption of several noble metal atoms on the non-polar (001) surface of the material. The important distortion of the surface caused by the adsorption was studied analyzing the effect on both electronic and geometrical structure.

Chapter 7 puts the basis for the study of the reactivity of another important TMC: Mo_2C. In this chapter the morphology of the C- terminated (001) surface has been guessed. Thermodynamic, electronic and structural properties of several possible terminations have been compared estimating the extent of each one for several temperatures. Such study is a first necessary step for studying adsorption of metallic clusters or reactivity on clean Mo_2C (001). This work also extends the concepts developed to estimate the stability of polar surfaces of semiconductors to systems with an intermediate character like TMC.

The conclusions of this thesis are given in **chapter 8**.

References

1 C. E. Tucker, J. G. de Vries, Topics in Catalysis, 2002, 19, 111.

2 Adapted from http://en.wikipedia.org/wiki/Catalysis

3 Resurces.school.co.uk/johnsonmatthey/

4 Lawrie Lloyd, Handbook of Industrial Catalysts, Springer Science+Businnes Media, LLC, 2011.

5 Photograph: Bettmann/Corbis.www.theguardian.com/lifeandstyle/wordofmouth/2010/oct/27/old-ale-beer-history

6 Clement and D'esormes, Ann. Chim., 1806, 59, 329.

7 http://www.essentialchemicalindustry.org/

8 F. Sherwood Taylor, A History of Industrial Chemistry, Heinemann, London, 1957, 429.

9 J. J. Berzelius, Ann. Chim. Phys., 1936, 61, 146.

10 H. Knözinger, K. Kochloefl, Heterogeneous Catalysis and Solid Catalysts, in Ullmann's Encyclopedia of Industrial Chemistry, Wiley, 2003.

11 D. N. Belton, Y. M. Sun, J. M. White, J. Phys. Chem., 1984, 88, 5172.

12 S. J. Tauster, Acc. Chem. Res., 1987, 20, 389.

13 H. H. Hwu, J. G. Chen, Chem. Rev, 2005, 105, 185.

14 R. B. Levy, M. Boudart, Science, 1973, 181, 547.

15 N. Ji, T. Zhang, M. Zheng, A. Wang, H. Wang, X. Wang, J. G. Chen, Angew. Chem. Int. Ed., 2008, 47, 8510.

16 S. T. Oyama, The Chemistry of Transition Metal Carbides and Nitride, Springer, 1996.

17 S. V. Didziulis, K. D. Butcher, Coord. Chem. Rev., 2013, 257, 93.

18 F. Viñes, C. Sousa, F. Illas, P. Liu, J. A. Rodriguez, J. Phys. Chem. C, 2007 , 111, 16982.

19 Y. F. Zhang, F. Viñes, Y. J. Xu, Y. Li, J. Q. Li, F. Illas, J. Phys. Chem. B, 2006, 110, 15454.

20 P. Liu, J. A. Rodriguez, J. Phys. Chem. B, 2006, 110, 19418.

21 F. Viñes, J. A. Rodriguez, P. Liu, F. Illas, J. Catal., 2008, 260, 103.

22 E. Florez, T. Gomez, J. A. Rodriguez, F. Illas, Phys. Chem. Chem. Phys, 2011, 13, 6865.

23 J. A. Rodriguez, F. Illas, Phys. Chem. Chem. Phys., 2012, 14, 427.

24 F. Viñes, A. Vojvodic, F. Abild-Pedersen, F. Illas, J.Phys Chem. C, 2013, 117, 4168.

25 J. A. Rodriguez, F. Viñes, F. Illas, P. Liu, Y. Takahashi, K. Nakamura, J. Chem. Phys., 2007, 127, 211102.

26 E. Florez, L. Feria, F. Viñes, J. A. Rodriguez, F. Illas, J. Phys. Chem. C, 2009, 113, 19994.

27 L. Feria, J. A. Rodriguez, T. Jirsak, F. Illas, J. Catal., 2011, 279, 352.

28 J. M. Thomas, W. J. Thomas, Principles and Practice of Heterogeneous Catalysis, Wiley-VCH, Weinheim, 1996.

29 E. Florez, T. Gomez, P. Liu, J. A. Rodriguez, F. Illas, ChemCatChem, 2010, 2, 1219.

30 J. A. Rodriguez, P. Liu, Y. Takahashi, K. Nakamura, F. Viñes, F. Illas, J. Am. Chem. Soc., 2009, 131, 8595.

31 K. Edamoto, E. Miyazaki, T. Anazawa, A. Mochida, H. Kato, Surf. Sci.,1992, 169/270, 389.

32 E. Florez, T. Gomez, J. A. Rodriguez, F. Illas, Phys. Chem. Chem. Phys, 2011, 13, 6865.

33 C. T. Campbell, S. C. Parker, D. E. Starr, Science, 2002, 298, 811.

34 M. Haruta, Catal. Today, 1997, 36, 153.

35 L. K. Ono, D. Sudfeld, B. Roldan Cuenya, Surf. Sci., 2006, 600, 5041.

36 J. A. Rodrıguez, L. Feria, T. Jirsak, Y. Takahashi, K. Nakamura, F. Illas, J. Am. Chem. Soc., 2010, 132, 3177.

37 J. A. Rodriguez, P. J. Ramirez, G. G. Asara, F. Viñes, J. Evans, P. Liu, J. M. Ricart, F. Illas, submitted.

38 A. B. Vidal, L. Feria, J. Evans, Y. Takahashi, P. Liu, K. Nakamura, F. Illas, J. A. Rodriguez, J. Phys. Chem. Lett., 2012, 3, 2275.

39 J. A. Rodriguez, J. Evans, L. Feria, A. B. Vidal, P. Liu, K. Nakamura, F. Illas, J. Catal., 2013, 307, 162.

Chapter 2

Methodology

This chapter is intended to a reader that is already aware about standard computational techniques used in quantum chemistry, material modeling and computational heterogeneous catalysis as well as the basis of solid state physics. The theoretical basis of Density Functional Theory (DFT) will be sketched as normally it is implemented when studying the electronic structure of solid state systems. Some characteristic quantities always present in periodic calculations will be presented highlighting why they are important and needed to justify the computational set up chosen. The methodology here presented has been used throughout the thesis. Complete and detailed expositions about the methods commonly used in quantum chemistry can be found in ref (1) and ref (2). A deep explanation of the theoretical foundation of Density Functional Theory as well as its most common application and implementation can be found in ref (3) and in ref (4). An introduction about the solid state can be found in ref (5) and ref (6), whereas for a general discussion about electronic structure calculation in solid state the reader can refer to ref (7).

2.1 Density functional calculations on extended systems: Bulk material and surfaces.

Density functional theory (DFT) has been developed in the sixties as a viable alternative to calculate the ground state properties of a multi-electronic system without dealing explicitly with the multi-electronic wave function but just with a quantity strictly related to it: the electronic density $\rho(\mathbf{r})$. It has been shown by Hohenberg and Kohn in their first theorem that the ground state electron density of a system cannot be derived by two different nuclear (external) potentials.[8] This means that there is one and only one non-degenerated ground state electron density associated to a certain nuclear potential. The electron density determines the external potential that affects the Hamiltonian, and

consequently it determines also the wave function. In this way the total energy of the system E_0 turns to be a functional of the electron density $\rho(\mathbf{r})$.

$$E_0 = E[\rho(\mathbf{r})] \quad (1)$$

This theorem bases the application of DFT for the study of the electronic structure of molecules and solids. However is with Hohenberg and Kohn's second theorem that DFT gains practical applicability for the study of chemical systems.[8] It is an application of the variational principle for the electronic density. The theorem states that the total energy E calculated using a trial density $\rho^T(\mathbf{r})$ will be always higher than the total energy of the system with real density $\rho(\mathbf{r})$, E_0.

$$E[\rho^T(\mathbf{r})] > E_0[\rho(\mathbf{r})] \quad (2)$$

In principle any improved trial density more similar to the real electron density $\rho(\mathbf{r})$ lowers the total energy calculated. Up to this point DFT seems to be extraordinary promising when treating systems with a huge number of electrons like a molecule or the unitary cell of a solid.

Traditionally in the DFT framework the total energy is decomposed in several contributions, each one functional of the electronic density $\rho(\mathbf{r})$.
Such decomposition[4] is presented in eq. (3):

$$E_0[\rho(\mathbf{r})] = T_{ni}[\rho(\mathbf{r})] + \{V_{ne}[\rho(\mathbf{r})] + \\ + V_{ee}[\rho(\mathbf{r})] + \Delta V_{ee}[\rho(\mathbf{r})] + \Delta T[\rho(\mathbf{r})]\} \quad (3)$$

The first term in eq. (3), $T_{ni}[\rho(\mathbf{r})]$, refers to the kinetic energy of non-interacting electrons whose density is equal to the real density of the system. The other terms in curly brackets include all classical and non-classical electron - electron and electron - nuclei interactions. The second and the third term, $V_{ne}[\rho(\mathbf{r})]$ and $V_{ee}[\rho(\mathbf{r})]$, are the attractive potential between electrons and nuclei, often referred as "external potential", and the classical electron-electron repulsion. The physical nature of the electrons produces all differences between a fictitious system of particles that interact classically and the real system. All those differences are included in the last two terms of Eq (3). The first contribution, ΔV_{ee} $[\rho(\mathbf{r})]$, refers to all non-classical correction to the electron-electron repulsion energy. The last term in Eq (3), $\Delta T[\rho(\mathbf{r})]$, corrects the kinetic energy including the effect of the correlation of the electrons motion.[4]

However problems arise when considering electrons mutual interactions and all those effects that do not exist in the "classic" world well described by the first three terms of eq. (3).[4]
The (older) Hartree – Fock (HF) mean field approximation[1] considers the physical nature of electrons fulfilling anti-symmetry principle when constructing the wave functions through Slater determinants. In this way the exchange contribution to the total energy is naturally taken into account avoiding that electrons with same spin get too close. However the monodeterminantal HF picture completely neglects motion correlation treating each time all electrons but one as a homogeneous diffuse charge density where the remaining electron moves as a particle. For this reason post HF methods are needed for a good description of the physics of the system. DFT includes all this non classical quantities, ΔV_{ee} and ΔT in eq. (3), in some empirical functional of the density, since the exact analytical form is unknown.
In the DFT approach the electronic density is expressed in term of occupied orbitals ψ_i as

$$\rho(\mathbf{r}) = \sum_i |\psi_i| \tag{4}$$

one can then define a set of monoelectronic equations that can be solved in a self-consistent way, determining ψ_i.[9]

$$h_i^{KS}\psi_i = \varepsilon_i \psi_i \tag{5}$$

The term h^{KS} in eq. (5) represents an effective monoelectronic Hamiltonian, defined as

$$h_i^{KS} = -\frac{1}{2}\nabla^2 - \sum_k^{nuclei} \frac{Z_k}{|r_i - r_k|} + \int \frac{\rho(r')}{|r_i - r'|} dr' + V_{eff} \tag{6}$$

and finally

$$V_{eff}(\mathbf{r}) = \frac{\delta E_{XC}[\rho(\mathbf{r})]}{\delta \rho(\mathbf{r})} \tag{7}$$

The term E_{XC} in eq. (7) includes the last two terms in curly brackets in eq. (3).

2.2 Common DFT functionals

A careful chose of the type of exchange-correlation (XC) functional as well as its flavor within each approximation has to be done when setting up some electronic structure calculations. It was commented in the previous section that

the exact analytical form to calculate the exchange and correlation contribution to the total energy is unknown. For this reason nowadays the numerous approximations available in commercial codes are commonly classified according with the functional form used to extract information from the density function.

The XC functional can depend on the value of the electron density in each point of the space, or on the value of the density together with its first or second derivatives. The first XC approximation is called Local Density Approximation, (*LDA*), and explicitly supposes that the density changes slowly with the position as it happens in a metallic system.[10,11]

The second approximation, known as Gradient Generalized Approximation (*GGA*), can better describe more complex systems like metal oxides or carbides.[12] Two of the most widely used implementation of this last approximation, PW91 and PBE, are both available in VASP.[13,14] It is worth to cite the B3LYP as the most used hybrid functional which includes 20% of exact HF exchange when calculating XC energy.[15] Another important approximation known as DFT-D*X* was developed by S. Grimme.[16] This approximation allows to take into account for the dispersion forces adding an energetic term to the standard DFT Hamiltonian. It uses a parameterized Lennard-Jones potential and depends from just pairwise (X = 2), or also three-body (X = 3) interactions, essential to describe non-covalent bond.[17]

2.3 Important parameters and characteristic quantities

2.3.1 K points grid and basis set

Some other important parameters have to be converged when setting up periodic electronic structure calculations of solids. These are the number of **k** points used to evaluate the energy of the system and the size of the basis set used to approximate the electronic states. Whenever these two important parameters have been converged, then the XC functional can be varied looking for the one that give the best value for some important bulk property, or some other property of interest. Commonly the optimization of the cell parameter is followed by the calculation of the bulk modulus (a quantity related to the compressibility of the material) and used to determine which XC functional best describe the system. Concepts like **k** point, direct and reciprocal lattices derive from the treatment of solids as infinite perfect systems. Obviously this is a big approximation of the physical reality of condensed matter but it gives the possibility to study plenty of extended systems.

Periodic solid is composed by a repetition unit, the conventional cell, replicated all over the (direct) space along some primitive vectors $\{\mathbf{a}_i\}$ which respect the translational symmetry. The translation operator commutes with the

Hamiltonian of the system and for this reason it can be chosen a common set of eigenvectors for the two operators. Such eigenstates refer to monoelectronic states describing particles subjected to the attractive potential of the nuclei V(**r**) that has the same periodicity of the unit cell. The periodic potential is defined as:

$$V(\mathbf{r}) = V(\mathbf{r} + \boldsymbol{\tau}). \quad (8)$$

Here τ is a generic vector multiple of the translational primitive vectors {$\mathbf{a}_i$} defining the unitary cell in the direct space. Bloch theorem[18] (eq. (9)) defines a general form for the wave function describing a system where electrons are subjected to a periodic potential.

$$\Psi(\mathbf{r}) = e^{ik\mathbf{r}} u(\mathbf{r}) \quad (9)$$

Where $e^{ik\mathbf{r}}$ is a plane wave and *u(**r**)* is a local function with the same periodicity of the direct lattice. The wave function respects the periodicity fulfilling eq. (10):

$$\Psi_{n,\mathbf{k}}(\mathbf{r} + \boldsymbol{\tau}) = \Psi_{n,\mathbf{k}}(\mathbf{r}) e^{i\mathbf{k}\boldsymbol{\tau}} \quad (10)$$

it depends parametrically on the principal quantum number *n* but also on the value of the wave vector **k**. Such wave vectors define the set of plane waves with the same periodicity of the crystal, but **k** also represents the complete set of vectors belonging to the reciprocal lattice (or **k**-space) associated to the direct one formed by the atoms that compose the solid.
The reciprocal lattice is a mathematical tool used to simplify calculations and concepts in solid state physics, based on the creation of a fictitious lattice related to the real one. The set of primitive vectors {$\mathbf{b}_i$} defining the new lattice are constructed from those of the direct one using eq. (11):

$$[\mathbf{b}_1\mathbf{b}_2\mathbf{b}_3]^T = 2\pi[\mathbf{a}_1\mathbf{a}_2\mathbf{a}_3]^{-1} \quad (11)$$

Translational symmetry in the direct lattice reduces any point of the crystal to a point in the primitive direct cell, enclosed by the set of vectors {$\mathbf{a}_i$}. In the same way any point in the reciprocal space is recovered in its primitive cell, the first Brillouin zone defined by vectors {$\mathbf{b}_i$}.
Up to this point the number of possible **k** values within the first Brillouin zone is infinite. Discretization occurs as a consequence of the application of the Born–von Karman periodic boundary conditions (B-VK PBC). B-VK PBC assumes that an infinite crystal is composed by a number of finite units containing a large number of cells along each direction. Repeated units are delimited in a formal way such that translation leads to the original point. In this sense the global crystal can be thought as cyclic. Now the problem of an infinite perfect crystal is

reduced to a finite crystal composed by a big number of conventional unit cell. Applying boundary conditions the **k** points values allowed and so the number of **k** points considered within the first Brillouin zone becomes finite because only those that are symmetrically non-equivalent are taken into account. However this number is proportional to the number of cells explicitly included in the repeated units that have to be large.[6] A huge number of different **k** values is still allowed, but and eigenvalues of the hamiltonian varies continuously allowing a discrete sampling. Calculate the total energy of the system means averaging the eigenvalues on all **k** and then summing on all *n* occupied states. Luckily the eigenvalue associated to each Bloch wave function change slowly with the value of **k**. This allows generate a thick enough **k** point grid and perform a discrete sampling of the first Brillouin zone. Sufficient accurate sampling converge the final energy value calculated respect to the number of **k** points (see Fig. 1).
Big unitary cell are associated to small Brillouin zone and just one central **k**-point is normally enough. However the reader must be aware that it can be very dangerous do not perform any test to check if the number of **k** points considered is large enough.

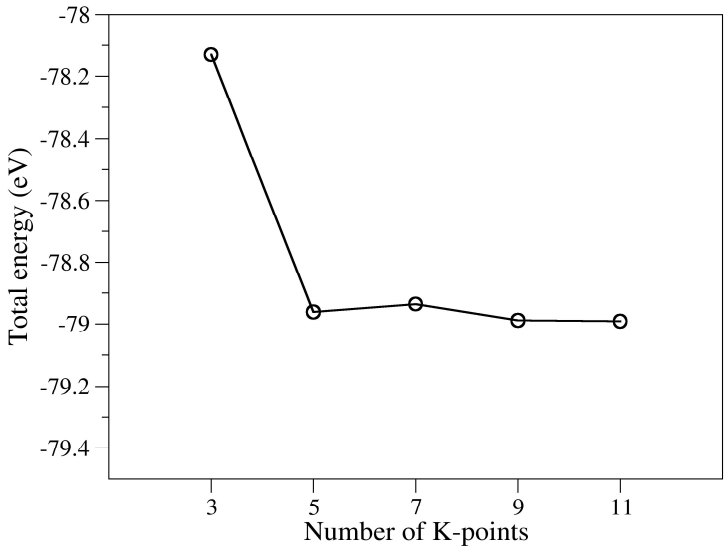

Figure 1: Total energy of the bulk unit cell of δ-MoC calculated using different **k** point meshes. The profile reports the total energy (eV) versus the number of **k** points used (along each direction) when generating the 3 dimensional grid used to sample the first Brillouin zone.

Another important parameter to be converged carefully is the basis set of the calculation.

The Bloch wave function (or crystal orbital) can be expanded as a linear combination of functions. All the results presented in this thesis have been obtained using the code VASP[19,20,21] that uses a plane wave basis set. Localized atom centered basis set are normally of Gaussian type like those implemented in the code CRYSTAL[7] or numerical as used in the DMol3 code.[22]

Using plane wave basis set the local function in eq. (9) ***u(r)*** equals the unity and the Bloch function can be expressed as:

$$\Psi_{n,\mathbf{k}}(\mathbf{r})e^{i\,\mathbf{k}\tau} = \sum_{\mathbf{g}} a_{\mathbf{n},\mathbf{g},\mathbf{k}} e^{i(\mathbf{g}+\mathbf{k})\mathbf{r}} \qquad (11)$$

where {**g**} is the complete set of wave vectors of the plane waves that respect the periodicity of the reciprocal lattice and {$a_{n,g,k}$} is the set of coefficients used in the linear expansion. However this requirement is fulfilled by infinite plane wave that would be included in the expansion. Practically it is truncated for a large value of **g** for which the contribution of those plane waves is negligible, $\mathbf{G}_{cut}$.

$$|\,\mathbf{G}_{cut}\,| \geq |\,\mathbf{g}+\mathbf{k}\,| \qquad (12)$$

2.3.2 Atomic Charges

Atomic charge is a concept normally used to support chemical intuition but despite it is part of the standard chemical knowledge its definition is not unique. In fact atomic charge is not a quantum observable because there is not a unique way to define an atom within a molecule. For this reason several non-equivalent definitions are accepted and used, and the final value of the atomic charge or the charge transfer calculated is dependent from the method used.

In this thesis atomic charges have been calculated in agreement with the theory of Atoms In Molecules (AIM) developed by Bader.[23] Within this theory the volume of space associated to each atom in a molecule is determined drawing zero - flux 2-D surfaces in correspondence to the minima of the charge density of the system around the atom considered. As normally the electron density of a molecule presents cusps corresponding with the nuclei, minima result located in the region between two atoms. Surfaces are then drowned perpendicular to the straight line connecting two maxima in correspondence of the electron density minimum. This divides the electron density shared between the two nuclei leaving each atom on one side of the zero - flux surface. In this way a definition

of the volume occupied by each atom within the molecule can be obtained using just any electron density function suitable for the system without other assumptions on the size or the shape of the atoms. The final value of the atomic charge is obtained subtracting the integrated charge density within the volume associated to each atom from the number of electrons of the neutral atom. The integration gives the number of electrons contained in the Bader volume associated with that atom. This task has been performed using a code developed by the Henkelman group, [24] freely available online.

On this topic plenty of literature is available from the personal work and webpage of Bader or Henkelman groups.[25,24] New interesting developments of the theory and investigations about the more intimate consequences of this theory can be found in the recent works of many groups around the world. Between them here it is nice to remember the work done by the Quantum Chemistry Group of the University of Oviedo.[26]

2.3.3 Density of States

Due to the periodicity of the crystal the discrete electronic structure of a molecular system turns to be a continuum of energetic regions where there is (or there is not) presence of quantum states available for occupation by electrons. Important information about the behavior of the material can be extracted from the analysis of its Density Of States (DOS). Such profile reports the number of states present for a given binding energy allowing the classification of the material as insulator or metal, depending of the presence (or the absence) of electronic bands across the Fermi level E_F. The presence of a band-gap between unoccupied conducting states and occupied valence states defines a material as insulator.

The transition metal carbides of the groups IV-VI, investigated in this thesis, are metallic systems. This means that the last occupied state, the highest in energy corresponding to the HOMO of a molecular system, belong to a band that is just half-filled and that there are empty states available in the proximity of the Fermi level. For instance Fig. 2 reports the DOS of the bulk δ-MoC system. The Fermi energy is by definition equal to zero as it is the energy of the Fermi level, the last occupied state of the system. For this reason the numerical value obtained for the binding energy associated with the Fermi level is normally subtracted from the effective binding energy calculated for every state. In this way the zero of the energy corresponds again with the Fermi level.

The presence of geometrical distortions, atom substitutions, vacancies or interstitial atoms and adsorbates changes the electronic structure of the material and its effect can be detected in the total DOS but also projecting the total DOS. The projected total DOS (PDOS) gives the contribution of the states associated to a region of the system or a certain atom to the total DOS. In this way it is possible to determine the contribution, or the changes, on a set of orbitals and also arriving to define the role of each spin orbital of the system.

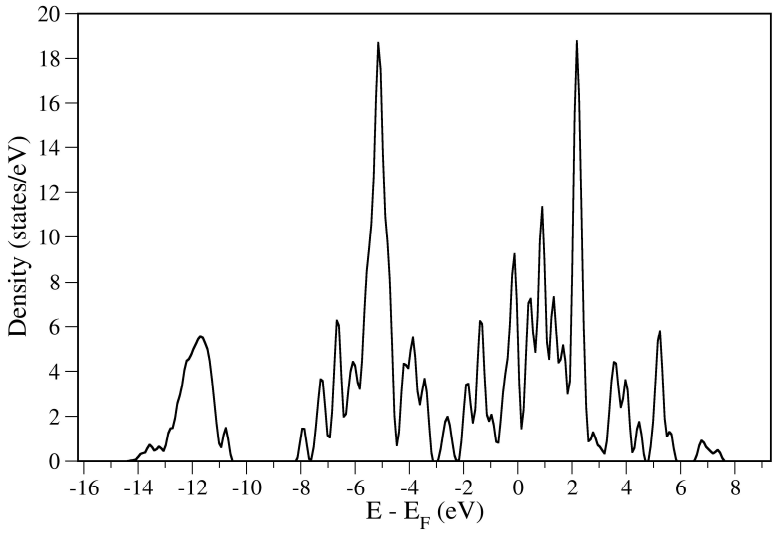

Figure 2: Total density of States (DOS) calculated for the δ-MoC bulk system. The metallic behavior of this material derives from the presence of continuum DOS across E_f.

2.4 Surface slab model

All the heterogeneous catalytic processes analyzed in this thesis were studied using periodic surface models that allow a realistic description of the physical nature of the surface considering the relaxation caused by the vacuum felt by the outermost atomic layers of the material. Unfortunately the high level quantum chemistry methods accessible on “molecular” scale cannot be used, so DFT is the most common approximation adopted in this as well as many fields of material science. The periodic surface model is created from the bulk material adding some vacuum along the direction perpendicular to surface of interest. This disrupts the translational symmetry within the crystal along that direction and the system created is now infinite in 2 direction and finite along the third one. The vacuum (commonly 10-12 Å) has to be enough to avoid interaction between replicas of the unit cell.

The atomic layers included in the slab are not all physically identical because those more external feel a different environment depending on the proximity of the vacuum where those more internal should behave as bulk material. For this reason the bottom layers of the slab are frozen in their optimized bulk positions where the uppermost layers are relaxed together with the adsorbates (if present). However the slab needs to be thick enough so the relaxed layers feel the *bulk-like* effect of the internal atoms despite of the replicated vacuum under the bottom of the slab. This should be checked considering a thick enough slab and always increasing the number of relaxed layers checking the convergence with the total energy. The profile of the total energy, function of the number of relaxed layers, presents a plateau (see Fig. 3) when relaxing the most internal layers. It ensures that those atoms do not feel the vacuum and are therefore behaving like bulk material.

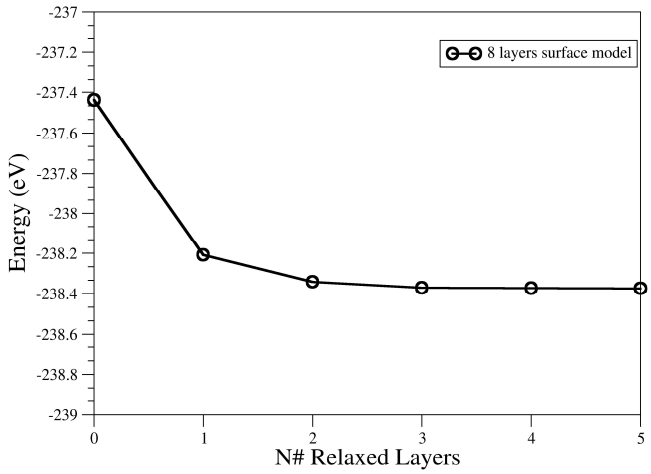

Figure 3: Total energy of the 8 layer slab model of the C-terminated (001) surface of Mo_2C *vs* number of relaxed layers. The perfect bulk-cut slab is reported as 0 relaxed layers. The lack of energy change when relaxing the internal layers of the slab ensures that the center of the slab behaves as the β-Mo_2C bulk material.

2.5 Chemical reactions on surfaces

2.5.1 Adsorption and desorption processes

Adsorption of reactants on a surface is the very initial step for every heterogeneous reaction. It is considered a non-activated process when molecules pass from the gas phase to form an adsorbed phase on the surfaces of the catalyst. Adsorption modifies both molecule and catalyst, activating some

molecular bonds and modifying the surface structure. Important quantities involved in adsorption processes are the adsorption energy E_{ads}, the distortion energy E_{dist} and the extent of the lateral interaction between adsorbates E^{LI}.

The adsorption energies reported in this manuscript has been always calculated as:

$$E_{ads} = E_{surf+mol} - E_{mol} - E_{surf} \quad (13)$$

Where $E_{surf+mol}$ stays for the total energy of the adsorbed system, E_{mol} is the energy of the relaxed gas phase molecule and E_{surf} is the energy of the relaxed slab. This means that a stronger bond between molecule and surface will produce a more negative value of the E_{ads} calculated. The adsorption energy is a quantity that depends of the slab model used. Slab models that reproduce different coverage can lead to a change in the calculated adsorption energy. The adsorption process in fact is a balance between the attraction of the molecule for the surface and the distortion of both molecule and surface from their equilibrium geometry to the adsorbed geometry. The distortion of the surface can be estimated calculating the distortion energy E^{s}_{dist}:

$$E^{s}{}_{dist} = E_{surf-mol} - E_{surf} \quad (14)$$

E^{s}_{dist} is the difference between the energy of the slab frozen in the adsorbed geometry but without the molecule $E_{surf\text{-}mol}$, and the energy of the relaxed naked slab E_{surf}. The distortion energy of the molecule, E^{m}_{dist}, can be considered comparing the energy of the relaxed molecule in the gas phase, E_{mol}, and that of the molecule frozen in the adsorbed geometry but without the surface, $E_{mol\text{-}surf}$.

$$E^{m}{}_{dist} = E_{mol-surf} - E_{mol} \quad (15)$$

However other effects can influence the calculated adsorption energy. The strength of the lateral interactions E^{LI} can be estimated calculating the difference between the energy of one isolated gas phase molecule distorted as in the adsorbed geometry respect to that of a lattice of *n* molecule frozen in the adsorbed geometry at certain coverage θ but without the underlying surface $E^{\theta}_{mol\text{-}surf}$.

$$E^{LI} = n(E_{mol}) - E^{\theta}_{mol-surf} \quad (16)$$

E^{LI} in eq. (16) can be positive or negative depending if the interaction between adsorbates is repulsive or attractive, contributing to decrease or increase the average E_{ads}. However for sufficient low coverage lateral interactions between adsorbates can be normally neglected.

2.5.2 Identification of reactants, transition states and products.

The first step to study a reaction on a surface is to determine the adsorption and the co- adsorption geometry of reactants. It should be done considering the final equilibrium geometry of the products and guessing what seems to be the most probable pathway connecting the two minima on the potential energy surface (PES).

The minimum structures need to be characterized by vibrational analysis calculating the harmonic frequencies associated to the normal modes of the minimum geometry structures. In VASP it is done by explicit calculation of the Hessian matrix of the portion of the system of interest, normally just the adsorbates. Every atom considered in the vibrational analysis is moved along each direction and then the forces generated are calculated. Once the 6 force constants are calculated for each atom, the matrix is diagonalized obtaining the harmonic force constant $\boldsymbol{k_i}$ for the collective movement of all atoms along each normal mode ***i*** of the system. Then the harmonic vibrational frequency for each normal mode ***i*** can be calculated knowing the reduced mass (μ in eq. (17)) of the system.

$$f_i(s^{-1}) = \frac{1}{2\pi}\left(\frac{\mathbf{k}_i}{\mu}\right)^{1/2} \qquad (17)$$

All frequencies calculated for a minimum structure have to be real. Once the most stable geometry for reactants and products have been determined and both have been characterized as minimum by vibrational analysis one can further identify the geometry of the transition state (TS) connecting the two minima. This is the maximum along the minimum energy path (MEP) connecting reactants and products.

Let's consider a chemical reaction of the type:

Reactants -> $[TS]^{‡}$ -> Products

Identify the TS structure along the MEP is interesting because (1) the MEP will be the mechanism of formation of the products with maximum statistical weight, and (2) if we are considering a single step process or the reaction limiting step then the reaction rate can be estimated comparing the energy of the TS structure respect to the reactants. Several algorithms are now available to determine the TS structures using VASP.[27,28] All TS structures reported in this thesis have been identified using the CI-NEB (Climbing Image Nudged Elastic Band) algorithm.[29] The CI-NEB algorithm creates and optimizes several intermediate structures between reactants and products (often called *images*) trying to minimize their energy. This will bring the images toward the minima on the PES, falling down in correspondence of reactants or products. However along the guessed MEP images are interconnected by "harmonic springs". These fictitious forces avoid images to fall down on one side or the other of the energetic barrier. The CI modification to the algorithm cancels the forces, due to the springs, on the image higher in energy and inverts the sign of the forces calculated due to the PES itself. In this way the image is pushed up, *climbing* the energy barrier and maximizing its energy along the band formed by all images. This method works fine although it is very expensive as each image is optimized separately. For this reason the number of the relaxed atoms explicitly included in the NEB has to be chosen carefully trying to minimize the degrees of freedom of the system. Once a good candidate for the TS has been identified, vibrational analysis will shed light on the real nature of structure. Just one imaginary frequency associated to the normal mode connecting reactants and products, whose wavenumber is higher than about 350 cm^{-1}, ensures that the structure found is a real transition state. Now this structure has to be relaxed using a first derivative algorithm (like the quasi – Newton algorithm implemented in VASP)[30] and then the vibrational analysis should be performed again. Although the total energy should be sensibly lower compared with that of the first TS guess, there should be no important change on the frequencies calculated. This ensures the goodness of the TS structure found.

For an extended discussion about TS search methods with VASP one can refer to the Henkelman group website.[24]

References

1 A. Szabo, N. S. Ostlund Modern Quantum Chemistry: Introduction to Advanced Electronic Structure Theory; Courier Dover Publications, 1996.

2 F. Jensen, Introduction to Computational Chemistry, Wiley, 2006.

3 W. Koch, M. C. Holthausen, A chemist's guide to Density Functional Theory, 2nd Edition, Wiley, 2001.

4 C. J. Cramer, Essentials of Computational Chemistry. Theories and Models, 2nd Edition, Wiley, 2004.

5 C. Kittel, Introduction to Solid State Physics, 8th Edition, Wiley, 2004.

6 N. W. Ashcroft, D. N. Mermin, Solid State Physics, Cengage Learning Emea, 1976.

7 R. Dovesi, V. R. Saunders, C. Roetti, R. Orlando, C. M. Zicovich-Wilson, F. Pascale, B. Civalleri, K. Doll, N. M. Harrison, I. J. Bush, P. D'Arco and M. Llunell, CRYSTAL06, CRYSTAL06 User's Manual, University of Torino, Torino, 2006.

8 P. C. Hohenberg, W. Kohn, Phys. Rev., 1964, 136, 864.

9 W. Kohn, L. J. Sham, Phys. Rev., 1965, 140, A1133.

10 A. Zunger, J. P. Perdew, Phys. Rev. B, 1981, 23, 5048.

11 S. H. Vosko, L. Wilk, M. Nusair, Can. J. Phys., 1980, 58, 1200.

12 J. P. Perdew, J. A. Chevary, S. H. Vosko, K. A. Jackson, M. R. Pederson, D. J. Singh,

C. Fiolhais, Phys. Rev. B: Cond. Matter, 1992, 46, 6671.

13 Y. Wang, J. P. Perdew, Phys. Rev. B, 1991, 43, 8911.

14 J. Perdew, K. Burke, M. Ernzerhof, Phys. Rev. Lett., 1996, 77, 3865.

15 P. J. Stephens, F. J. Devlin, M. J. Frisch, J. Phys. Chem., 1994, 98, 11623.

16 S. Grimme, J. Comp. Chem., 2006, 27, 1787.

17 S. Grimme, J. Antony, S. Ehrlich, H. Krieg, J. Chem. Phys., 2010, 132, 154104.

18 Bloch, F. Z. Phys., 1929, 57, 545.

19 G. Kresse, J. Furthmüller, Comput. Mater. Sci., 1996, 6, 15.

20 G. Kresse, J. Phys. Rev. B, 1996, 54, 11169.

21 G. Kresse, J Hafner, J. Phys. Rev. B, 1993, 47, 558.

22 B. Delley, J. Chem. Phys., 2000, 113, 7756.

23 R. Bader, Atoms in Molecules: A Quantum Theory; Oxford University Press, 1994.

24 http://theory.cm.utexas.edu/henkelman/

25 http://www.chemistry.mcmaster.ca/aim/

26 http://azufre.quimica.uniovi.es/amp/amp.html

27 H. Jonsson, G. Mills, K. W. Jacobsen, Nudged Elastic Band Method for Finding Minimum Energy Paths of Transitions, in “Classical and Quantum Dynamics in Condensed Phase Simulations”, ed. B. J. Berne, G. Ciccotti, D. F. Coker, World Scientific, 1998.

28 G. Henkelman, H. Jónsson, J. Chem. Phys., 1999, 111, 7010.

29 G. Henkelman, B.P. Uberuaga, H. Jónsson, J. Chem. Phys.,2000, 113, 9902.

30 P. Pulay, Chem. Phys. Lett., 1980, 73, 393.

Chapter 3

CO adsorption on TiC(001) and Au/TiC(001)

The first part of this chapter reports the work done in collaboration between our laboratory, the Quantum Chemistry Group of Universitat Rovira i Virgili, the groups of the Institute of Theoretical and Computational Chemistry of the Universitat de Barcelona (IQTC-UB), and the BNL (USA).[1] The second part has been done in collaboration between our laboratory and the groups of IQTC-UB, Departament de Química Inorgànica & IN2UB (Universitat de Barcelona), Surface Chemistry and Catalysis Group, Department of Chemistry (University of Aberdeen).[2] In this case experiments were carried out at the Departament de Química Inorgànica & IN2UB of the Universitat de Barcelona.

This chapter concerns the adsorption of carbon monoxide on several models of gold nanoparticle supported on TiC, on the extended (001) surface of the support as well as on several types of defects commonly presents in rock-salt structured materials. Carbon monoxide is a component of the synthetic gas, or *syngas*, a mixture of CO and molecular hydrogen but containing also CO_2 and H_2O in various proportions, mainly produced by reaction of water with methane (steam reforming).[3]

CO is also an important “probing molecule” commonly used in experiments and a huge literature relating desorption temperature and vibrational frequency shifts with adsorption sites and energies is available. However in some cases the straightforward interpretation of such results leads to misinterpretations corrected by theoretical evidences.[4]

The interaction with gold nanoparticle has been reproduced with 2 and 3 dimensional gold nanostructures adsorbed on TiC (001). Such computational

models present low coordinated gold atoms and already demonstrated to correctly predict the reactivity of Au/TiC system.[5]

It is necessary to investigate adsorption before studying any catalytic process involving carbon monoxide because that is the very first step of every heterogeneous reaction. The interaction of the probe molecule with the naked support gains interest because of the intrinsic TMC catalytic properties already detailed in the introduction of this thesis, and because it represents the majority of the surface exposed to the gas phase reactants by any heterogeneous catalysts.

Before to study the adsorption on the various models, some bulk and surface properties including density of states, bulk modulus and other surface characteristic quantities (interlayer rumpling, surface energy) were calculated, comparing with previous theoretical calculations and experiments. This is needed to optimise the computational set up used and ensure the goodness of our models. Carbon monoxide adsorption was explored in all possible sites and geometries on naked TiC and on each gold nanoparticle observing a preferential interaction with the surface carbons of the clean substrate. The interaction of CO with supported gold nanoparticle showed that adsorption is stronger on lower coordinated gold atoms and, as expected, smaller nanoparticles bind stronger than bigger ones. Upon adsorption on naked TiC (001) a strong C-C_s double bond is formed between the molecule and the exposed carbon causing an important distortion of the surface. Such local structural features are conserved when adsorbing CO on other surface models used to reproduce different coverage. The increment of the adsorption energy (E_{ads}) calculated when lowering the coverage is strictly related with such distortion and can be rationalised calculating the normalised distortion energy ($E_{dist,norm}$) in each supercell model.

The second part of this chapter further examines the interaction of CO with TiC analysing some possible common defective adsorption sites on the surface by mean of both extended and finite models as well as experiments performed on TiC nanopowders. Adsorption on TiC (001) terraces studied with standard periodic slab models reproduces substantially the results obtained for the extended (001) surface in high coverage situation and CO experiments moderate adsorption energy. The interaction strength increases dramatically for low coordinated sites such edge or kink sites becoming irreversible. These adsorption trends have also been reproduced using a small 64 atoms TiC

nanocube and studying adsorption on facets, edge and corners. Temperature programmed desorption (TPD) experiments performed after deposition at room temperature let infer an adsorption energy in agreement with the DFT results obtained for low coverage situations.

The literature about CO adsorption on TiC (001) and on small TiC clusters is controversial and presents results that differs in both preferred adsorption site and adsorption energy depending on the computational methodology, and results obtained with extended slab models contradict previous theoretical studies.[6,7,8] The high adsorption energy calculated for low coverage situation does not agree with values inferred from older TPD experiments.[9] For this reason a simple kinetic Monte Carlo (kMC) model that explicitly consider the interaction of the molecule with the surface, the effect of the neighbouring occupied adsorption sites as well as surface diffusion was implemented adapting the algorithm proposed by Meng et el.[10] to simulate the TPD experiment, using our calculated values of the adsorption energy on TiC (001) at various coverage as starting parameters. Simulated TPD solves the apparent controversy agreeing with both previous and new experimental results presented.

References

1 G. G. Asara, L. Feria, E. Florez, J. M. Ricart, P. Liu, J. A. Rodriguez, F. Illas, J. Phys. Chem. C, 2011, 115, 22495.

2 B. P. Mant, G. G. Asara, J. A. Anderson, N. Homs, P. Ramírez de la Piscina, S. Rodríguez, J. M. Ricart, F. Illas, Surf. Sci., 2013, 613, 63.

3 D. A. Hickman, L. D. Schmidt, Science, 1993, 259, 343.

4 F. Illas, S. Zurita, A.M. Marquez, J. Rubio, Surf. Sci., 1997, 376, 279.

5 J. A. Rodriguez, P. Liu, Y. Takahashi, F. Vines, L. Feria, E. Florez, K. Nakamura, F. Illas, Catalysis Today, 2011, 166, 2.

6 F. Vines, J. A. Rodriguez, P. Liu, F. Illas, J. Cat., 2008, 260, 103.

7 P. Liu, J. A. Rodriguez, H. Hou, J. T. Muckerman, J. Chem. Phys., 2003, 118, 7737.

8 S. V. Didziulis, K. D. Butcher, Coordination Chemistry Reviews, 2013, 257, 93.

9 S. V. Didziulis, P. Frantz, L. C. Fernandez-Torres, R. L. Guenard, O. El-bjeirami, S. S. Perry, J. Phys. Chem. B, 2001, 105, 5196.

10 B. Meng, W.H. Weinberg, J. Chem. Phys., 1994, 100, 5280.

THE JOURNAL OF PHYSICAL CHEMISTRY C

ARTICLE

pubs.acs.org/JPCC

Theoretical Study of the Interaction of CO on TiC(001) and Au Nanoparticles Supported on TiC(001): Probing the Nature of the Au/TiC Interface

Gian Giacomo Asara,[†,‡] Leticia Feria,[†] Elizabeth Florez,[†,§] Josep M. Ricart,[‡] Ping Liu,[∥] José A. Rodriguez,[∥] and Francesc Illas*[,†]

[†]Departament de Química Física & IQTCUB, Universitat de Barcelona, C/Martí i Franquès 1, 08028 Barcelona, Spain
[‡]Departament de Química Física i Inorgànica, Universitat Rovira i Virgili, C/Marcel·lí Domingo s/n, 43007 Tarragona, Spain
[§]Instituto de Química, Universidad de Antioquia, A.A. 1226, Medellín, Colombia
[∥]Chemistry Department, Brookhaven National Laboratory, Upton, New York 11973, United States

Supporting Information

ABSTRACT: The interaction of CO with the bare TiC(001) surface and with Au_n (n = 4, 9, 13) nanoparticles supported on the same TiC(001) surface has been studied by means of periodic density functional theory (DFT) based calculations with large supercell slab models. CO adsorption on the bare TiC(001) surface involves the direct interaction with a C surface atom and leads to a significant deformation of the underlying substrate. Because of this feature the calculated adsorption energy significantly varies with coverage. A comparison with available experimental data shows that this system is more complex than expected. The interaction of CO with the Au nanoparticles involves preferential bonding to low coordinated Au atoms. However, although the supported Au nanoparticles bind CO well, the adsorption energy of the molecule on the admetal is somewhat smaller than the one corresponding to the naked carbide surface and decreases with increasing the particle size, which is also consistent with a rather small red shift of the vibrational frequency of the adsorbed CO molecule that also decreased with increasing particle size. Implications for the use of Au/TiC systems in catalytic reactions involving CO are also discussed.

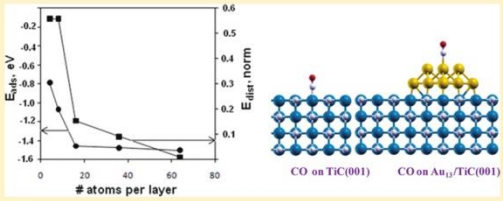

INTRODUCTION

The landmark studies of Haruta et al.[1] and of Goodman et al.[2] on the outstanding and unexpected catalytic properties of Au nanoparticles supported on TiO_2 concerning CO oxidation at low temperature have opened, no doubt, a new field[3,4] in catalysis with possible applications in chemical reactions of industrial interest.[5] Subsequent review articles have discussed different phenomena that may be responsible for the remarkable performance of Au nanocatalysts.[3,4] Although there is evidence that in some occasions the special reactivity of Au nanoparticles cannot be attributed to support effects and arises mainly from the presence of low coordinated sites[6,7] and/or from a critical nanoparticle size,[8−10] there is also overwhelming evidence that in many other cases the influence of the support is critical. In fact, experiments by Flytzani−Stephanopoulos et al.[11] have shown that Au (and also Pt) nanoparticles supported on ceria have remarkable catalytic activity for the water gas shift reaction, a very important process involved in the industrial production of molecular hydrogen to be used in petroleum hydrodesulfurization processes in the oil refineries or in the Bosch−Häber synthesis of ammonia. The important role of the underlying oxide in determining the catalytic properties of supported Au nanoparticles has been elegantly shown by Rodriguez et al.[12] in their studies using the idea of inverse catalyst which consists of ceria nanoparticles supported on Au(111). Further evidence for the importance of the support comes from the work of Serna and Corma[13] showing that Au nanoparticles supported on TiO_2 are able to chemoselectively hydrogenate the nitro group in nitrostyrene in mild conditions leaving the C=C bond intact, the reason being precisely the role between the support and the supported Au nanoparticle.[14] Corma et al. have also shown that the catalytic activity of Au nanoparticles toward CO oxidation is enhanced when supported on nanostructured ceria.[15]

From the discussion above it is clear that supports do affect the catalytic activity of Au nanoparticles but also that most of the supports used so far in these studies are mainly oxides, either reducible, such as TiO_2 and CeO_2, or nonreducible such as MgO or SiO_2. The carbides of the early transition metals exhibit chemical and catalytic properties that in many aspects are very similar to those of expensive noble metals.[16] In fact, these

Received: August 13, 2011
Revised: September 26, 2011
Published: October 10, 2011

carbides are able to catalyze the isomerization and hydrogenation of olefins,[16,17] the synthesis of large hydrocarbons through the Fischer−Tropsch process,[16] the conversion of methane to synthesis gas,[18,19] and desulfurization reactions[16,20−29] and have attracted significant attention in the past few years in rather different fields, from solid-state physics[30] to surface science[31] and catalysis.[32] Furthermore, the surfaces of transition metal carbides have been proposed as excellent supports for the dispersion of metals.[33−35] Therefore, it seems logical to attempt to simultaneously take advantage of the catalytic properties of transition metal carbides and of Au nanoparticles. This possibility was indeed explored by Ono and Roldán-Cuenya on their study of the influence of interparticle interactions on the catalytic properties of Au nanoparticles toward low temperature CO oxidation.[36] Inspired by these authors, a long-term systematic joint theoretical and experimental investigation was launched aiming at exploring the catalytic properties of metals supported on carbide substrates. Starting from a study of the electronic structure and properties of Au nanoparticles on TiC, which evidenced important Au ↔ C interactions,[37] it has been shown that Au nanoparticles supported on TiC have strong hydrodesulfurization activity being able to dissociate SO_2 and thiophene[38−41] and that they are active at dissociating H_2 and O_2.[42] That these systems dissociate H_2 could be anticipated from previous work showing that this reaction is facilitated at Au undercoordinated sites without requiring a specific particle size.[7] This is not the case for the dissociation of molecular oxygen where the Au particle size is important. Hence, it is worth pointing out that Au/TiC was the first system in which atomic oxygen was detected after dissociation of O_2 on a Au nanoparticle.[40]

In order to further investigate the nature of Au/TiC interaction, we report here a theoretical study on the adsorption of CO on TiC(001) and on Au nanoparticles supported on this single crystal surface. The focus on CO as an adsorbate is motivated by the good chemical activity of Au/TiC for the low temperature oxidation of CO.[36] Furthermore, a detailed knowledge of the interaction between CO on TiC(001) and Au nanoparticles supported on TiC(001) constitutes a necessary step before undertaking further study on the catalytic activity of Au/TiC for the synthesis of alcohols or hydrocarbons (Fischer−Tropsch) from CO hydrogenation. The choice of CO is also justified from the numerous studies on metal surfaces, and also on oxides, where the vibrational shift of the CO stretching mode is used to extract information about the extent of donation and back-donation bonding mechanism and, hence, to infer the chemical nature of the active sites.[43] Nevertheless, it is important to point out that the use of CO as a probe molecule requires caution since the conclusions arising from these studies are not as straightforward as one can learn from the classical literature. In fact, it is important to notice that bonding mode assignments based on the CO stretching frequency have led to misinterpretations as shown via photoelectron diffraction experiments[44] and theoretical calculations. For instance, a careful analysis of the interaction of CO on Pt(111) reveals that both donation and back-donation mechanisms contribute to the observed red shift.[45] Likewise, a rather recent study of the interaction of CO on Au atoms supported on MgO(001) thin films reveals that the probe molecule can induce the observed effect; the presence of CO induces significant chemical modifications (charge state) of the supported gold species indicating that the interpretation of vibrational spectra of adsorbed CO requires special care.[46]

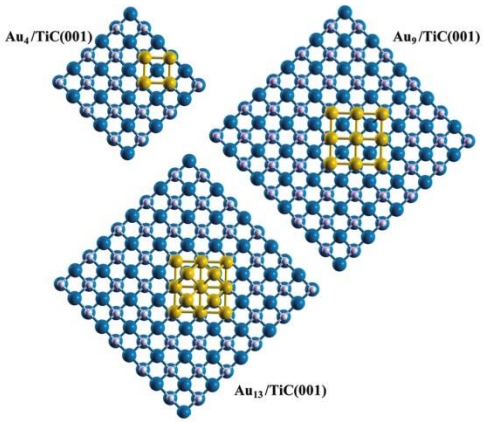

Figure 1. Top view of the full supercell models used to represent the Au_4/TiC(001) and Au_9/TiC(001) and top and side views of Au_{13}/TiC(001). The color code used in the drawing is C (white), Ti (blue), and Au (yellow).

SURFACE MODELS AND COMPUTATIONAL DETAILS

To investigate the CO adsorption on TiC(001) and on Au_n (n = 4, 9, 13) particles supported on TiC(001), suitable periodic slab models have been constructed. The choice for this particular size of supported particles is justified from the scanning tunneling microscopy (STM) studies which clearly show that deposition of a small amount of Au on TiC(001) results in small and rather flat clusters.[38] Note also that Au_4 only exhibits edge atoms whereas Au_9 exhibits edge, side, and inner atoms and Au_{13} consists of two atomic layers and, hence, represents a three-dimensional particle (Figure 1). The slab models have been built using the lattice parameter optimized for bulk TiC as reported in previous work.[47] Usually, the slab models contain four atomic layers, the two outermost ones are completely allowed to relax whereas the atoms in the two innermost atomic layers have been frozen at the bulk positions to provide an adequate environment.

In the following discussion we will show that the case of CO adsorption on the naked TiC(001) surface is more complex than that imagined. In order to reach definitive conclusions several unit cells of increasing size had to be used. These are 1 × 1, 2 × 1, 2 × 2, 3 × 3, and 4 × 4 and all have four atomic layers. In addition, 1 × 1 unit cell slabs with up to eight layers—always with the two innermost layers fixed—have been considered to further check for convergence. These calculations show that four atomic layers provide converged results, even for CO adsorption. In the case of the 1 × 1 model there are two C and two Ti per layer (16 atoms in total). The 2 × 1 supercell contains four C and four Ti per layer (32 atoms in total) whereas in the 2 × 2, 3 × 3, and 4 × 4 the number of C and Ti atoms per layer is 8, 18, and 32 so that the total number of atoms is 64, 144, and 256, respectively. Note that with the notation above, 1 × 1 corresponds in reality to a$(\sqrt{2} \times \sqrt{2})$/R45° unit cell if related to the minimum possible primitive cell; the use of the present notation is just for simplicity. To avoid misunderstanding, the total number of

atoms in each cell has been given explicitly (see also Figure 1 and the corresponding drawings included in the Supporting Information).

A single CO molecule has been added to the surface resulting in a coverage ranging from 1/4 to of 1/64; this is one CO molecule per 4 or 64 total surface atoms in the 1×1 or 4×4 supercells which corresponds to a CO coverage ranging from 1/2 to 1/32 if referred to the C surface atoms only. In order to provide an additional internal check, calculations have been carried out with four and nine CO molecules in the 2×2 and 3×3 supercells, respectively, which result in a 1/4 coverage as in the 1×1 one. This strategy permits us to investigate possible artifacts arising from the model. The atomic structure of the adsorbed CO molecule has been obtained from total energy minimization starting from different positions and orientations as indicated below.

To adequately model the Au/TiC systems and to guarantee that the supported nanoparticles are sufficiently separated from their periodically repeated images, two different unit cells were used. Thus, a 3×3 supercell has been used to represent the Au_4 cluster supported on TiC (001), which is the same described above concerning the interaction of CO with clean TiC(001), whereas, following previous work,[40] a 5×5 supercell has been employed to represent both Au_9 and Au_{13} supported nanoparticles. Thus, the resulting supercell models for the Au_n/TiC systems contain a total of 150 (72 C, 72 Ti, 4 Au plus CO) atoms for Au_4/TiC; 411 (200 C, 200 Ti, 9 Au plus CO) atoms for Au_9/TiC; and 415 (200 C, 200 Ti, 13 Au plus CO) atoms for Au_{13}/TiC (see Figure 1). The Au atoms were initially placed above C atoms following a previous theoretical study indicating that Au atoms supported TiC(001) prefer to interact with this site[48] but, in any case, the resulting structures were always obtained from proper geometry optimizations.

As in the case of the clean surface, a single CO molecule was added to each Au_n/TiC slab model with different starting geometries and orientation for the adsorbed CO molecule above different possible surface sites. In each case, the atomic structure was relaxed following energy minimization and once final geometries were obtained a vibrational analysis has been carried out to characterize final geometries as proper minimum energy structures in the potential energy surface. Vibrational frequencies have been obtained from explicit diagonalization of the corresponding block of the Hessian matrix with the second derivatives obtained from finite differences of analytical gradients as implemented in VASP.

The energy values have been obtained from periodic density functional calculations carried out using the PW91 form of the exchange-correlation potential[49−51] and by making use of the VASP code.[52,53] The electronic density is expanded in a plane wave basis set and the effect of the atomic cores on the valence states taken into account by the projector augmented wave (PAW) method of Blöch[54] as implemented by Kresse and Joubert.[55] It is worth recalling that this representation of the core states allows one to obtain converged results with a cutoff kinetic energy of 415 eV for the plane-wave basis set. In the present work we used PAW potentials that leave explicitly the $3d^4$ electrons of Ti, the valence electrons of C and O, and the $5d^{10}\,6s^1$ electrons of Au. For Ti these are more restrictive that those used in previous work where the $3p^6$ semicore electrons have been explicitly included.[47] Calculations of the TiC bulk modulus, a property very sensitive to the description of the cores, were carried out with the two sets of PAW differing by less than 1% indicating that the present choice is accurate enough. In order to further test the influence of exchange-correlation potential and, also, of the description of the atomic cores, additional calculations for the adsorption of CO on the bare TiC(001) surface were carried out using the 1×1 and 2×2 supercell using the RPBE functional[56] as implemented in VASP[52,53] and the same RPBE functional as implemented in the DMol^3 code.[57,58] In the latter case, calculations are of all electron type and are carried out using a numerical basis of double-ζ quality with a local basis cutoff of 5.5 Å in real space which is comparable in accuracy to a Gaussian 6-31G* basis set and all the electrons of C, O, and Ti were included.

Numerical integration in the reciprocal space was carried out using suitable Monkhorts−Pack[59] grids of special k-points for the different supercell models representing the clean TiC(001) and Au_n/TiC models with and without CO. Thus, $7 \times 7 \times 1$, $5 \times 7 \times 1$, $5 \times 5 \times 1$, and $3 \times 3 \times 1$ grids were used for the 1×1, 2×1, 2×2, and 3×3 models. Enough k-points (25 or 15) have been selected for the DMol^3 calculations in which, to allow additional degrees of freedom, the top three layers of the bulk surfaces were allowed to relax along with the adsorbates, while only the bottom layer was kept fixed at the calculated bulk lattice positions. For the larger supercell models, for instance those representing the Au_9/TiC and Au_{13}/TiC sytems, calculations have been carried out at the Γ point. A conjugated gradient algorithm with an energy criterion of 0.001 eV has been used for the convergence in the total energy which allows us to obtain an optimized structure with forces which are, in all cases, smaller than 0.03 eV Å^{-1}.

The corresponding adsorption energies have been calculated as

$$E_{ads} = E_{CO(ads)} - (E_{CO} + E_{slab})$$

where $E_{CO(ads)}$ is the energy of CO adsorbed either on the clean TiC(001) surface or on the Au_n/TiC(001) supported cluster, E_{CO} is the calculated energy of the gas phase CO molecule, and E_{slab} is the energy of the clean TiC(001) surface model or of the corresponding Au_n/TiC(001) system; with this definition, negative values of the adsorption energy indicate that adsorbed CO is more stable than the separated systems.

■ ADSORPTION OF CO ON THE CLEAN TIC(001) SURFACE

The study of CO adsorption on the clean TiC(001) is important by itself but also provides the reference for the Au_n/TiC systems described in the next section. Contrarily to the case of CO on metal surfaces for which the existing literature is quite large, the information regarding the interaction of CO on TiC is very scarce. Theoretically, two studies using cluster models were reported.[60,61] Viñes et al. also studied CO−TiC adsorption using slab models, where CO adsorption is one of the elementary steps of the water gas shift reaction on TiC(001).[62] Experimentally, temperature programmed desorption (TPD) measurements by Didziulis et al.[60] show that CO desorbs from TiC(001) at 145 K indicating a rather low adsorption energy which is estimated to be of the order of −0.5 eV. The same authors[60] report high resolution electron energy loss spectroscopy (HREELS) experiments and a CO vibrational frequency of 2120 cm^{-1} revealing a small shift of 23 cm^{-1} which is consistent with such small adsorption energy.

Table 1. Calculated (PW91) Values for the CO Adsorption Energy on TiC(001) (E_{ads} in eV) Predicted from Different Supercell Surface Models and, Hence, Different Coverage[c]

TiC(001) unit cell	no. of atoms per layer	E_{ads}	E_{dist}	$E_{dist,norm}$
1 × 1	4	−0.79	0.56	0.56
		−0.57[a]		
		−0.39[b]		
2 × 1	8	−1.07	1.12	0.56
		−0.89[a]		
		−0.83[b]		
2 × 2	16	−1.46	0.62	0.15
3 × 3	36	−1.48	0.82	0.09
4 × 4	64	−1.50	0.10	0.01

[a] RPBE/VASP. [b] RPBE/DMol^3. [c] E_{dist} is the energy of the slab model at the geometry corresponding to CO adsorption but without the CO at the surface minus the energy of the naked slab, whereas $E_{dist,norm}$ is the same as E_{dist} but normalized with respect to the number of atoms in the surface layer and taking the 1 × 1 unit cell as reference. For comparison, some RPBE values arising from calculations using a plane wave (VASP) or numerical localized basis set (DMol^3) are also reported.

Table 2. Selected Equilibrium Distances (in Å) Corresponding to CO Adsorption on TiC(001) As Predicted from PW91 Density Functional Calculations Using Different Surface Models[d]

TiC(001) unit cell	C−O	C_{surf}−CO	Ti−C_{surf}	Ti−C_{surf} (naked)[c]
1 × 1	1.18	1.33	2.70	2.21
	1.18[a]	1.33[a]	2.73[a]	2.21[a]
	1.19[b]	1.33[b]	2.61[b]	2.17[b]
2 × 1	1.19	1.32	2.88	2.20
	1.18[a]	1.32[a]	2.88[a]	2.21[a]
	1.19[a]	1.33[b]	2.79[b]	2.17[b]
2 × 2	1.19	1.32	2.54	2.22
3 × 3	1.19	1.32	2.66	2.22
4 × 4	1.19	1.32	2.74	2.22

[a] RPBE/VASP. [b] RPBE/DMol^3. [c] The small differences in this value for the PW91 calculations are mostly numerical and indicate error bars in the geometry optimization, a more accurate value is 2.21 ± 0.01 Å. [d] For comparison, some RPBE values arising from calculations using a plane wave (VASP) or numerical localized basis set (DMol^3) are also reported.

In order to find out the most stable adsorption site and geometry, many different possibilities were explored all leading to the same final result, namely, a clear preference for the adsorption on top of a surface C atom, with the CO oriented with its C-end down and its molecular axis perpendicular to the surface. It is worth pointing out that the existence of C═C═O has been reported for Mo_2C both experimentally[63] and theoretically.[64,65] This indicates that the participation of the surface C sites plays an essential role on the metal carbide surface. Adsorption on top of a surface Ti atom, also with the C-down orientation, gives a stable structure that is significantly energetically above the most favored one except perhaps when the coverage is larger than 1/2, a situation that will not be further discussed. For the smallest 1 × 1 unit cell containing four atomic layers, the PW91 computed adsorption energy (E_{ads}) is −0.79 eV, in agreement with previous results using the same approach and the same surface model.[62] Increasing the number of atomic layers up to eight leads to E_{ads} = −0.75 eV, indicating that these results converged with respect to the number of atomic layers in the slab model. This value is slightly higher than the experimental value, which is not surprising since the PW91 functional is known to exaggerate bonding interactions. In fact, the RPBE functional predicts E_{ads} = −0.57 eV (VASP) or −0.39 eV (DMol^3). Both values are in the correct direction indicating that the PW91 E_{ads} values may be overestimated by 0.2 eV with uncertainties of the same order of magnitude due to the different description of atomic cores or of the valence electrons.

So far, all results seem to be consistent and in a nice agreement with experiment. However, to our surprise, the E_{ads} value was found to be significantly larger (−1.07 eV) when calculated from the 2 × 1 unit cell and even larger (−1.46 eV) as predicted from the calculations using the 2 × 2 supercell. Further enlarging the supercell to 3 × 3 has no effect with E_{ads} = −1.47 eV, a value which is not substantially modified when using the larger 4 × 4 unit cell which leads to E_{ads} = −1.50 eV (Table 1). At first sight one may argue that the larger supercell models situations with much smaller CO coverages. However, the influence of CO coverage in the TPD adsorption peak is rather small changing from 145 K at the lowest exposure and increasing only to 139 K with increasing exposure.[60] Therefore, the calculated results for the larger supercells seem to be in contradiction with experiment. In order to further investigate the origin of this effect, calculations have been carried out for the 2 × 1 cell using the RPBE functional. The calculated RPBE E_{ads} values are slightly smaller than the PW91 ones: −0.89 eV (VASP) and −0.83 eV (DMol^3), as expected, but still noticeably larger than the values obtained for the 1 × 1 model using the same method. One may still attribute the difference between the smallest 1 × 1 model and the larger supercells to the different coverage. However, this is very unlikely since the lateral interaction between CO adsorbed molecules is less than 0.02 eV in the 1 × 1 cell. This is not surprising since the distance between adsorbed molecules is at least 3.5 Å. To further check the consistency of the models, we have carried out an additional calculation for the 2 × 2 supercell with four adsorbed CO molecules. In this way, the calculated PW91 E_{ads} becomes −1.13 eV, which is rather larger than the value obtained with the 1 × 1 cell (−0.78 eV). Hence, the coverage effect is too large since, as commented above, the TPD desorption changes with coverage from 145 to 139 K only.

Obviously, the difference between the calculated values has to have its origin in the optimized atomic structure. This is comprehensible since the only difference between the calculation for the 1 × 1 cell and the one with the 2 × 2 supercell and four adsorbed CO molecules is the number of atoms which are allowed to relax in an independent manner. To confirm this hypothesis, we analyzed in detail the geometry of the adsorbed molecule and of the underlying TiC slab model. The calculated CO distance ranges from 1.18 Å for the smallest cell to 1.19 Å for the largest one, and the distance from the substrate C directly interacting with CO, hereafter referred to as C_{surf}, to the C atom of CO varies between 1.33 Å and 1.32 Å (Table 2). Evidently, the atomic structure of atomic CO cannot be the origin of the difference in E_{ads} calculated for the different supercell models. We are then left with the substrate atomic structure as only possibility. A careful analysis confirms that this is the case. In fact, the presence of CO strongly distorts the underlying TiC surface up to the point that the distance between a Ti atom in the second

layer and the C_{surf} atom changes from 2.21 ± 0.02 Å, depending on the supercell, to 2.70 Å for the 1 × 1 supercell with four atomic layers (2.77 Å when eight atomic layers are included) and to 2.66 Å for the 3 × 3 supercell. Clearly, the interaction between CO and the TiC surface is very strong, to the point that the C_{surf} moves almost 0.5 Å outward toward the vacuum. The distortion is so large that a 1 × 1 cell cannot account for the necessary relaxation, and this is why the calculated adsorption energy changes with the supercell model.

From the previous discussion various firm conclusions can be extracted. First, the CO interaction with the TiC(001) surface is strong with a large deformation of the substrate which leads to a periodicity different from the one corresponding to the CO adlayer only. The adsorption energy is the result of the strong bonding between the C_{surf} and the CO molecule, which with a C_{surf}—C distance of 1.32 Å is in the range of double bonds (Table 2). However, the energy gain from such strong interaction is counteracted by the energy cost to deform the surface. For the 1 × 1 surface model, this energy cost is 0.56 eV (see E_{dist} in Table 1) which almost explains the difference between the E_{ads} results for the 1 × 1 and 2 × 2 supercells. In the case of the 2 × 2 and larger cells, the energy cost is much smaller because the additional degrees of freedom allow the system to relax sufficiently. This is clear from the results in Table 1 for E_{dist}, especially when normalized with respect to the number of atoms in the surface ($E_{dist,norm}$). For the 3 × 3 and 4 × 4 surface models $E_{dist,norm}$ is less than 0.1 eV. The result is a moderate value of the adsorption energy of −1.5 eV at the PW91 level of theory or an estimate of approximately −1.0 eV at the RPBE one. This is still larger than the value inferred from TPD experiments, and the origin of the difference can be attributed either to the limitations of the present exchange-correlation potentials and, also, to conditions of the single crystal sample used at the experiments. For instance, it may well be that the experimental conditions for the extremely low coverage represented in the 3 × 3 and 4 × 4 surface models is hardly achievable. While the final value of the adsorption energy of CO on TiC may be regarded somehow as an open issue, the nature of the interaction and the adsorbate induced relaxation of the surface is out of question.

Let us now turn our attention to the vibrational frequency of adsorbed CO. The PW91 calculated value for this property in the gas phase is 2133 ± 8 cm^{-1} at an equilibrium distance of 1.143 Å. The error bar of 8 cm^{-1} is the statistical error arising from the calculation of the CO molecule in the different boxes used to accommodate the different supercell models as is due to the use of a slightly different number of plane waves in each case. Both are close to the experimental values of 2169 cm^{-1} for the harmonic vibrational frequency and 1.128 Å for the internuclear equilibrium distance.[66] Note that the experimental fundamental frequency is 2143 cm^{-1}. Experimental shifts consider the fundamental frequency as the reference whereas theoretical frequencies and shifts in this article are always harmonic. For the 1 × 1 supercell we compute a value of 2083 cm^{-1} for the CO stretching (2025 cm^{-1} from DMol^3 calculations with the RPBE functional) which represents a negative shift of −50 cm^{-1} on the harmonic frequency (a larger shift of −97 cm^{-1} when considering the DMol^3 result of free CO of 2128 cm^{-1}). On the other hand, HREELS experiments by Disziulis et al. find a loss at 2120 cm^{-1} which is associated with the stretch of the adsorbed CO molecule. This implies a shift of −23 cm^{-1} with respect to the fundamental frequency of CO (2143 cm^{-1}). The signs of the calculated and experimental shifts are equal and both are relatively small indicating that the CO molecule remains neutral. This is in agreement with the covalent nature of the chemical bond between C_{surf} and CO inferred from the calculations. This statement is also supported by the calculated value of the C_{surf}—C stretching mode which for the physically meaningful supercells appears in the 1157−1191 cm^{-1} range depending on the supercell (Table 3). This is quite large for a frustrated translation and indicative of the formation of a strong covalent bond. Interesting enough a feature at 1190 cm^{-1} is observed in the HREELS experiments which has not been previously assigned and which one can tentatively assign to the C_{surf}—C stretching mode.

Table 3. Selected PW91 Vibrational Frequencies (cm^{-1}) for CO Adsorbed on TiC(001) As Calculated from Different Supercell Surface Models and, Hence, Different Coverage

	TiC(001) unit cell				
assignment	1 × 1	2 × 1	2 × 2	3 × 3	4 × 4
stretching CO	2083	2045	2040	1999	2020
stretching C_{surf}—C	1120	1164	1191	1157	1173
CO frustrated trans. X	617	622	581	588	582
CO frustrated trans. Y	573	595	580	585	576
CO tilting XZ	446	448	439	389	405
CO tilting YZ	380	429	422	389	399

In the view of the differences in adsorption energy encountered with the different supercell models, we find it convenient to investigate also the effect of the surface model on the vibrational frequencies. Table 3 presents the values for several vibrational modes which are related to CO motion. The first two modes correspond to the CO and C_{surf}—CO stretching frequencies which are strongly coupled. The CO stretching frequency decreases from 2083 cm^{-1} for the 1 × 1 model to 2020 cm^{-1} for the largest 4 × 4 supercell with small variations depending on the model. The C_{surf}—CO frequency varies in a similar way indicating that the two modes are coupled; the calculated value for the largest 4 × 4 unit cell is of 1170 cm^{-1}, even closer to the experimental feature commented above. The next four modes correspond to frustrated translation of CO in direction parallel to the surface and to the CO tilting modes. Note that these four low-frequency modes form two groups of almost degenerate frequencies as one would expect from symmetry. The degeneration is not complete because of the small but noticeable surface rumpling of the Ti and C atoms.[47]

The results presented so far indicate that the interaction of CO on the bare TiC(001) is more complex than imagined from the rather simple nature of the interacting systems. It is clear that some specific results require validation from more sophisticated calculations, perhaps using hybrid functionals, but also claim for further experiments. Nevertheless, they also provide the reference framework for the main goal of the present paper which is the study of the interaction of CO with Au nanoparticles supported on TiC(001).

■ ADSORPTION OF CO ON THE AU_N (N = 4, 9, 13) NANOPARTICLES SUPPORTED ON TIC(001)

The electronic structure of small Au clusters supported on TiC(001) is strongly polarized by the underlying substrate as shown by previous work from both theory and experiment, the

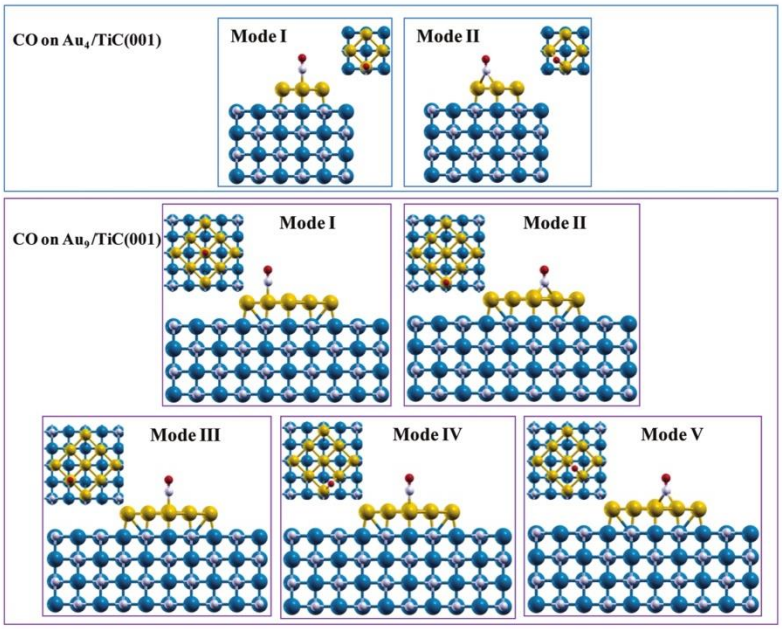

Figure 2. Possible adsorption modes for CO on the Au_4 (top panel) and Au_9 (bottom panel) particles supported on TiC(001). Note that the C-down orientation is always favored and that only a portion of the unit cell is represented. The color code used in the drawing is C (white), Ti (blue), Au (yellow), and O (red).

reason being the Au ↔ C interactions.[37] This electron polarization leads to a very active catalyst for DeSOx reactions[38,41] and for the dissociation of molecular oxygen[40] and molecular hydrogen.[42] Can the same phenomenon be responsible for the high chemical activity observed for Au/TiC during CO oxidation?[33,36] To get further insight into the new chemistry of Au particles supported on TiC(001), we report here results for the interaction of these supported particles with CO taken as a probe molecule. The particles chosen to carry out this study are representative of those found in experiments carried out in ultrahigh vacuum using a TiC(001) single crystal where Au coverage is of the order of 0.1 ML.[38] Several adsorption modes have been tried with the CO molecules starting from C down, O down, or atoms parallel to the surface. The C-down orientation is always preferred although not all initial structures correspond to distinct stable structures on the potential energy surface. Moreover, since the nanoparticles supported on TiC(001) are small enough to be considered the so-called scalable regime, where properties scale linearly with particle size, it is not surprising that each particle presents some particularities although some common trends are also apparent.

For the supported Au_4 particle, two final stable geometries are found which correspond to CO on top of a Au atom with the CO bond perpendicular to the surface in a C-down orientation (mode I in Figure 2) and a similar one with CO on a bridge site between two Au atoms (mode II in Figure 2). The on-top site leads to the most stable interaction with a calculated value of −1.30 eV for the adsorption energy and a CO stretching frequency of 2087 cm^{-1} (Table 4). The CO molecule binds quite well to the supported Au cluster, but the

Table 4. Adsorption Energy (E_{ads} in eV) of CO on the Au_n/TiC(001) (n = 4, 9, 13) Systems, C−O and Au−C Internuclear Equilibrium Distances (d_{C-O} and d_{Au-C} in Å), and CO Stretching Frequency (cm^{-1}) for the Adsorption Modes Corresponding to Energy Minima with Respect to the CO Degrees of Freedom [a]

	E_{ads}	d_{CO}	d_{AuC}	ν
		Au_n/TiC (n = 4)		
mode I	−1.30	1.16	1.95	2087
mode II	−0.92	1.18	2.16	1905
		Au_n/TiC (n = 9)		
mode I	−0.75	1.15	1.98	2115
mode II	*a*			
mode III	−1.10	1.15	1.96	2110
mode IV	−0.89	1.17	2.20	1939
mode V	−0.66	1.18	2.11	1933
		Au_n/TiC (n = 13)		
mode I	−0.68	1.16	1.99	2090
mode II	−0.60	1.17	2.17	1979
mode III	−0.69	1.19	2.16	1783
mode IV	−0.96	1.17	2.02	1987

[a] This initial mode does not lead to a stable different structure.

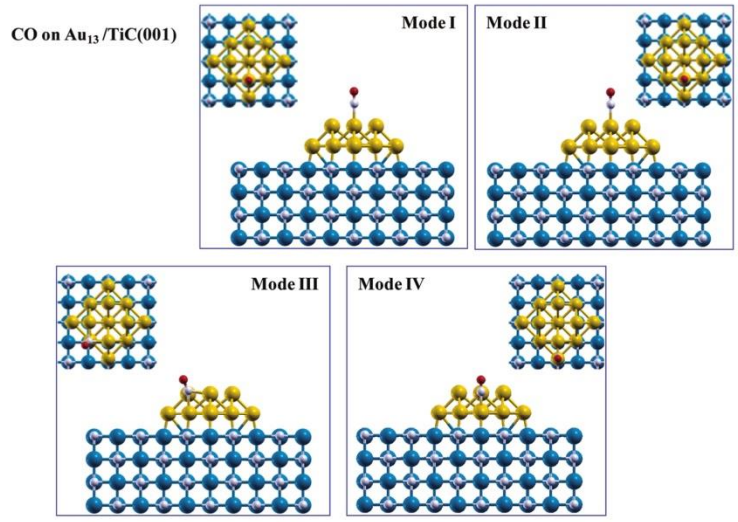

Figure 3. Final optimized adsorption modes for CO on the Au_{13} particle supported on TiC(001), for a more detailed description see text. Note that the C-down orientation is always favored. The color code used in the drawing is C (white), Ti (blue), Au (yellow), and O (red).

adsorption energy is somewhat smaller than that seen for low coverages of CO on the bare TiC(001) substrate (−1.50 eV). The difference in adsorption energies implies that CO will always bind preferentially to the TiC substrate, but CO molecules that hit the Au clusters may remain bound to the admetal and react with other adsorbates. In Table 4, the vibrational frequency of CO is only slightly perturbed upon interaction with Au (except for the bridge site where, as expected, it decreases considerably) with a red shift of -46 cm^{-1} with respect to the calculated value for gas phase CO. This is even smaller than the one calculated for CO on bare TiC(001), as expected from the weaker interaction with the supported particle than with bare substrate. In order to confirm this interpretation, we computed the adsorption energy of CO above various C sites of the TiC(001) surface model containing already a supported Au_4 particle. The most stable site corresponds to the interaction of CO directly with a C atom opposite to a Au atom of the Au_4 particle. At this site, the calculated value of the adsorption energy is of −1.43 eV which is in agreement with the value calculated for the larger supercells as discussed in the previous section (see also Table 1). Further, at this site, the CO stretching frequency becomes 2022 cm^{-1} which is also in agreement with the values obtained for the large TiC supercell slab models (Table 3). These results confirm the accuracy of the results presented on the previous section for CO on bare TiC(001) and, in addition, indicate that the CO/TiC(001) interaction is very local.

Let us now focus on the interaction of CO with the Au_9 supported particle. The Au_9 supported particle is also a planar structure consisting of just one layer of Au atoms. However, at variance of Au_4, it exhibits more potential adsorption sites, three different atop sites are possible with CO above a Au atom either in the particle center, side or corner with Au−Au coordination numbers of 4, 3, and 2, respectively, and various bridge sites are also possible (Figure 2). Results in Table 4 indicate that the most stable site for CO on Au_9 supported on TiC(001) is also an atop site. However, this does not correspond to the less coordinated Au atom (mode II in Figure 2) but to the Au atom at one side of the square formed by the nine Au atoms. The interaction with the least coordinated Au atoms is probably stronger but it does also introduce a significant distortion of the supported particle displacing the Au atoms from the underlying C atoms. On the other hand, the interaction of CO on top of one Au atom as in mode II preserves the particle most favorable interaction with the substrate and results in the larger value of the adsorption energy (−1.10 eV). Note that this, although substantial, is again smaller than the value corresponding to CO on the bare TiC surface, indicating that a large population of CO will cover the supported Au particle only at sufficiently large coverages of the admolecule. At this site the calculated value for the CO stretching frequency is of 2110 cm^{-1} resulting in a shift of -23 cm^{-1} with respect to gas phase CO. To further check the consistency of this result, we also calculated the adsorption energy of CO on top of a C atom of the TiC substrate of the model containing the supported Au_9 nanoparticle. The calculated value of −1.37 eV is again close enough to the one corresponding to the naked surface indicating that the presence of the supported Au particle does not affect the electronic structure and bonding capability of the available free C sites of the TiC(001) surface.

Finally, we consider the larger Au_{13} supported particles consisting of two atomic layers with nine and four atoms, respectively. In this case, several initial geometries have been explored and four different stable structures were found after geometry optimization. These are schematically displayed in Figure 3 and the relevant geometrical data reported in Table 4. The preferred adsorption mode for CO (mode I in Figure 3) involves also direct interaction between CO an a Au atom on the topmost layer of the Au_{13} nanoparticle. For this adsorption mode, the adsorption energy is somewhat smaller than for the

supported Au_4 and Au_9 particles and, consequently, smaller than the one corresponding to the adsorption of CO on the bare TiC(001) surface or on C sites of the TiC(001) surface covered by Au nanoparticles. The other stable structures involve the interaction of CO with a bridge site formed by two Au atoms on the topmost layer (mode II in Figure 3) or the direct interaction between CO and a Au atom (modes III and IV in Figure 3) which are equivalent to mode III and mode II for Au_9 on TiC. Thus, the only difference between mode III and mode IV for CO on Au_{13}/TiC is the number of Au atoms surrounding the Au atoms directly bonded to CO. In mode III, this Au atom has two nearest neighbor Au atoms in the bottom Au layer and two in the topmost layer, whereas in mode IV the Au atom bonded to CO has also two nearest neighbor Au atoms in the bottom Au layer but only one in the topmost layer. Overall, the largest CO adsorption energies in Table 4 increase following the sequence: Au_{13} (−0.96 eV) < Au_9 (−1.10 eV) < Au_4 (−1.3 eV). All the supported Au clusters are able to bind the CO molecule well.

Note also that the calculated vibrational frequency for CO adsorbed at the most stable sites of the different Au nanoparticles is of the same order but does not directly correlate with the adsorption energy. Thus, the information that one can extract from HREELS or similar experiments on these systems is at most the coordination mode, although there is some indication of back-donation from the Au nanoparticle to CO, as expected from the polarization of the Au nanoparticle induced by the underlying substrate.[37]

From the discussion above we can extract some firm conclusions regarding the interaction of CO with Au nanoparticles supported on TiC(001). In all cases, the most stable situation involves the direct bonding between the CO molecule and one Au atom. However, the adsorption energy decreases with increasing the particle size. Moreover, the adsorption energy is always smaller than the one corresponding to CO on the bare TiC(001) surface, even when supported Au particles are present. Furthermore, the interaction of CO on the Au nanoparticles supported on TiC(001) induces a relatively small red shift of the CO stretching frequency which, in this way, does not provide any essential new information. In this work, the focus on CO as an adsorbate was motivated by the good chemical activity of Au/TiC for the low temperature oxidation of carbon monoxide ($CO + 0.5O_2 \rightarrow CO_2$).[33,36] On the basis of this work and our previous study for the adsorption of O_2 on Au/TiC(001),[37] we can conclude that the good performance of the Au/TiC system in CO oxidation is probably a direct consequence of the ability that the Au in contact with TiC has to activate the O_2 molecule rather than binding CO. On the supported Au clusters, there is a large weakening of the O−O bonds and the CO for the formation of CO_2 may come from TiC or from the Au on the surface. Since the supported Au interacts well with O_2 and CO, it can perform all the steps for the CO oxidation reaction by itself, with the TiC having an indirect participation through the modification of the electronic properties of gold.

SUMMARY AND CONCLUSIONS

The interaction of CO with the bare TiC(001) surface and with Au_n (n = 4, 9, 13) nanoparticles supported on the same TiC(001) surface has been studied by means of periodic density functional theory based calculations using slab supercell models containing up to 400 atoms. The particles used are representative of those existing upon evaporation of Au atoms on TiC(001) under ultrahigh-vacuum conditions as revealed by STM experiments.[38]

For the adsorption of CO on the bare TiC(001) surface, several models have been used which all reveal that bonding of CO to this surface at relatively low coverage involves the direct interaction with the CO molecule and a C surface (C_{surf}) atom, the interaction with Ti sites being less favorable unless the CO coverage becomes very large although this situation has not been investigated in detail. The CO interaction directly above C sites involves a significantly large deformation of the underlying surface with the distance between C_{surf} and the Ti atoms in the second layer being rather elongated from the corresponding distance for the naked surface. This deformation causes the calculated adsorption energy to vary significantly with the unit cell model used to represent the surface. The reason is that large supercell models contain a larger number of structural degrees of freedom and thus allow for a better relaxation of the substrate in response to the presence of the adsorbate. The calculated adsorption energy at coverage of C sites of 50% is of roughly 0.5−0.8 eV depending on the exchange-correlation potential, atomic core description, and basis set. While this value is in agreement with the one extracted from the TPD experiments of Didziulis et al.,[60] one must realize that it arises from a unit cell which is too small to appropriately describe the adsorbate induced relaxation. In fact, for models representing a coverage of the C sites of 1/8 (0.125 ML) or lower, the calculated adsorption energy increases up to 1.0−1.4 eV, again depending on the computational method. The reason for this enhancement of E_{ads} is the possibility to better accommodate the substrate relaxation induced by the presence of CO and cannot be attributed to a decrease on the lateral interaction between adsorbed CO molecules. This larger value of E_{ads} is not in agreement with experiment and it is difficult to assess the origin of the difference although it is consistently predicted by different DFT methods. Hence, it is unlikely that the situation here is similar to the case of CO on MgO(001) where standard exchange-correlation functionals do not provide a satisfactory description, even qualitatively (see for instance ref 67 and references therein). Therefore, the difference between theory and experiment may be due to difficulties in the experiment to reach such low coverage conditions or to some problems with the TiC(001) single crystal sample. This point of view is supported with the calculation of the stretching vibrational frequency of CO which predicts a shift which is larger than the one measured in the experiments and increases with decreasing coverage. Clearly, the interaction of CO with TiC(001) appears to be more complex than anticipated from naïve arguments and claims for further work from both theory and experiment.

The interaction of CO with the Au nanoparticles exhibits some common features and, also, well-defined trends. Thus, the CO molecule always prefers to interact directly with a Au atom and, in general, low coordinated Au atoms are preferred, as expected. However, the interaction of CO with the supported Au particles is somewhat weaker than with the naked surface and decreases with increasing the particle size. This is also consistent with a rather small red shift of the vibrational frequency of the adsorbed CO molecule that also decreased with increasing the particle size. These findings have strong implications for the use of Au/TiC systems in catalytic reactions involving CO. In fact, the present results strongly suggest that any additional reaction with the adsorbed CO, such as its direct hydrogenation, is certainly a very likely possibility. Au/TiC is to be expected to

act as a bifunctional catalyst, where Au provides a source of atomic H which further reacts with CO adsorbed on the TiC terraces. Additional work is necessary to investigate these possibilities and is being currently carried out in our laboratories.

■ ASSOCIATED CONTENT

Supporting Information. Figures displaying all calculated structures. This material is available free of charge via the Internet at http://pubs.acs.org.

■ AUTHOR INFORMATION

Corresponding Author
*E-mail: francesc.illas@ub.edu.

■ ACKNOWLEDGMENT

G.G.A. thanks Universitat Rovira i Virgili, for supporting his predoctoral research, E.F. thanks the Programa sostenibilidad 2011-2012 Universidad de Antioquia for supporting her research, and F.I. acknowledges support received through the "2009 ICREA Academia" prize for excellence in research. Financial support has been provided by the Spanish MICINN (Grants FIS2008-02238 and CTQ2008-06549-C02-01) and in part by Generalitat de Catalunya (Grants 2009SGR1041, 2009SGR00462, and XRQTC). Computational time has been generously provided by the Barcelona Supercomputing Center. The research carried out at BNL was supported by the US Department of Energy, Chemical Sciences Division (Contract No DE-AC02-98CH10886).

■ REFERENCES

(1) Haruta, M. *Catal. Today* **1997**, *36*, 153.
(2) Valden, M.; Lai, X.; Goodman, D. W. *Science* **1998**, *281*, 1647.
(3) Hashmi, A. S. K.; Hutchings, G. J. *Angew. Chem., Int. Ed.* **2006**, *45*, 7895.
(4) See also the reviews in the special issue dedicated to chemistry of nanogold. *Chem. Soc. Rev.* **2008**, 37.
(5) Hughes, M. D.; Xu, Y. J.; Jenkins, P.; McMorn, P.; Landon, P.; Enache, D. I.; Carley, A. F.; Attard, G. A.; Hutchings, G. J.; King, F.; Stitt, E. H.; Johnston, P.; Griffin, K.; Kiely, C. J. *Nature* **2005**, *437*, 1132.
(6) Lopez, N.; Janssens, T. V. W.; Clausen, B. S.; Xu, Y.; Mavrikakis, M.; Bligaard, T.; Nørskov, J. K. *J. Catal.* **2004**, *223*, 232.
(7) Corma, A.; Boronat, M.; González, S.; Illas, F. *Chem. Commun.* **2007**, 3371.
(8) Turner, M.; Golovko, V. B.; Vaughan, O. P. H.; Abdulkin, P.; Berenguer-Murcia, A.; Tikhov, M. S.; Johnson, B. F. G.; Lambert, R. M. *Nature* **2008**, *454*, 981.
(9) Roldán, A.; González, S.; Ricart, J. M.; Illas, F. *ChemPhysChem* **2009**, *10*, 348.
(10) Roldán, A.; Ricart, J. M.; Illas, F. *Theor. Chem. Acc.* **2011**, *128*, 675.
(11) Fu, Q.; Saltsburg, H.; Flytzani-Stephanopoulos, M. *Science* **2003**, *301*, 935.
(12) Rodriguez, J. A.; Ma, S.; Liu, P.; Hrbek, J.; Evans, J.; Perez, M. *Science* **2007**, *318*, 1757.
(13) Corma, A.; Serna, P. *Science* **2006**, *313*, 332.
(14) Boronat, M.; Concepción, P.; Corma, A.; González, S.; Illas, F.; Serna, P. *J. Am. Chem. Soc.* **2007**, *129*, 16230.
(15) Carrettin, S.; Concepcion, P.; Corma, A.; Nieto, J. M. L.; Puntes, V. F. *Angew. Chem., Int. Ed.* **2004**, *43*, 2538.
(16) Hwu, H. H.; Chen, J. G. *Chem. Rev.* **2005**, *105*, 185.
(17) Levy, R. B.; Boudart, M. *Science* **1973**, *181*, 547.
(18) Claridge, B.; York, A. P. E.; Brungs, A. J.; Marquez-Alvarez, C.; Sloan, J.; Tsang, S. C.; Green, M. L. H. *J. Catal.* **1998**, *180*, 85.
(19) Brungs, A. J.; York, A. P. E.; Green, M. L. H. *Catal. Lett.* **1999**, *57*, 65.
(20) Chianelli, R. R.; Berhault, G. *Catal. Today* **1999**, *53*, 357.
(21) Rodriguez, J. A.; Liu, P.; Dvorak, J.; Jirsak, T.; Gomes, J.; Takahashi, Y.; Nakamura, K. *Surf. Sci.* **2003**, *543*, L675.
(22) Oyama, S. T. *Catal. Today* **1992**, *15*, 179.
(23) Rodriguez, J. A.; Dvorak, J.; Jirsak, T. *J. Phys. Chem. B* **2000**, *104*, 11515.
(24) St. Clair, T. P.; Oyama, S. T.; Cox, D. F. *Surf. Sci.* **2002**, *511*, 294.
(25) Liu, P.; Rodriguez, J. A. *J. Chem. Phys.* **2003**, *119*, 10895.
(26) Diaz, B.; Sawhill, S. J.; Bale, D. H.; Main, R.; Phillips, D. C.; Korlann, S.; Self, R.; Bussell, M. E. *Catal. Today* **2003**, *86*, 191.
(27) Schwartz, V.; da Silva, V. T.; Oyama, S. T. *J. Mol. Catal. A: Chem.* **2000**, *163*, 251.
(28) Liu, P.; Rodriguez, J. A.; Asakura, T.; Gomes, J.; Nakamura, K. *J. Phys. Chem. B* **2005**, *109*, 4575.
(29) Furimsky, E. *Applied Catal., A* **2003**, *240*, 1.
(30) Isaev, E. I.; Simak, S. I.; Abrikosov, I. A.; Ahuja, R.; Vekilov, Yu. Kh.; Katsnelson, M. I.; Lichtenstein, A. I.; Johansson, B. *J. Appl. Phys.* **2007**, *101*, 123519.
(31) Bazhanov, D. I.; Mutigullin, I. V.; Knizhnik, A. A.; Potapkin, B. V.; Bagaturyants, A. A.; Fonseca, L. R. C.; Stoker, M. W. *J. Appl. Phys.* **2010**, *107*, 083521.
(32) Vojvodic, A.; Hellman, A.; Ruberto, C.; Lundqvist, B. I. *Phys. Rev. Lett.* **2009**, *103*, 146103.
(33) Ono, L. K.; Sudfeld, D.; Roldan Cuenya, B. *Surf. Sci.* **2006**, *600*, 5041.
(34) Naitabdi, A.; Ono, L. K.; Roldan-Cuenya, B. *Appl. Phys. Lett.* **2006**, *89*, 043101.
(35) Schweitzer, N. M.; Schaidle, J. A.; Ezekoye, O. K.; Pan, X.; Linic, S.; Thompson, L. T. *J. Am. Chem. Soc.* **2011**, *133*, 2378.
(36) Ono, L. K.; Roldán-Cuenya, B. *Catal. Lett.* **2007**, *113*, 86.
(37) Rodriguez, J. A.; Viñes, F.; Illas, F.; Liu, P.; Takahashi, Y.; Nakamura, K. *J. Chem. Phys.* **2007**, *127*, 211102.
(38) Rodriguez, J. A.; Liu, P.; Viñes, F.; Illas, F.; Takahashi, Y.; Nakamura, K. *Angew. Chem., Int. Ed.* **2008**, *47*, 6685.
(39) Rodriguez, J. A.; Liu, P.; Viñes, F.; Illas, F.; Takahashi, Y.; Nakamura, K. *J. Am. Chem. Soc.* **2009**, *131*, 8592.
(40) Rodriguez, J. A.; Feria, L.; Jirsak, T.; Takahashi, Y.; Nakamura, K.; Illas, F. *J. Am. Chem. Soc.* **2010**, *132*, 3177.
(41) Feria, L.; Rodriguez, J. A.; Jirsak, T.; Illas, F. *J. Catal.* **2011**, *279*, 352.
(42) Florez, E.; Gomez, T.; Liu, P.; Rodriguez, J. A.; Illas, F. *ChemCatChem* **2010**, *2*, 1219.
(43) Sheppard, N.; Nguyen, T. T. In *Advances in Infrared and Raman Spectroscopy*; Hester, R. E., Clark, R. J. H., Eds.; Heyden and Son: London and New York, 1978; Vol. 5, p 67.
(44) Woodruff, D. P.; Bradshaw, A. M. *Rep. Prog. Phys.* **1994**, *57*, 1029.
(45) Illas, F.; Zurita, S.; Marquez, A. M.; Rubio, J. *Surf. Sci.* **1997**, *376*, 279.
(46) Sterrer, M.; Yulikov, M.; Risse, T.; Freund, H.-J.; Carrasco, J.; Illas, F.; di Valentin, C.; Giordano, L.; Pacchioni, G. *Angew. Chem., Int. Ed.* **2006**, *45*, 2633.
(47) Viñes, F.; Sousa, C.; Liu, P.; Rodriguez, J. A.; Illas, F. *J. Chem. Phys.* **2005**, *122*, 174709.
(48) Rodriguez, J. A.; Viñes, F.; Illas, F.; Liu, P.; Takahashi, Y.; Nakamura, K. *J. Chem. Phys.* **2007**, *127*, 211102.
(49) Perdew, J. P.; Wang, J. A. *Phys. Rev. B* **1992**, *45*, 13244.
(50) Perdew, J. P.; Chevary, J. A.; Vosko, S. H.; Jacson, K. A.; Pederson, M. R.; Singh, D. J.; Fiolhais, C. *Phys. Rev. B* **1992**, *46*, 6671.
(51) Perdew, J. P.; Chevary, J. A.; Vosko, S. H.; Jacson, K. A.; Pederson, M. R.; Singh, D. J.; Fiolhais, C. *Phys. Rev. B* **1993**, *48*, 4978.
(52) Kresse, G.; Hafner, J. *Phys. Rev. B* **1993**, *47*, 558.
(53) Kresse, G.; Furthmuller, J. *Phys. Rev. B* **1996**, *54*, 11169.
(54) Blöch, P. E. *Phys. Rev. B* **1994**, *50*, 17953.
(55) Kresse, G.; Joubert, D. *Phys. Rev. B* **1999**, *59*, 1758.

(56) Hammer, B.; Hansen, L. B.; Nørskov, J. K. *Phys Rev B* **1999**, *59*, 7413.
(57) Delley, B. *J. Chem. Phys.* **1990**, *92*, 508.
(58) Delley, B. *J. Chem. Phys.* **2000**, *113*, 7756.
(59) Monkhorst, H. J.; Pack, J D. *Phys. Rev. B* **1976**, *13*, 5188.
(60) Didziulis, S. V.; Frantz, P.; Fernandez-Torres, L. C.; Guenard, R. B.; El-bjeirami, O.; Perry, S. S. *J. Phys. Chem. B* **2001**, *105*, 5196.
(61) Didziulis, S. V.; Butcher, K. D.; Perry, S. S. *Inorg. Chem.* **2003**, *43*, 7766.
(62) Viñes, F.; Rodriguez, J. A.; Liu, P.; Illas, F. *J. Catal.* **2008**, *260*, 103.
(63) Wu, W.; Wu, Z.; Liang, C.; Chen, X.; Ying, P.; Li, C. *J. Phys. Chem. B* **2003**, *107*, 7088.
(64) Ren, J.; Huo, C.-F.; Wang, J.; Li, Y.-W.; Jiao, H. *Surf. Sci.* **2005**, *596*, 212.
(65) Liu, P.; Rodriguez, J. A. *J. Phys. Chem. B* **2006**, *110*, 19418.
(66) Huber, K. P.; Herzberg, G. *Molecular Spectra and Molecular Structure, Constants of Diatomic Molecules*; Van Nostrand-Reinhold: New York, 1979; Vol. 4.
(67) Valero, R.; Gomes, J. R. B.; Truhlar, D. G.; Illas, F. *J. Chem. Phys.* **2008**, *129*, 124710.

ELECTRONIC SUPPLEMENTARY INFORMATION

Theoretical study of the interaction of CO on TiC(001) and Au nanoparticles supported on TiC(001): probing the nature of the Au/TiC interface

Gian Giacomo Asara,[1,2] Leticia Feria,[1] Elizabeth Florez,[1,3] Josep M. Ricart,[2] Ping Liu,[4] José A. Rodriguez,[4] and Francesc Illas[1*]

1) Departament de Química Física & IQTCUB, Universitat de Barcelona, C/ Martí i Franquès 1, 08028 Barcelona, Spain

2) Departament de Química Física i Inorgànica, Universitat Rovira i Virgili, C/ Marcel·lí Domingo s/n, 43007 Tarragona, Spain

3) Instituto de Química, Universidad de Antioquia, A.A. 1226, Medellín, Colombia

4) Chemistry Department, Brookhaven National Laboratory, Upton, NY 11973 (USA)

[*] Corresponding author: e-mail francesc.illas@ub.edu

Figure S1.- The different 4 layer slab models used to represent TiC(**00**1)

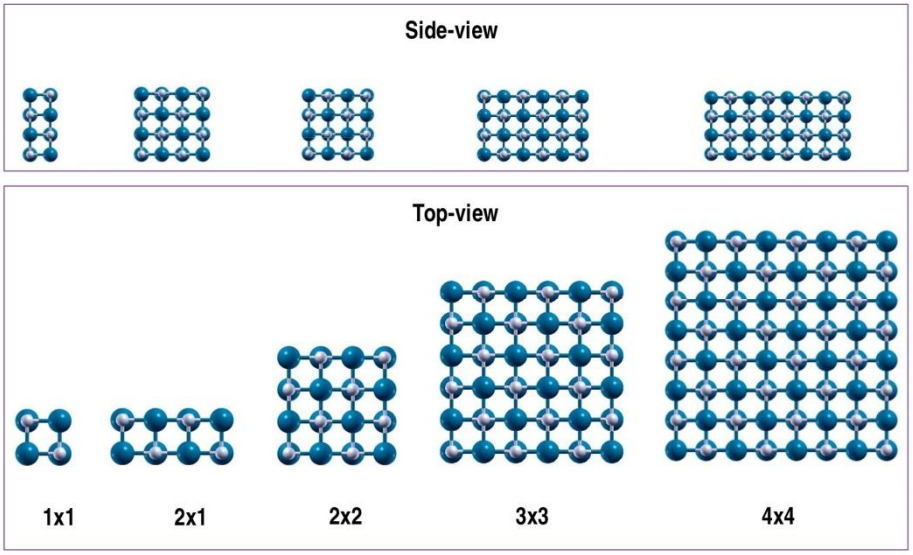

Figure S2.- Different 1×1 slab models used to represent TiC(**00**1)

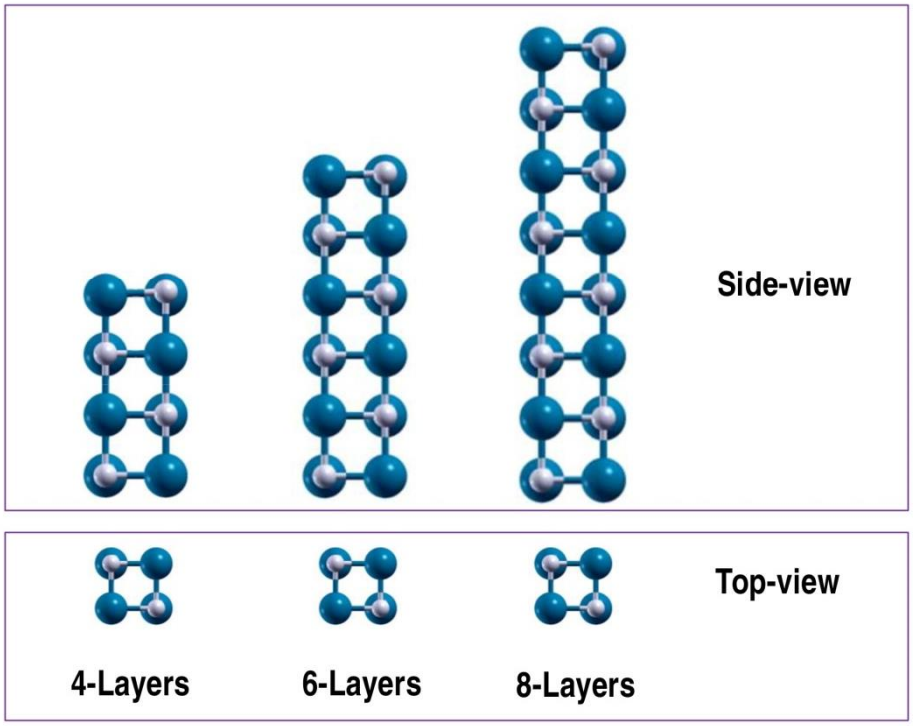

Figure S3.- The different 4 layer slab models used to study the interaction of CO with the TiC(**00**1) surface.

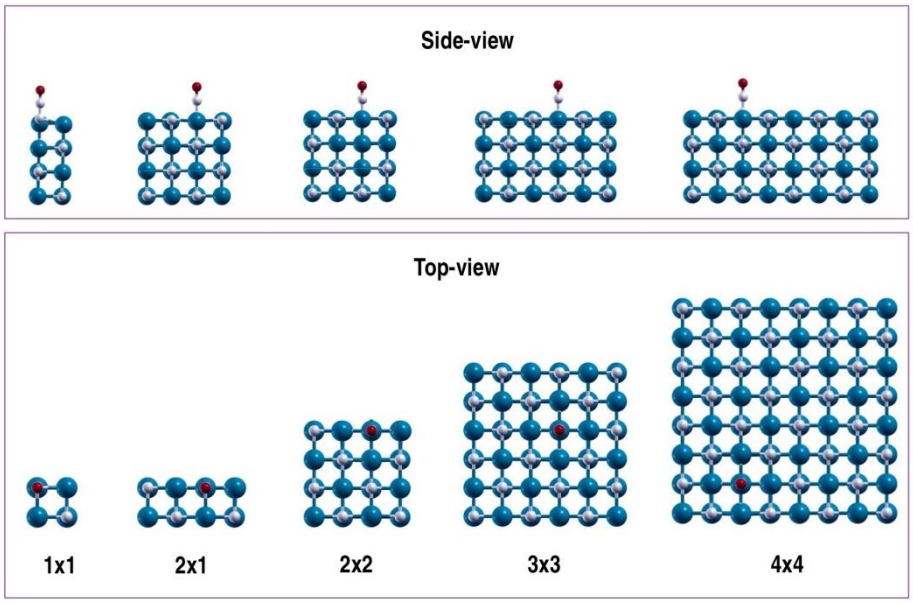

Figure S4.- The slab models used to study the influence of the number of atomic layers on the adsorption of CO on TiC(**00**1).

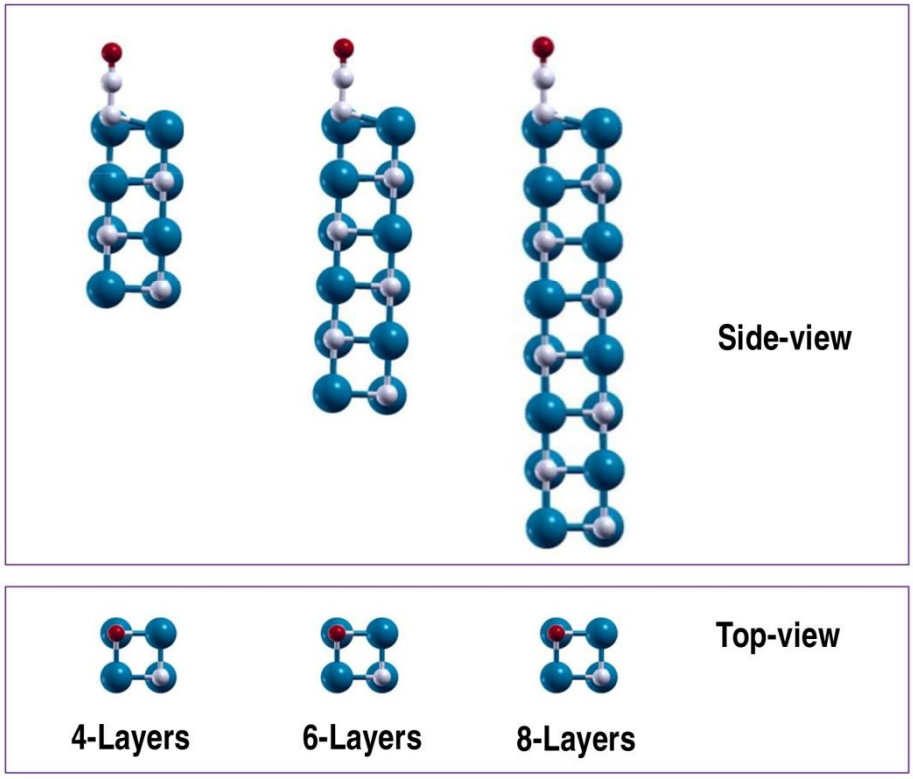

Figure S5.- The different 4 layer slab models used to study the influence of coverage effects on the adsorption of CO on TiC(**00**1).

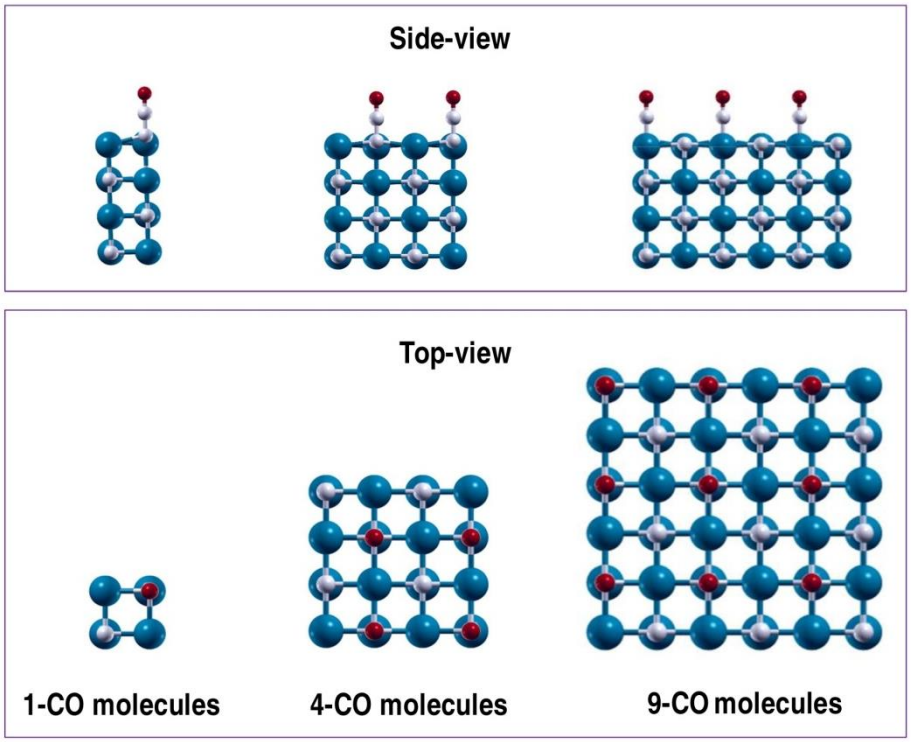

Figure S6.- The different layer slab models used to represent Au_4, Au_9 and Au_{13} nanoparticles supported on TiC(**00**1)

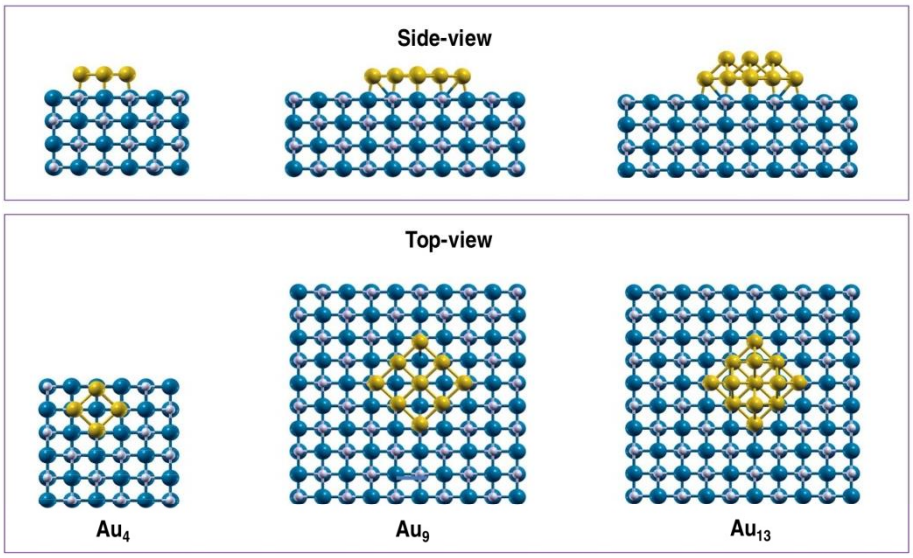

Surface Science 613 (2013) 63–73

Contents lists available at SciVerse ScienceDirect

Surface Science

journal homepage: www.elsevier.com/locate/susc

Theoretical and experimental study of the interaction of CO on TiC surfaces: Regular versus low coordinated sites

Barry P. Mant [a,b,c], Gian Giacomo Asara [a,d], James A. Anderson [c], Narcis Homs [b,e], Pilar Ramírez de la Piscina [b], Sònia Rodríguez [b], Josep M. Ricart [d], Francesc Illas [a,*]

[a] Departament de Química Física & IQTCUB, Universitat de Barcelona, C/Martí i Franquès 1, 08028 Barcelona, Spain
[b] Departament de Química Inorgànica & IN2UB, Universitat de Barcelona, C/Martí i Franquès 1, 08028 Barcelona, Spain
[c] Surface Chemistry and Catalysis Group, Department of Chemistry, University of Aberdeen, Aberdeen AB24 3UE, Scotland, UK
[d] Departament de Química Física i Inorgànica, Universitat Rovira i Virgili, C/Marcel·lí Domingo s/n, 43007 Tarragona, Spain
[e] Departament de Materials i Catàlisi, Catalonia Institute for Energy Research (IREC), C/Jardins de les dones de negre 1, 08930 Barcelona, Spain

ARTICLE INFO

Article history:
Received 20 November 2012
Accepted 8 March 2013
Available online 16 March 2013

Keywords:
TiC
CO
DFT
Low coordinated sites

ABSTRACT

The adsorption of CO at regular and defect sites of the TiC surface has been studied by means of density functional theory (DFT) based calculations and temperature programmed desorption experiments (TPD) using TiC nanopowders as substrate whose structure and morphology have been characterized by X-ray diffraction and both scanning and transmission electron microscopy. The results obtained confirm previous work indicating that the nature of CO adsorption is strongly dependent on surface coverage due to the distortion of the surface induced by the adsorbate and also allows one to resolve an apparent anomaly between theory and experiment. Calculations and TPD experiments show that CO adsorption strength at regular sites is rather large with an adsorption energy of about −1.60 eV which is consistent with a main desorption peak at ~500 K. Adsorption at low coordinated sites is even stronger and in agreement with desorption experiments indicating that CO continues to desorb at temperatures as high as 600 K.

1. Introduction

The study of the catalytic properties of transition metal carbides (TMC) was triggered by the landmark work of Levy and Boudart [1] who showed that the catalytic properties of this class of materials are similar to those of Pd or Pt in the conversion of n-pentane to isopentane. This stemmed a huge and increasing interest for TMC beyond their already known distinctive features and technologically interesting properties including hardness, [2] high melting point [3] and high electrical and thermal conductivity, which have been investigated both experimentally and theoretically for a long time [1–7]. Nowadays, these properties are usually associated with the different bonding modes that all together contribute to the TMC mixed nature: hard as covalent solids, with the high melting point typical of ionic materials and that show high conductivity like metallic systems. Recent work has demonstrated a non-zero density of states at the Fermi level for various TMCs [6,7].

The recent potential use as catalysts, together with the lower prices compared to noble metals has resulted in a huge number of studies that have explored the catalytic activity of extended surfaces and lower-dimensional structures experimentally [2–4,8–11] and theoretically [3,12,13]. The study of model reactions such as the water gas shift (WGS) reaction, [9,10] CO hydrogenation, [11] or typical "Pt-like" reactions such as α-CH bond activation in 2-butene or cyclohexene dehydrogenation to form benzene, [3] or hydrocarbon hydroisomerisation [14] are only some of the extensive studies performed over the last forty years [2–4]. More recent work demonstrates promising catalytic application of these materials as *non-inert* supports for noble metals nanoparticles [15–24]. All of these studies implied the explicit exploration of the possible adsorption sites with small probe molecules on various surfaces.

Among the different TMC, TiC has often been chosen to study the catalytic properties of the non-polar (001) surface quite extensively [3,25–31]. Note also that TiC(001) is by far the most stable surface and exposes an equal number of Ti and C atoms, allowing Ti–C adsorption sites which, for instance, are commonly preferred by oxygen-containing small organic moieties [29]. Many of the previous works present theoretical and experimental results of the interaction of small probe molecules such as water, ammonia, carbon monoxide, or small alcohols like methanol [23–29], although in some systems the situation is not completely understood; this is precisely the case of CO adsorption as we will illustrate in detail below.

Didziulis et al. [25] presented the first detailed experimental study of this system which was complemented with theoretical results from cluster model calculations. The first data available on the interaction of CO on TiC(001) was obtained by combined experimental techniques including temperature programmed desorption (TPD), high

* Corresponding author.
E-mail address: francesc.illas@ub.edu (F. Illas).

0039-6028/$ – see front matter © 2013 Elsevier B.V. All rights reserved.
http://dx.doi.org/10.1016/j.susc.2013.03.005

resolution electron energy loss spectroscopy (HREELS), X-ray and UV photoelectron spectroscopy (XPS and UPS, respectively). Density functional theory (DFT) based calculations within the B3LYP exchange-correlation potential on a small Ti_5C_5 and Ti_9C_9 cluster model representing the TiC(001) surface were also employed to further interpret the experimental data [25]. The TPD results for CO on TiC(001) showed that CO desorbs at rather low temperatures with a sharp peak at 145 K. Increasing the CO exposure slightly decreased this to 139 K showing that lateral interactions were not significant. From the standard Redhead analysis, the estimated adsorption energy was around −0.5 eV, indicating that the interaction of CO with the TiC(001) surface was weak. HREELS spectra supported this point of view since the change in the CO stretching frequency with respect to the gas phase value was only $-23\ cm^{-1}$, consistent with a small change in the CO bond strength and inferring only a weak interaction with the surface. Interestingly, a peak at $1190\ cm^{-1}$ was also observed which the authors assigned to a different adsorption mode. This peak decreased in intensity with increasing temperature while a peak corresponding to Ti═O vibrations increased in intensity. This is explained by the CO adsorbed on this different site reacting with the surface to form Ti═O species. The XPS and UPS data were unable to assign the adsorption site but the cluster model DFT calculations strongly favoured a model where CO was adsorbed on top of Ti with CO on top of C being unfavoured. The authors interpreted these results as bonding arising only from forward donation of electrons from the CO molecule to the surface with the effective $3d^0$ orbital of Ti not being able to back-donate. These conclusions were supported by further DFT calculations using different codes, which predicted weak adsorption with the site being CO on Ti [27–29].

The above discussion seems to provide a coherent picture of the adsorption of CO on TiC(001). Nevertheless, one must point out that the conclusions extracted from these initial DFT calculations have to be regarded with caution since the cluster model used to represent the TiC(001) surface is extremely small and, more importantly, the geometry of the cluster model and of the CO molecule are fixed and the perpendicular distance from the C atom of CO to either surface C and Ti atoms varied. In fact, subsequent work based on more elaborated density functional calculations and using more realistic surface models which fully take into account surface relaxation resulted in different predictions for the most stable adsorption site. Moreover, depending on the surface model selected, one may find that CO adsorption C-down on top of the metal atom is the preferred binding mode or that the most stable interaction involves C-down on top of the carbon atom [13,25,32–34]. The difference of surface model and, most importantly, the different number of structural degrees of freedom in some of these studies has important consequences in the calculated adsorption energy value. Thus, it goes from nearly −0.5 eV for CO on top of Ti [25,32,33], which is interpreted as arising from the weak interaction of the CO 1π orbital with the empty d-orbital of the formally d^0 metal, to −0.8 eV for CO on top of C[13] at high coverage and, finally, to almost −1.5 eV[34] at very low coverage implying a much stronger, covalent double C–C bond and a concomitant deformation of the underlying substrate. Therefore, one must conclude that the choice of surface model and of surface coverage is more important than earlier anticipated. This is confirmed by the study by Viñes et al. [13] on the mechanism of the WGS reaction over TiC(001), Ti_8C_{12} "metcar" and $Ti_{14}C_{13}$ nanocrystal. These authors found different results for the most favoured CO adsorption site depending on the model. For both bare TiC(001) and $Ti_{14}C_{13}$, which have similar coordination of Ti and C atoms, the most favourable site for CO adsorption was always on a C atom while for the Ti_8C_{12} metcar, the Ti site was preferred.

In a recent study, Asara et al. [34] analysed CO adsorption on TiC(001) in detail as a function of coverage and surprisingly found that this has indeed an unexpected strong effect on the adsorption energy. The study used periodic DFT calculations modelling the slab with supercells of different size and considered different functionals and codes. Again it was shown that a site on a C atom was the most favourable for CO adsorption while the Ti site was stable but lower in adsorption energy. For small unit cells representing a rather large coverage, the energy of adsorption was in line with the experimental one reported in the earlier work of Didziulis [25,26]. However, for larger supercells representing a much lower CO coverage, the adsorption energy calculated converged to around −1.5 eV. These calculations have also shown that upon CO adsorption the TiC(001) surface distorts considerably with the surface C atom which is directly interacting with CO being pulled outwards by 0.5 Å from the equilibrium value for the naked surface. This also explains the results from the high coverage situation where the surface unit cell cannot relax sufficiently to compensate for the surface distortion. The bond distance calculated between the surface carbon atom and the CO carbon was 1.3 Å, a value consistent with expectation for C═C double bonds. This ketenylidene C═C═O surface species has also been calculated as a favourable adsorption site for Mo_2C and indeed there is experimental evidence to support its existence [35,36].

The discussion above demonstrates how complex the interaction of such a simple molecule with titanium carbide is, justifying a further, more rigorous investigation to confirm unambiguously the identity of the adsorption site and the adsorption energy on the clean TiC(001) surface and a rather systematic exploration of the behaviour of the probe molecule in the presence of defects studied using various computational techniques. In this work we present a systematic theoretical study which takes into account adsorption sites located at terrace and step edges and also provide new experimental data that allows one to reach a rather complete picture of the adsorption of CO on TiC.

2. Material models and computational details

The adsorption of CO on the non-polar (001) surface of TiC was modelled using the repeated slab approach, thus using periodic models possessing 4 atomic layers. Supercells of different size were employed to account for coverage effects and further investigate surface relaxation, which was previously found to be crucial [34]. The smallest unit cell corresponds to a $(\sqrt{2} \times \sqrt{2})$/R45° of the primitive one having 2 C and 2 Ti atoms in each atomic layer. For simplicity, this $(\sqrt{2} \times \sqrt{2})$/R45° unit cell will be further referred to as 1 × 1. Following this notation we can describe the larger supercells as 2 × 1, 2 × 2 and 3 × 3 having 32, 64 and 144 atoms, respectively. Fig. 1 displays these slab models including CO at the most stable site in the optimum geometry which is described in the next section. In all cases, slabs repeated in the perpendicular direction to the surface were interleaved by a vacuum width (10 Å) sufficient to prevent interactions between the repeating slabs. A CO molecule was added to these slabs resulting in coverage values of 1/4, 1/8, 1/16 and 1/36 with respect to the total number of exposed surface atoms. The CO molecule was initially added on top of a C surface terrace atom of the TiC(001) surface as this has been shown to be the most stable site [18,36]. Nevertheless, the Ti terrace site of the TiC(001) surface was also investigated using the same 1 × 1, 2 × 1, 2 × 2 and 3 × 3 slab models for comparison. The top two slab layers as well as the CO molecule were allowed to relax during structural optimization and the adsorption energy (E_{ads}) was then calculated as:

$$E_{ads} = E_{slab+CO} - E_{CO} - E_{slab}$$

where E_{ads} is the adsorption energy, $E_{slab\ +\ CO}$ is the energy of the slab with adsorbed CO, E_{CO} is the energy of an isolated CO molecule calculated within the same sized unit cell and E_{slab} is the energy of the clean, optimised surface slab model. For each slab the distortion energy was also calculated, as defined as:

$$E_{dist} = E_{slab-CO} - E_{slab}$$

where E_{dist} is the distortion energy, E_{slab} is the energy of the clean slab and $E_{slab\text{-}CO}$ is the energy of the system at the optimised geometry

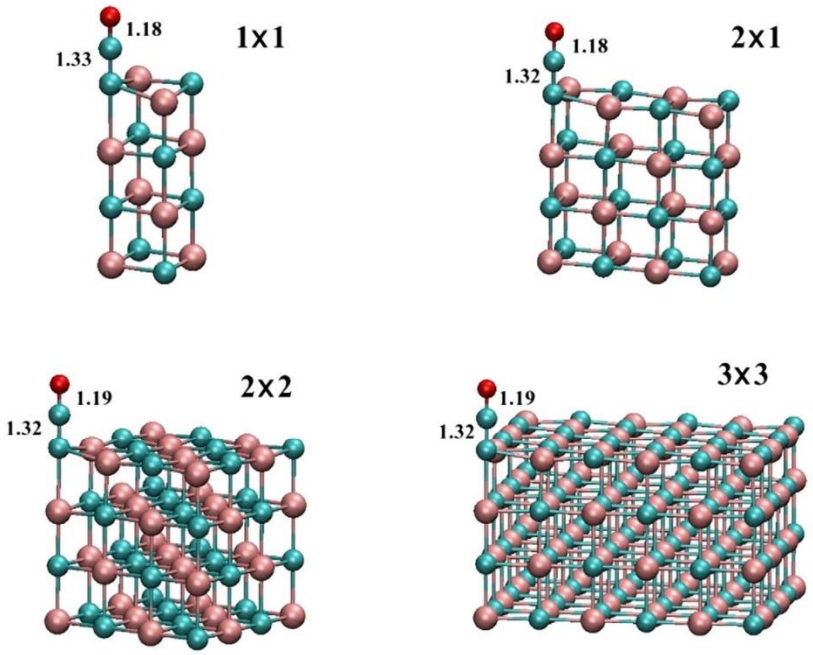

Fig. 1. Schematic representation of the optimised structure of CO chemisorbed on the different supercells used to model TiC(001) and representing surface coverage values of 1/4, 1/8, 1/16 and 1/36, respectively. The C–O and C–C_{surf} distances in Å are also reported.

when CO was adsorbed. This provides an indication of adsorbate induced relaxation which, in turn, is related to bond strength.

In order to investigate adsorption at defect sites, two models have been considered. The first model starts with a 3 × 3 supercell but then half of the surface atoms are removed thus leading to a monoatomic step with Ti and C sites and of the two topmost atomic layers, the two exposed terraces, have been allowed to relax. It is worth noting that monoatomic steps have been detected experimentally on TiC (001) [22]. CO adsorption was studied on carbon (as displayed in Fig.2a) and titanium atoms on the edge site. Kink sites were also modelled by removing either one Ti or one C atom from the step edge (Fig. 2b). The second model corresponds to a 64 atom cluster model with a cubic shape exposing terrace, edge and corner sites. This cube has a side length of 6.1 Å and although it is too small to represent TiC nanoparticles, it is a useful model to study the effect of low coordinated sites on the trends towards CO adsorption. It is worth pointing out that this TiC cubic cluster may constitute an alternative model of the larger cubes observed by scanning electron microscopy (SEM) for TiC nanopowder [37]. During calculations, all atoms in the cube were allowed to relax. In this model system, CO was adsorbed on both Ti and C sites and the most relevant structures are shown in Fig. 3.

The energy for the surface models described above and for CO adsorption on the latter has been obtained from density functional theory (DFT) based calculations using the PW91 form of the generalised gradient approximation (GGA) for the exchange correlation potentials [38,39]. Core electrons were treated using the projected augmented wave (PAW) method of Blöch [40,41] and as implemented by Kresse and Joubert [42]. This procedure keeps the accuracy of an all electron calculation with the computational efficiency of pseudopotentials. The electron density was approximated using a plane wave basis set with a kinetic energy cut-off of 415 eV. This has already been demonstrated to be sufficient for this system [6,34]. Numerical integration in reciprocal space was carried out using a Monkhorst–Pack grid [43] of 10 × 10 × 1 *k*-points for every supercell model. For the model with steps, a *k*-point mesh of 10 × 10 × 1 was also used with a vacuum width of 10 Å between images whereas calculations for the nanocube model were carried out at the gamma point. All structures were optimised thereby ensuring that forces on all relaxed atoms were smaller than 10^{-3} eV/Å and the resulting optimised geometries were characterized as minima on the potential energy surface calculating the associated normal modes by explicit diagonalization of the corresponding block of the Hessian matrix which, as usual, is obtained from finite difference of analytic gradients.

Using the computational setup described above, the TiC calculated equilibrium cell parameter and bulk modulus were 4.336 Å and 266 GPa, respectively, both close to the experimental values (4.328 Å and 233 GPa) [34] thus ensuring sufficient accuracy for the present purposes. All DFT calculations were carried out by using the VASP code [44,45].

Finally, in order to better interpret some of the results which will be presented in the forthcoming sections, a series of kinetic Monte Carlo simulations of the desorption process have been carried out which required implementing and testing the algorithm proposed by Meng and Weinberg [46].

3. Experimental details

Growing TiC single crystals is far from being a simple task and this may be considered as the main reason for the rather limited literature on adsorption on specific well defined surfaces of this material. In general, the synthesis of TiC single crystals and of other transition metal carbides may be accomplished through the Verneuil technique,

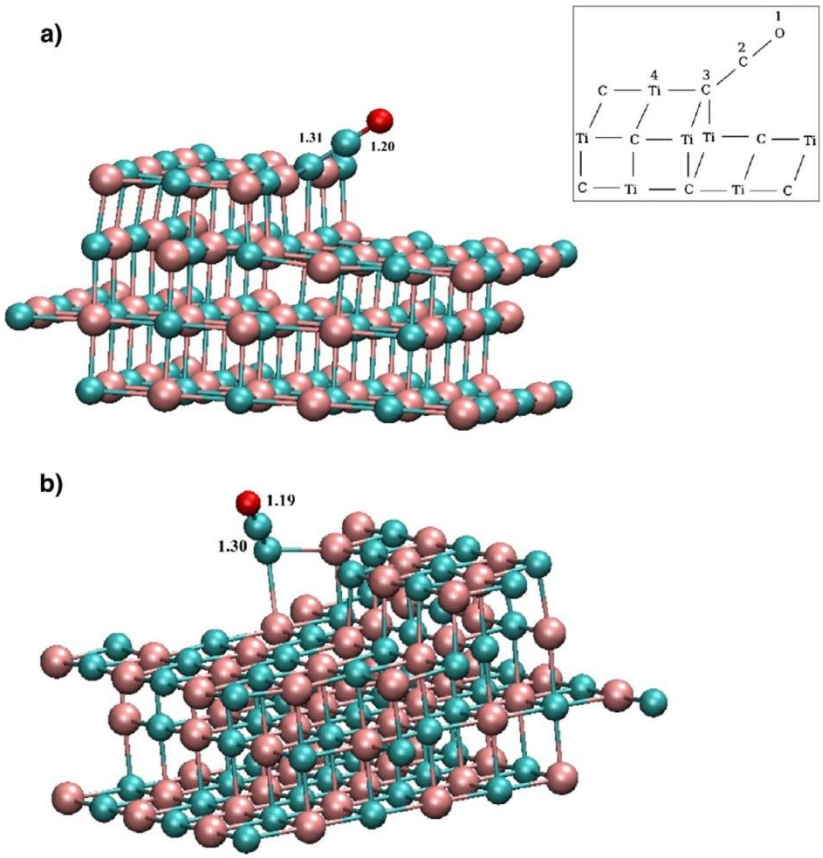

Fig. 2. Schematic representation of the optimised structure of CO chemisorbed at the step edge (a) and kink (b) slab models. Note that the final structure for CO at the kink site also involves a C atom at the step edge. The C–O and C–C_{surf} distances in Å are also reported. The inset in the top right defines the relevant bond and dihedral angles.

[47,48] the "floating zone" method [49–51] and, in particular, the improved technique by Otani et al., [53] precipitation from molten metals, [54] and chemical vapor deposition [55–58]. Unfortunately, all of these techniques involve very high temperatures, which are needed to melt and recrystallize the metal carbides, and also involve the manipulation of volatile and highly reactive reagents. Recently, a technique to obtain TiC single crystals using a lower temperature preparation in molten salts has been proposed [59] although this still requires temperatures of ~1200 K and leads only to nanofibers and not to more extended nanocrystals with well-defined surfaces. Therefore, it was decided to carry out experiments using commercial TiC powder (nanopowder, Sigma Aldrich, 95%, <200 nm). Although experiments on nanopowder cannot be compared directly to our calculations on the TiC(001) crystal face, it is important that this surface is by far the most stable one and, hence, expected to be the most abundant in the powder. The choice for TiC nanopowder is justified also by the extensive work on MgO where it has been shown that single crystals, thin films supported on metals and nanopowders in the form of MgO smokes, exhibit a behaviour which is closer than anticipated. In fact, there is compelling evidence that varying the surface area of the substrate barely affects local properties such as adsorption energies and vibrational frequencies, the case of CO adsorption on MgO being a clear paradigm [60]. Therefore, it is expected that the experiments on the TiC powder should provide a useful guide for comparison between our new results and past work, especially as there is only one previous experimental study [25].

The characterisation of TiC nanopowder was accomplished using different techniques. The X-ray powder diffraction (XRD) pattern was obtained with a Panalytical X'Pert PRO MPD α1 (r = 240 mm) diffractometer using Cu-Kα radiation (λ = 1.5406 Å). The analysis was carried out with X'Pert High Score Plus and WinPlotr software. Scanning electron microscopy (SEM) micrographs were obtained using a ZEISS Auriga instrument equipped with an Oxford energy dispersive X-ray (EDX) analyzer. Transmission electron microscopy (TEM) analysis was carried out with a Jeol 2000 instrument. X-ray photoelectron spectra (XPS) of as received TiC sample was acquired with a PHI 5500 Multitechnique System instrument (Physical Electronics) with a monochromatic X-ray source (Al Kα line of 1486.6 eV), placed perpendicular to the analyzer axis and calibrated using the 3d5/2 line of Ag. During data acquisition the pressure was kept at 4×10^{-9} mbar. The Ti 2p, C 1s and Cl 2p atomic levels were analysed. The analysis and fitting of the spectra were made with Multipak V8.2B program from ULVAC-PHI. The presence of chlorine as impurity was detected (atomic surface concentration below 1%). Temperature programmed desorption (TPD) of CO was carried out on TiC nanopowder using a Micrometrics Autochem II 2920 instrument equipped with a thermal conductivity detector (TCD).

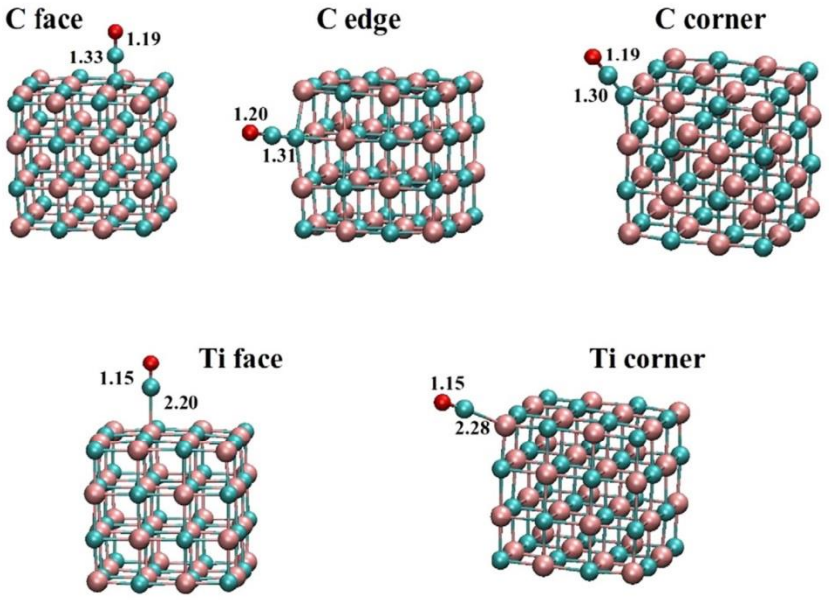

Fig. 3. Schematic representation of the optimised structure of CO chemisorbed on the different sites of the 64 cluster atoms model representing a TiC nanoparticle. The C–O, C–C_{surf} and C–Ti distances in Å are also reported.

The sample (around 0.05 g) was placed into a U-shaped reactor for analysis. The sample was pretreated in a He flow at 363 K for 15 min, and then the temperature was decreased at 298 K and the sample exposed to a CO flow (10% v/v CO in He, 10 mL/min). After baseline stabilisation, the temperature was increased at 10 K/min up to 973 K and measurements recorded every 0.1 s.

4. Results and discussion

4.1. Density functional theory based calculations

In order to compare different situations involving different coverage and different types of adsorption sites, it was convenient to re-examine previous work concerning CO adsorption at the terrace sites of TiC(001) [34] using more stringent convergence thresholds for energy and geometry optimization. Hence, the adsorption of CO on the TiC(001) surface was first studied using the smaller 1×1 supercell and considering both C and Ti sites. The corresponding density functional calculations predict that the C-down adsorption mode with the C–O axis perpendicular to the surface plane is the most favoured and, at the same time, confirm previous results on the preferred adsorption mode above the C surface site with an adsorption energy of −0.83 eV [34]. The interaction energy calculated for the adsorption on the Ti site is somewhat smaller (−0.61 eV) and also in agreement with previous theoretical results obtained by density functional calculation on a rather small surface cluster model. The latter was indeed claimed to be in agreement with available experimental results [25]. An important structural feature of the chemisorption bond between CO and the C atom of the TiC(001) surface (hereafter referred to as C_{surf}) is the C–C_{surf} distance of 1.33 Å which is reminiscent of a C=C double bond. This strong interaction weakens the C–O bond as indicated from the calculated bond length, that passes from 1.14 Å of the gas phase molecule to 1.18 Å upon adsorption on TiC(001). The strong C–C_{surf} interaction also causes a significant distortion of the surface, pulling the surface carbon atom by 0.31 Å into the vacuum which contrasts with the smaller outward distortion of the surface when CO interacts directly above a surface Ti atoms with a rather long C–Ti distance (2.19 Å) and with a small change in the C–O bond distance, calculated as 1.15 Å. The results regarding equilibrium geometry of adsorbed CO above C and Ti sites together with the adsorption energy values reported above clearly point to C_{surf} as the preferred adsorption site. Also, taking into account the well-known tendency of the GGA functionals to exaggerate adsorption energies [61], our rather high coverage (1/4 of the exposed surface atoms are covered) results for adsorption on both metal and carbon sites seem to agree perfectly with the experimental value that can be extracted from the TPD experiments of Didziulis et al. [25]. Nevertheless, the discussion in Section 1 already indicated that the situation is more complex than initially envisaged.

Let us now move from the 1×1 to the 2×1 surface model adsorbing CO on one of the four distinct exposed surface carbon atoms, which implies further reduction of the CO coverage from 0.25 to 0.125. This reduction in coverage produces an increase in the calculated CO adsorption energy at the C site, which becomes −1.21 eV, a surprising result which was also reported in previous work [34], but it barely affects the CO adsorption energy at the Ti site which only changes by 0.01 eV. In both cases, the geometry of the adsorbed CO molecule does not change from that predicted by the previous set of calculations modelling a CO coverage of 0.25. For the C site, the C–O and C–C_{surf} distances are 1.18 Å and 1.32 Å, respectively, almost identical to the values reported above for higher coverage. A similar situation is found when considering the Ti site (Table 1). The reason for the larger adsorption energy at the C site has been attributed to a more efficient manner of relaxing the surface distortion produced by CO adsorption due to the higher number of degrees of freedom available [34]. This produces a smaller distortion with a decrease of the distance from the titanium of the second layer to C_{surf}: of 2.45 Å instead of 2.53 Å as corresponding to the situation modelled by the 1×1 supercell. Thus, the larger 2×1 supercell can relax more, and better describes the distortion due

Table 1
Adsorption (E_{ads}) and distortion (E_{dist}) energies calculated for CO adsorbed on C and Ti sites of TiC(001) surface models. $E_{dist\text{-}norm}$ corresponds to normalising E_{dis} with respect to the number of 1 × 1 units in the supercell. All values are in eV.

Slab	Site	E_{ads}	E_{dist}	$E_{dist\text{-}norm}$/eV
1 × 1	C	−0.83	0.33	0.33
	Ti	−0.61	0.03	0.03
2 × 1	C	−1.21	0.37	0.19
	Ti	−0.62		–
2 × 2	C	−1.56	0.55	0.14
	Ti	−0.63		–
3 × 3	C	−1.58	0.64	0.07
	Ti	−0.63		–

to the adsorption of CO. For this reason, distortion energies (normalised with respect to the number of atoms in the 1 × 1 supercell contained in the model) calculated for both 1 × 1 and 2 × 1 systems are 0.33 and 0.19 eV, respectively. Interestingly, adsorption at the Ti site does not produce this surface deformation and, hence, the corresponding adsorption energy does not vary substantially with coverage.

Further decreasing the coverage to 0.0625, which corresponds to a single CO molecule per 16 surface atoms in the 2 × 2 supercell, and to 0.027 (one CO molecule per 36 surface atoms using a 3 × 3 supercell) produces a significant increase in the adsorption energy from −1.21 eV for the coverage represented by the 2 × 1 supercell to −1.56 and −1.58 eV for the situations corresponding to the 2 × 2 and 3 × 3 unit cells, respectively. In these latter cases, the atomic structure of the adsorbate remains almost unchanged when compared to the 2 × 1 model. A decrease in the Ti – C_{surf} distance can be seen with respect to the value corresponding to the 1 × 1 model, which becomes 2.49 Å for the 2 × 2 supercell and 2.46 Å in the case of the 3 × 3. For these models, the calculated normalised distortion energy decreases to 0.14 and 0.07 eV, respectively, demonstrating that the situation with very low CO coverage permits an improved manner of relaxing the structural distortion caused by CO adsorption. Tables 1 and 2 summarize the calculated values for adsorption and distortion energies as well as the corresponding structural parameters.

To further investigate the effect of CO coverage, vibrational frequencies for the normal modes related to adsorbed CO were calculated for the different situations represented by each of the supercells considered. It is worth pointing out that the analysis of adsorption modes based on CO stretching frequency have been proven to lead to erroneous interpretations in other cases [62], and that even the interpretation of the vibrational shift of the internal CO mode is far from being straightforward [63,64]. Here, we use this property to provide further insights on the nature of the CO/TiC interaction and to compare with available experimental data. The results of the different sets of frequency calculations are reported in Table 3. For the interaction of CO with the C_{surf} site, the present density functional calculations predicts a decrease of 36 cm^{-1} in the C – O stretching frequency when moving from a coverage of 0.25 as represented by the 1 × 1 structure to that represented by the 2 × 2 surface model, and then converging to a value of 2025 cm^{-1} calculated for the 3 × 3 supercell. This normal mode is

Table 2
Bond lengths (Å) calculated for CO adsorbed on TiC(001): $d_{C\text{-}O}$ refers to the distance between the C and the O atom of the adsorbate; $d_{\perp}$ is the distance between the C atom of adsorbed CO and the surface atom (C or Ti) below it; d_{12} corresponds to the distance between the surface atom below the CO molecule and the one in the second layer; $d_{12\text{–}naked}$ is as d_{12} but for the naked surface.

Slab	Site	$d_{C\text{-}O}$	$d_{\perp}$	d_{12} (d_{12_naked})
1 × 1	C	1.18	1.33	2.53 (2.22)
1 × 1	Ti	1.15	2.19	2.16 (2.09)
2 × 1	C	1.18	1.32	2.45 (2.22)
2 × 2	C	1.19	1.32	2.49 (2.17)
3 × 3	C	1.19	1.32	2.46 (2.22)

Table 3
Calculated vibrational frequencies (cm^{-1}) for the stretching (ν_{CO}) and frustrated translation ($\nu_{\perp}$) modes of the adsorbed CO molecule. The calculated ν_{CO} value for gas phase CO is 2131 ± 1 cm^{-1} where the error bar originates from the use of the different supercells for the calculation of the isolated molecule.

Slab	1 × 1	2 × 1	2 × 2	3 × 3
ν_{CO}	2069 (C site) 2061 (Ti site)	2050	2033	2025
$\nu_{\perp}$	1118 (C site) 379 (Ti site)	1154	1177	1174

clearly coupled to the C_{surf}–C stretch. The latter mode increases from 1118 cm^{-1} calculated in the 1 × 1 to 1177 cm^{-1} in the 2 × 2, leading to an almost (within numerical accuracy) converged value of 1174 cm^{-1} for the 3 × 3 supercell representing a low coverage situation. Accordingly, one can tentatively relate this low coverage C_{surf}–C stretching vibrational frequency to the feature found experimentally by Didziulis et al. [25] at 1190 cm^{-1} and not previously assigned.

It is important to stress that all results discussed so far are in perfect agreement with the previous picture outlined in the work of Asara et al. [34], even if the previously reported adsorption energies were somewhat smaller and the trends discussed above in both bond distances and vibrational frequencies were not clearly identified due to the rather flat potential energy surface which requires much more stringent convergence criteria to obtain a definitive answer. Consequently, the present numerically more accurate study avoids ambiguities and provides a solid background for the next step which is the study of role of the various defects on the (001) surface by means of slab and nanocube models (Figs. 2a, b, 3).

The adsorption of CO on a low coordinated C site was modelled first using a slab model built in such a way that it enables one to explore one-atom-step and kink defects. The first type of defect is modelled by removing some atoms in the first layer of the TiC(001) slab, as indicated in the previous section, and the latter obtained by subtracting a titanium or carbon atom, respectively from the step. On both models the high accuracy of the calculations together with the extremely tight criterion for the geometry optimization, already tested for adsorption of diatomic molecules on other stepped surfaces [65], allowed us to locate a proper minimum energy structure in such a complex system which was further characterized by frequency analysis. The present calculations predict large values of the adsorption energy on both defects: −2.87 eV for the molecule adsorbed at the step site and −3.45 eV on the kink site which indicate that this would lead to an irreversible adsorption. As a result of this strong interaction, there is an even larger distortion of the substrate compared to the case of the C terrace site with concomitant calculated distortion energy values of 0.63 eV for the step and 0.47 eV for the kink site. In the step model, such strong adsorption causes the C – O bond length of the adsorbate to reach 19 Å with a further decreased C_{step}–CO distance of 1.31 Å. The CO axis does not remain perpendicular to the surface, but instead tilts towards the bottom of the atomic step and forms an angle of 152° with the upper terrace. On an even lower-coordinated carbon atom, as in the kink model, the calculations starting with CO adsorbed on a edge carbon and tilted to the bottom of the step, as in the case of the step site, converged to a different situation with the CO axis leaning towards the vacancy left by the titanium atom and no stable adsorption modes involving other carbon atoms of the kink were found. Structural parameters for this optimised geometry agree well with those of the edge site modelled with the step, and with what was previously discussed for adsorption on the terrace, showing a C – O distance of 1.19 Å and a distance between the carbon of the edge and the carbon of the adsorbate of 1.30 Å. Results are summarized in Table 4.

To further explore the effect of relaxation of the underlying substrate on the adsorption on low coordinated carbon and titanium atoms, a relatively small stoichiometric nanocube consisting of 64 atoms was constructed and its atomic structure optimised. This

Table 4
Adsorption (E_{ads}) and distortion (E_{dist}) energy values and structural parameters calculated for CO interacting with Ti and C atoms of step and at kink sites, respectively. The latter is obtained by subtracting either a C (adsorption on Ti) or a Ti atom (adsorption on C) from the step model. $d_{C\text{-}O}$ refers to the distance between the C and the O atom of the adsorbate and $d_{\perp}$ is the distance between the C atom of adsorbed CO and the underlying closest surface atom. The α and β bond and dihedral angles are as defined in the inset of Fig. 2; the former represent the angle between atoms labelled 2, 3 and 4 and the latter the dihedral angle between the atoms labelled as 1, 2, 3 and 4. Distances are in Å, angles in degrees and energy values in eV.

	Site	E_{ads}	E_{dist}	$d_{C\text{-}O}$	$d_{\perp}$	α (°)	β(°)
Step	**C**	−2.87	0.63	1.19	1.31	152	145
	Ti	−0.84	0.01	1.15	2.20	139	146
Kink	**C**	−3.45	0.47	1.19	1.30	120	66
	Ti	−2.30	0.30	1.28	2.21	94	47

nanostructure contains adsorption on various possible low coordinated sites already considered using the slab model but it also permits one to explore additional adsorption sites. It is worth noting that a TiC cubic nanostructure has been hypothesized [66], theoretically confirmed [67] and also experimentally seen in the present electron microscopy (SEM and TEM) study for experiments on TiC nanopowder (see Section 4.2). On the nanocube model we obtained results that are in qualitative agreement with the predictions from the slab models for both the clean and stepped surface. Here, in addition to terrace sites at the nanocluster faces, adsorption on both edge and corner C and Ti sites was also explored. Face sites give results comparable to the values obtained for the 1 × 1 supercells. Adsorption at the C site gives the most stable structure, with a calculated adsorption energy of −0.65 eV, and a distortion energy of 0.49 eV, whereas adsorption above Ti site leads to a somewhat less stable structure with an adsorption energy of −0.60 eV. In this case, the distortion energy with respect to the relaxed nanocube was only 0.05 eV indicating that adsorption at the Ti site is less sensitive to CO coverage. This is not surprising since the TiC nanocluster does not have the structural rigidity imposed by the crystal lattice. The present calculations also show that CO adsorbs very strongly at C edge and corner sites with energies of −2.1 and −3.1 eV, respectively. This is close to the energies of step and kink sites modelled using the slab model, indicating that the nanocube represents a good approach for modelling of defect sites. For CO adsorbed at the Ti corner, the calculated adsorption energy was −0.76 eV, not very different from the value predicted using the 1 × 1 supercell slab model or the face site of the TiC nanocube. Thus, even on low coordinated metal sites, the binding is still relatively weak. This is highlighted by the results corresponding to the CO molecule adsorbed at the Ti edge site, which is found to be unstable.

Finally, a comment should be made on the vibrational frequencies corresponding to CO adsorption at the nanocube. Going from CO at the C adsorption site at the cube face to the corner C site, the CO stretching frequency shows an increase of *ca.* 60 cm^{-1}. This shows that the dependence of the C–O stretching frequency does not provide a way to identify adsorption sites. This conclusion is consistent with the results corresponding to CO adsorption at the corner Ti and face Ti sites, which displays only a small variation in the stretching frequency. Adsorption energies and vibrational frequencies calculated for the nanocube model are reported in Tables 5 and 6.

Table 5
Adsorption (E_{ads}) and distortion (E_{dist}) energies (eV) for CO adsorption at different sites on the TiC nanocube model. Adsorption on edge titanium atom was found to be unstable.

Site	E_{ads}	E_{dist}
C_{face}	−0.65	0.49
Ti_{face}	−0.60	0.05
C_{edge}	−2.10	0.93
C_{corner}	−3.10	0.90
Ti_{corner}	−0.76	0.02

Table 6
Calculated vibrational frequencies (in cm^{-1}) for the stretching (ν_{CO}) and frustrated translation ($\nu_{\perp}$) of the adsorbed CO molecule on different nanocube sites.

Site	C face	Ti face	C corner	C edge	Ti corner
ν_{CO}	2000	2034	2059	2021	2043
$\nu_{\perp}$	1117	371	1265	1214	403

4.2. Experimental results

The system resulting from the interaction of CO with the TiC nanopowder and the TiC substrate itself was studied with an array of different experimental techniques which are useful in analysing the sample and to provide insight into the nature of adsorption and desorption processes. Firstly, powder XRD analysis was performed on the TiC nanopowder (Fig. 4). As expected, only diffraction peaks corresponding to cubic (F3-3 m) TiC are present. The crystallite size can be estimated using the Scherrer equation [68]:

$$d = \frac{k\lambda}{B\cos\theta}$$

where d is the crystallite size, k is a shape factor taken to be 0.94 for cubic particles, λ is the wavelength of X-rays, θ is the angle of peak and B is the line broadening of the peak at half maximum (FWHM). From the most intense (200) peak, a value of around 27 nm as the average crystallite size of the TiC nanopowder was obtained. SEM was used to analyse the morphology of the TiC nanocrystals. Examples of images obtained are shown in Fig. 5. A homogeneous distribution of cubic particles mainly ranging in size between 10 and 50 nm can be seen. Moreover, TEM analysis of individual nanoparticles allowed us to confirm their nature and to carry out microstructural characterisation; measured interplanar distances were consistent with cubic TiC crystallites. Fig. 6 shows the TEM micrograph obtained for a TiC particle of *ca.* 10 nm of size and its Fourier transform indexation (see inset of Fig. 6). In the TEM image, spacings corresponding to the (200) plane of TiC are visible and the Fourier transformed image of this crystallite contains spots corresponding to the (200) and (110) Miller indices of cubic TiC. These findings indicate that the theoretical study based on the nanocube-like models used in this work can be related with the experimental results of CO adsorption onto nanopowder TiC sample.

CO was dosed onto the TiC nanopowder and the resulting system studied by means of temperature programmed desorption (TPD). Results for the analysis of CO thermodesorption profile are reported in Fig. 7. Desorption temperatures above 500 K, which are higher than those reported in previous single crystal studies [25], are observed.

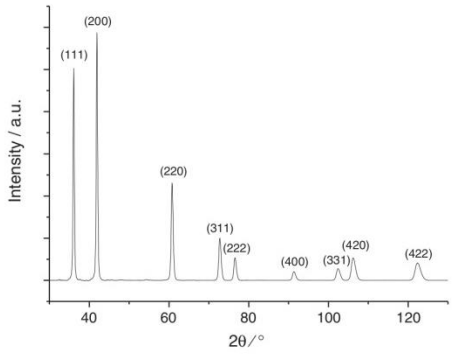

Fig. 4. X ray diffraction (XRD) pattern of the sample of TiC nanopowder (ICSD 03-065-0971).

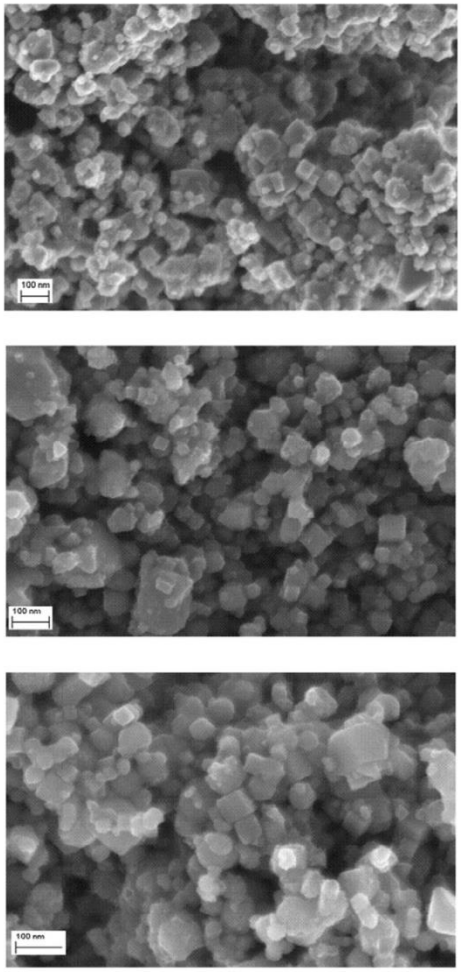

Fig. 5. Scanning electron microscopy (SEM) images of TiC nanopowder.

The present TPD results show that at least for some sites/faces of the TiC nanopowder strong adsorption of CO exists which, is in line with results from DFT based calculations for TiC(001) slab models. Note, that, as mentioned above, this surface should predominate in the nanopowder. The high dependence of the adsorption energy with coverage can be employed to explain the differences with previous data that reported an adsorption energy of around −0.76 eV [13], which is close to the high coverage value reported in this work. In our experiment, the adsorption of CO was carried out at 298 K (e.g. above the 150 K reported in previous work). Here, the temperature employed for initial CO exposure is too high to allow a high coverage situation and leads to only a fraction of the surface being covered by CO molecules. A consequence of this lower coverage is that molecules adsorb more strongly and remain so until above 500 K. This data is fully consistent with the computational results presented above which predict an adsorption energy of around −1.5 eV for low coverage of the (001) surface and much higher for defect sites accounting for the additional peak observed around 600 K.

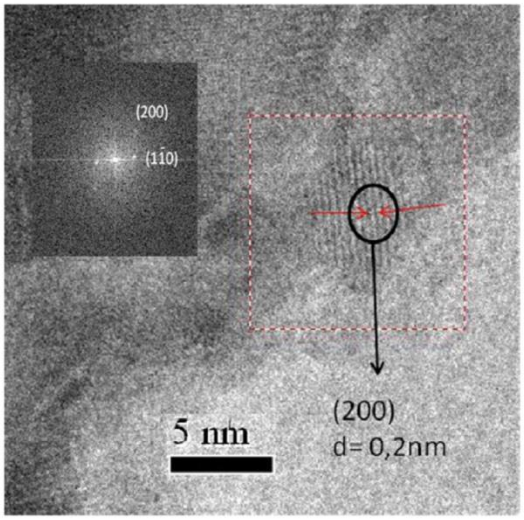

Fig. 6. TEM micrograph of an individual TiC particle. The inset corresponds to the Fourier transform analysis. The interplanar distance corresponds to the indexed (200) plane.

4.3. Kinetic Monte Carlo simulation of TPD experiments

The main goal of the present kinetic Monte Carlo (kMC) TPD simulations is to further confirm the interpretation above regarding the coexistence of a low and a high temperature peaks caused by the strong dependence of the adsorption energy on the CO coverage of the (001) surface. The simulation of desorption for various initial coverage values demonstrated how the low temperature desorption peak is present only at sufficiently high initial coverage whereas the high temperature peak is always present. This second peak at higher temperature is produced by the few desorbing molecules that still populate the surface at such high temperature. Present simulations consider only adsorption on top of surface carbons, as justified by DFT results, and results already reported [34] for the adsorption energy values in the various supercell models as starting parameters for the TPD simulations. For each CO molecule explicitly included in the simulation box, the adsorption energy was calculated by considering the effect of the number of possible first, second and third neighbour sites occupied. The DFT results presented above have already shown that surface relaxation induced by the adsorbed CO molecule constitutes the major contribution to the dependence of adsorption energy with coverage. Consequently, the effect of lateral CO–CO interaction was

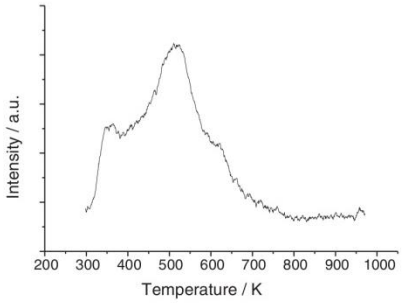

Fig. 7. Temperature programmed desorption (TPD) profile of adsorbed CO on TiC nanopowder.

not considered. The adsorption energy of a molecule i surrounded by n_1 (first), n_2 (second) and n_3 (third) neighbouring molecules, can then be approximated as:

$$E_{ads}(i) = E_0 + \tfrac{1}{4}(n_1)(E_1 - E_0) + \tfrac{1}{4}(n_2)(E_2 - E_0) + \tfrac{1}{4}(n_3)(E_3 - E_0)$$

where the $(E_1 - E_0)$, $(E_2 - E_0)$ and $(E_3 - E_0)$ quantities refer to the difference between the low coverage adsorption energy of a molecule, E_0, and a molecule whose four first (E_1), second (E_2) or third (E_3) neighbour sites are occupied, respectively, and with the different energies obtained from suitable supercell calculations representing the different coverage situations. In this way, the model takes into account the effect that neighbouring molecules have in varying the adsorption energy of the molecule considered. Desorption rates are then calculated from Arrhenius type plots assuming a constant pre-exponential factor of 10^{13}. Simulations for different initial coverages have been carried out on a 50 × 50 lattice, using periodic boundary conditions and a constant heating ramp of 4.8 K/min. From the simplicity of the model, a perfect agreement between theory and experiment cannot be expected. Nevertheless, it contains the essential ingredients to nicely reproduce the main trends observed.

The results obtained from the kMC simulations are reported in Fig. 8. The top of the figure shows the TPD profile (left) obtained for various initial coverages and contains a graphical representation of neighbour sites around each molecule adsorbed on the lattice (right). The bottom of the figure presents the simulated low (right) and high (left) coverage TPD profiles and shows peaks reproduced populating different fractions of the totality of the lattice sites. The overall simulated TPD profile for initial coverage above 50% predicts an intense desorption peak at temperatures around 150 K with a small shift toward lower temperatures when increasing the initial coverage. This is in good agreement with the experimental observations of Didziulis et al. [25] where initial conditions for the adsorption of the gas at very low temperature led to high initial coverage. Upon desorption of some of the molecules, the fraction of the occupied sites on the lattice lowers and the molecules now left on the surface can adopt regular configurations that reduce the distortion obtaining a higher average adsorption energy and a decrease of the calculated total desorption rate. Note that a small desorption peak at about 300–350 K, which is also seen in our TPD experiment (Fig. 7) is also present. This can be associated with an intermediate coverage situation that still does not allow molecules to stay far enough from each other so as to completely relieve the large surface distortion. The desorption feature observed at 450–500 K in the last part of the thermodesorption profile (Fig. 8 top left) is due to the small amount of molecules still adsorbed on the surface. Desorption at temperatures lower than 250 K involves an initial situation where at least half of the lattice sites are occupied. This is clearly shown in the profiles reported in Fig. 8 — bottom left, showing desorption peaks around 200 K obtained for initial coverages of 50 and 55%. The high temperature peak can be also reproduced simulating an initial very low coverage compatible with a much higher adsorption temperature. Such small amount of molecules adsorbed can initially stay far enough from each other so as to lead to high adsorption energy while minimizing the

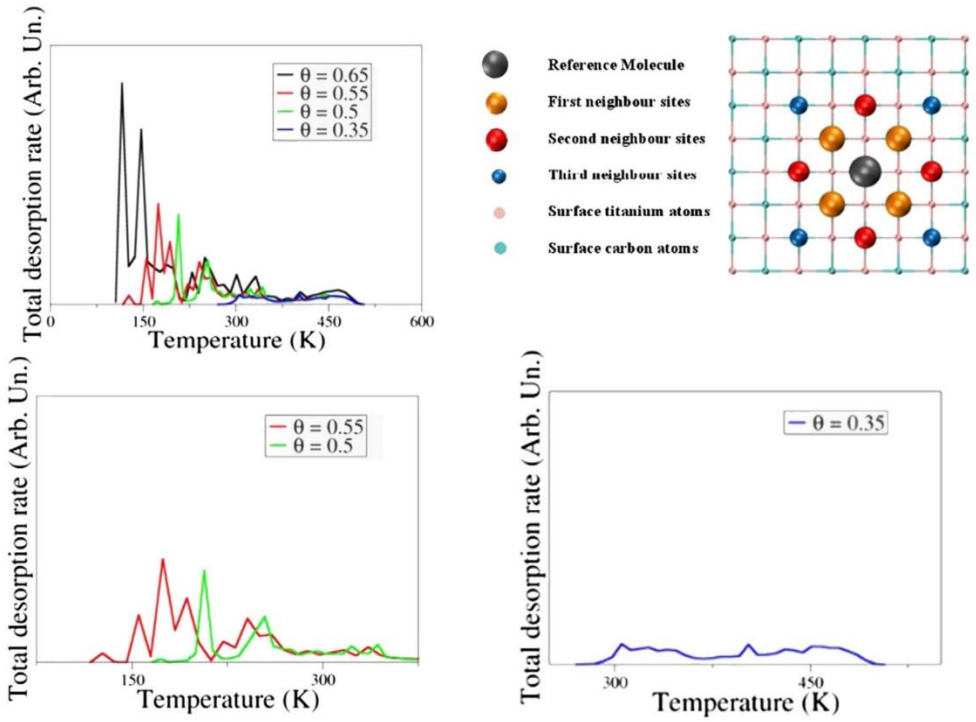

Fig. 8. Temperature programmed desorption profiles simulated for different initial coverages (top left) with neighbour sites distribution around a reference molecule (top right). The intense low temperature peak is reproduced only for initial situations with coverage higher or equal to 0.5 (bottom left). The high temperature peak in the last part of the spectra can be reproduced assuming very low initial coverage (bottom-right).

surface distortion. However the amount of molecules desorbing at this temperature is too small and will produce a weak signal only, hardly seen if directly compared with the low temperature peak. As reported in Fig. 8 — bottom right, kMC simulations for higher temperature adsorption, that is, initial coverages much lower than 50%, led to the appearance of the high temperature desorption peak alone and causing the absence of the low temperature peak. This agrees well with results obtained for desorption experiments after higher temperature CO adsorption on TiC nanopowder. Note that the reliability of the simulations is ensured by the overlap of the high temperature peaks obtained for every initial coverage. Finally, simulated thermodesorption profiles agree well with the experimental desorption features at both high (above 500 K) and low (about 150 K) temperatures.

To summarize, the kMC simulations carried out with energies obtained from periodic DFT calculations show both high and low temperature desorption peaks associated with very low and very high coverages which are in agreement with present experiments on TiC nanopowders and also with previous ones carried out on single crystal although the latter were unable to detect the high temperature peak.

5. Summary and conclusions

The interaction of CO with TiC has been studied using density functional theory based calculations on periodic and nanoparticle models and a variety of experimental techniques using TiC nanocrystals as substrate. This choice is justified by the almost insurmountable difficulty in preparing TiC single crystals [47–58] and also by experiments on MgO smokes showing that local properties such as vibrational features are comparable to those obtained in single crystals or thin films deposited on metal substrates and under ultra high vacuum conditions [60].

The DFT based calculations show that, on the TiC(001) surface, the preferred adsorption site is a C atom with the CO molecule adsorbed with the C end down. The present work confirms that adsorption energy highly depends on coverage [34]. At a relatively high coverage of 1/4 of the exposed surface atoms, a low adsorption energy of −0.83 eV is calculated with a concomitant large distortion energy due to the deformation of the surface induced by the presence of CO, while at a lower coverage of 1/36 of the surface atoms, the adsorption energy increases (in absolute value) to around −1.60 eV with a lower distortion energy. The large difference is due to the fact that, upon adsorption, the CO molecule pulls the surface C atom out of the surface to form a rather short, strong C_{surf}–C bond, explaining the large distortion energy. This also explains why larger supercells corresponding to lower coverage can better spread out the effect of this distortion leading to a lower distortion energy and thus a higher adsorption energy. The coverage dependent adsorption energy also helps to shed light on the differences encountered with a previous published experimental work [24], which reported a low temperature desorption of CO at 150 K corresponding to an adsorption energy of about −0.5 eV while recent computational work predicted a much stronger adsorption energy [34]. CO exposure at very low temperatures encourages high coverage, causing a decrease in the adsorption energy and a weak interaction with the substrate. Adsorption at higher temperatures results in lower coverage, with a much stronger interaction between the few remaining CO molecules and the substrate. TPD experiments found desorption of CO from TiC nanopowder at over 500 K supporting the interpretation above and the view of this low coverage-high adsorption energy situation. This picture is also supported from the kinetic Monte Carlo simulations although one may argue that the results are triggered by the input energies. Nevertheless, the simulations are consistent with the measured TPD.

To investigate CO adsorption at low coordinated sites, slab models with both step and kink sites were built and a 64 atoms cube was also used to model TiC cubic nanocrystal inferred from XRD and electron microscopy analysis. The DFT based calculations show that adsorption at these defect sites is even stronger. For the step site the calculated adsorption energy is −2.87 eV while for the kink site this increases to −3.45 eV. The present TPD results also evidenced such strongly bound molecules, with CO desorption occurring around 600 K. Energy values for CO adsorption on various sites on the nanocrystal model are in good agreement with those obtained by adsorbing CO on single crystal and defect slab models.

Acknowledgements

The authors are indebted to Prof. Piefranco Demontis, Dr. Federico G. Pazzona and M.Sc. Andrea Gabrieli of the Università degli Studi di Sassari for the fruitful discussions on the kinetic Monte Carlo methods. BM thanks the Erasmus programme for financing his stay at the Universitat de Barcelona, GGA thanks *Universitat Rovira i Virgili* for supporting his pre-doctoral research and FI acknowledges support received through the "*2009 ICREA Academia*" prize for excellence in research. Financial support has been provided by the Spanish MICINN/MINECO (grants FIS2008-02238, CTQ2008-06549-C02-01, Consolider Ingenio2010, Multicat CSD2009-00050 and MAT2011-23775) and in part by *Generalitat de Catalunya* (grants 2009SGR1041, 2009SGR00462, 2009SGR-0674 and XRQTC). Calculations were carried out, in part, at the CESCA and BCS supercomputer centres.

Appendix A. Supplementary data

Supplementary data to this article can be found online at http://dx.doi.org/10.1016/j.susc.2013.03.005.

References

[1] R.B. Levy, M. Boudart, Science 181 (1973) 547.
[2] S.T. Oyama, Catal. Today 15 (1992) 179.
[3] H.H. Hwu, J.G. Chen, Chem. Rev. 105 (2005) 185.
[4] A.M. Alexander, J.S.J. Hargreaves, Chem. Soc. Rev. 39 (2010) 4388.
[5] L.E. Hollander, J. Appl. Phys. 32 (1961) 996.
[6] F. Viñes, C. Sousa, P. Liu, J.A. Rodriguez, F. Illas, J. Chem. Phys. 122 (2005) 174709.
[7] P. Soni, G. Pagare, S.P. Sanyal, M. Rajagopalan, J. Phys. Chem. Solids 73 (2012) 873.
[8] J.G. Chen, B. Fruhberger, J.J. Eng, B.E. Bent, J. Mol. Catal. A 131 (1998) 285.
[9] J. Patt, D. Ju, C. Phillips, L. Thompson, Catal. Lett. 65 (2000) 193.
[10] D.J. Moon, J.W. Ryu, Catal. Lett. 92 (2004) 2.
[11] I. Kojima, E. Miyazaki, J. Catal. 89 (1984) 168.
[12] P. Liu, J.A. Rodriguez, J. Phys. Chem. B 110 (2006) 194185.
[13] F. Viñes, J.A. Rodriguez, P. Liu, F. Illas, J. Catal. 260 (2008) 103.
[14] A. Galadima, R.P.K. Wells, J.A. Anderson, Appl. Petrochem. Res. 1 (2012) 35.
[15] J.A. Rodríguez, F. Illas, Phys. Chem. Chem. Phys. 14 (2012) 427.
[16] E. Florez, T. Gomez, P. Liu, J.A. Rodriguez, F. Illas, Chem. Cat. Chem. 2 (2010) 1219.
[17] E. Florez, L. Feria, F. Viñes, J.A. Rodriguez, F. Illas, J. Phys. Chem. C 113 (2009) 19994.
[18] J.A. Rodriguez, F. Viñes, F. Illas, P. Liu, Y. Takahashi, K.J. Nakamura, J. Chem. Phys. 127 (2007) 211102.
[19] L.K. Ono, B. Roldán-Cuenya, Catal. Lett. 113 (2007) 86.
[20] A. Naitabdi, L.K. Ono, B. Roldan Cuenya, Appl. Phys. Lett. 89 (2006) 043101.
[21] L.K. Ono, D. Sudfeld, B. Roldan Cuenya, Surf. Sci. 600 (2006) 5041.
[22] J.A. Rodríguez, L. Feria, T. Jirsak, Y. Takahashi, K. Nakamura, F. Illas, J. Am. Chem. Soc. 132 (2010) 3177.
[23] T. Gomez, E. Florez, J.A. Rodriguez, F. Illas, J. Phys. Chem. C 115 (2011) 11666.
[24] N.M. Schweitzer, J.A. Schaidle, O.K. Ezekoye, X. Pan, S. Linic, L.T. Thompson, J. Am. Chem. Soc. 133 (2011) 2378.
[25] S.V. Didziulis, P. Frantz, L.C.F. Torres, R.L. Guenard, O. El-bjeirami, S.S. Perry, J. Phys. Chem. B 105 (2001) 5196.
[26] P. Frantz, S.V. Didziulis, Surf. Sci. 413 (1998) 384.
[27] P.B. Merrill, S.S. Perry, P. Frantz, S.V. Didziulis, J. Phys. Chem. B 5647 (1998) 7606.
[28] P. Frantz, S.V. Didziulis, L.C.F. Torres, R.L. Guenard, S.S. Perry, J. Phys. Chem. B 106 (2002) 6456.
[29] S.V. Didziulis, H.I. Kim, J. Phys. Chem. C 111 (2007) 11275.
[30] T. Aizawa, W. Hayami, R. Souda, S. Otani, Y. Ishizawa, Surf. Sci. 381 (1997) 157.
[31] K. Edamoto, E. Miyazake, T. Anazawa, A. Mochida, Surf. Sci. 270 (1992) 389.
[32] S.V. Didziulis, K.D. Butcher, S.S. Perry, Inorg. Chem. 42 (2003) 7766.
[33] P. Liu, J.A. Rodriguez, J. Chem. Phys. 120 (2004) 5414.
[34] G.G. Asara, L. Feria, E. Florez, J.M. Ricart, P. Liu, J.A. Rodriguez, F. Illas, J. Phys. Chem. C 115 (2011) 22495.
[35] J. Ren, C.F. Huo, J. Wang, Y.W. Li, H. Jiao, Surf. Sci. 596 (2005) 212.
[36] W. Wu, Z. Wu, C. Liang, X. Chen, P. Ying, C. Li, J. Phys. Chem. B 3 (2003) 7088.
[37] J.S. Pilgrim, M.A. Ducan, J. Am. Chem. Soc. 115 (1993) 9724.
[38] J.P. Perdew, K.A. Jackson, M.R. Pederson, D.J. Singh, C. Fiolhais, Phys. Rev. B 46 (1992) 6671.
[39] J.P. Perdew, Y. Wang, Phys. Rev. B 45 (1992) 244.
[40] P.E. Blöchl, Phys. Rev. B 50 (1994) 17953.

[41] P.E. Blöchl, K. Johannes, J.F. Clemens, Condens. Matter Mater. Sci. 1 (2008).
[42] G. Kresse, D. Joubert, Phys. Rev. B 59 (1999) 1758.
[43] H.J. Monkhorst, J.D. Pack, Phys. Rev. B 13 (1976) 5188.
[44] G. Kresse, J. Hafner, Phys. Rev. B 47 (1993) 558.
[45] G. Kresse, J. Furthmuller, Phys. Rev. B 54 (1996) 11169.
[46] B. Meng, W.H. Weinberg, J. Chem. Phys. 100 (1994) 5280.
[47] W.S. Williams, J. Appl. Phys. 32 (1961) 552.
[48] G.E. Hollox, R.E. Smallman, Appl. Phys. 37 (37) (1966) 818.
[49] Y. Kumashiro, A. Itoh, S. Misawa, J. Less Common Met. 32 (1973) 32.
[50] W. Precht, G.E. Hollox, J. Cryst. Growth 3–4 (1968) 818.
[51] R.N. Storey, R.A. Laudise, J. Cryst. Growth 6 (1970) 261.
[52] A.L. Hagstrom, L.I. Johansson, S.B.M. Hagstrom, A. Christensen, J. Electron Spectrosc. 11 (1977) 75.
[53] S. Otani, S. Honma, T. Tanaka, Y. Ishizawa, J. Cryst. Growth 61 (1983) 1.
[54] M.E. Packer, M.J. Murray, J. Cryst. Growth 16 (1972) 240.
[55] I. Higashi, Y. Takahashi, T. Atoda, J. Cryst. Growth 33 (1976) 207.
[56] I. Zergioti, A. Hatziapostolou, E. Hontzopoulos, A. Zervaki, G.N. Haidemenopoulos, Thin Solid Films 271 (1995) 96.
[57] C. Bisch, M. Nadal, F. Teyssandier, M. Bancel, B. Vallon, Mater. Sci. Eng. A Struct. 202 (1995) 238.
[58] A. Kato, N. Tamari, J. Cryst. Growth 49 (1980) 199.
[59] X.K. Li, Z.J. Dong, A. Westwood, A. Brown, R. Brydson, A. Walton, G.M. Yuan, Z.W. Cui, Y. Cong, Cryst. Growth Des. 11 (2011) 3122.
[60] G. Spoto, E.N. Gribov, G. Ricchiardi, A. Damin, D. Scarano, S. Bordiga, C. Lamberti, A. Zecchina, Prog. Surf. Sci. 76 (2004) 71.
[61] P.J. Feibelman, B. Hammer, J.K. Nørskov, F. Wagner, M. Scheffler, R. Stumpf, R. Watwe, J. Dumesic, J. Phys. Chem. B 105 (2001) 4018.
[62] D.P. Woodruff, A.M. Bradshaw, Rep. Prog. Phys. 57 (1994) 1029.
[63] F. Illas, S. Zurita, J. Rubio, A.M. Marquez, Phys. Rev. B 52 (1995) 12372.
[64] F. Illas, S. Zurita, A.M. Marquez, J. Rubio, Surf. Sci. 376 (1997) 279.
[65] J.L.C. Fajin, M.N.D.S. Cordeiro, J.R.B. Gomes, Appl. Catal. Gen. 379 (2010) 111.
[66] J.S. Pilgrim, M.A. Duncan, J. Am. Chem. Soc. 115 (1993) 9724.
[67] M. Patzschke, D. Sundholm, J. Phys. Chem. B 109 (2005) 12503.
[68] P. Scherrer, Götting. Nachr. Gesell. 2 (1918) 98.

Chapter 4

Water gas shift reaction (WGSR) on Au/TiC novel catalyst

The chapter reports a joint experimental - theoretical study elucidating the mechanism for the hydrogenation of CO_2 on the Au/TiC system. The theoretical investigation has been made in collaboration between our laboratory and groups of IQTC-UB and experiments have been carried out at Brookhaven National Laboratory, BNL (USA). Results obtained have been recently submitted to publication[1] and also gave the main motivation for all work reported in the next chapter.

CO_2 conversion is nowadays a brain-teaser problem for scientists around the world. It has central importance to solve global warming reducing the high quantities of this extremely pollutant gas emitted nowadays by human activities. In addition carbon dioxide can be the starting material for compounds further used as chemicals to produce fuels and alcohols.

Reverse water gas shift reaction (RWGS) is an easy way to begin the reconversion process. In RWGS CO_2 is reduced using molecular hydrogen and obtaining CO and water passing through several intermediates. The first step after the adsorption and activation of CO_2 is normally the addition of hydrogen. Depending where attach occurs several formate isomers with different stability are produced. However after cleavage of one C-O bond all moieties can be in principle converted into methanol. Breaking the second C-O bond forms surface CH_x (x = 0-3) units that can participate to heavier alcohols synthesis but also produce hydrocarbons through the Fisher-Tropsch (F-T) reaction, or be further reduced producing methane.

Recent experiments[2,3] performed on small gold nanoparticles adsorbed on single crystal TiC grown along the (001) direction reported very high reaction rates for CO_2 hydrogenation. The same experiments pointed out that high production of methanol and carbon monoxide is favoured by low Au coverage and flat 2D nanoparticles.

In this study we firstly identified the minimum energy path (MEP) for the complete conversion of CO and water to CO_2 and H_2 characterising reactants, products, intermediates and transition states involved. By definition the MEP coincides for both direct and reverse reaction so any process can be studied in the direction we prefer and on top of that at working temperature the reaction is in equilibrium. For this reason only the pathway that brings from CO and water to carbon dioxide and molecular hydrogen will be discussed. Such process, known as *Water Gas Shift Reaction*, (WGSR), has its own importance as it is one of the most important ways used to produce molecular hydrogen[4]

The identification of the transition states connecting the key stable intermediates of the WGSR allowed explain the good experimental activity seen. Comparing our new results obtained for the Au_4/TiC (001) system with those obtained previously for the reaction on the clean TiC (001) surface the whole process can be understood. The support acts cleaving one O – H bond of water, producing the OH species that will later oxidize carbon monoxide. This step is followed by formate dehydrogenation and recombination of atomic hydrogen.

In a second moment the kinetic information derived from the periodic density functional calculation was used for the *ab-initio* prediction of the reaction rates. On Au_4/TiC the rate limiting step (RLS) for the reaction is predicted to be the cleavage of the O – H to form CO_2, where the RLS on TiC (001) is the formation of the second C - O bond. [5]

The calculated rate constant for CO_2 dehydrogenation is about a hundred thousand times slower on the supported gold nanoparticle than on TiC (001), where the formation of the second C – O bond is about 100 million times faster on Au_4/TiC than on the bare support.[5] These combined effects reflect the experiments identifying Au/TiC an active catalyst for the water gas shift reaction.

References

1 J. A. Rodriguez, P. J. Ramírez, G. G. Asara, F. Viñes, J. Evans, P. Liu, J. M. Ricart, F. Illas, submitted.

2 J. A. Rodriguez, J. Evans, L. Feria, A. B. Vidal, P. Liu, K. Nakamura, F. Illas, J. Catal., 2013, 307, 162.

3 A. B. Vidal, L. Feria, J. Evans, Y. Takahashi, P. Liu, K. Nakamura, F. Illas, J. A. Rodriguez, J. Phys. Chem. Lett., 2012, 3, 2275.

4 R. B. Burch, Phys. Chem. Chem. Phys., 2006, 8, 5483.

5 F. Viñes, J. A. Rodriguez, P. Liu, F. Illas, J. Catal., 2008, 260, 103.

This is the pre-peer reviewed version of the following article: Angewandte Chemie International Edition, 2014, 53, 1–6, which has been published in final form at http://onlinelibrary.wiley.com/doi/10.1002/ange.201407208/abstract.

Charge Polarization at a Au-TiC Interface and the Generation of Highly Active and Selective Catalysts for the Low-Temperature Water Gas Shift Reaction.

José A. Rodriguez,*[a] Pedro J. Ramírez,[a,b] Gian Giacomo Asara,[c,d] Francesc Viñes,[d] Jaime Evans,[b] Ping Liu,[a] Josep M. Ricart,[c] Francesc Illas[d]

[a] Chemistry Department, Brookhaven National Laboratory Upton, NY 11973 (USA)
** E-mail: rodrigez@bnl.gov*
[b] Facultad de Ciencias, Universidad Central de Venezuela Caracas 1020A (Venezuela)
[c] Departament de Química Física i Inorgànica, Universitat Rovira i Virgili, C/ Marcel·lí Domingo s/n, 43007 Tarragona (Spain)
[d] Departament de Química Física & IQTCUB, Universitat de Barcelona, C/Martí i Franquès 1, 08028 Barcelona (Spain)

Transition metal nanoparticles dispersed on oxides or carbon supports are among the most frequently used catalysts in the chemical and petrochemical industries. In principle, by selecting the right combination of metal and support, one could reduce substantially the energy necessary for chemical transformations and optimize the use of chemical feedstock.[1] Metal-support interactions can have negative[2,3] or positive[4,5] effects on the catalytic properties of a metal. A major challenge in heterogeneous catalysis is to understand metal-support interactions at an atomic level and use them to design highly active and selective catalysts.[1,4,5] In the last decades, a large effort has been focused on the study of metal-oxide interactions.[1] However, in recent years, it has become clear that metal carbides can be excellent supports for the dispersion of metal catalysts.[6,7,8,9,10] The metal carbides have interesting catalytic properties on their own,[11,12,13,14,15,16,17,18] and they also can modify the reactivity of a supported metal through chemical bonding.[8,19] In this article we investigate the performance of Au/TiC(001) surfaces as catalysts for the water-gas shift reaction ($CO + H_2O \rightarrow H_2 + CO_2$, WGS). The WGS is a key process in the industrial production of hydrogen.[20,21] Commercial catalysts for the WGS usually involve mixtures Fe-Cr and Cu-Zn oxides, used at temperatures between 620-770 K and 470-525 K, respectively.[20] These catalysts normally require lengthy and complex activation steps before usage. There is a general desire to find WGS catalysts active at relatively low temperatures (< 470 K).[20] Metal-carbide based catalysts can accomplish this task[6,14,17,18] but there are serious concerns about their stability and selectivity.[14,18] Many metal carbides are sensitive to O_2 or O-containing molecules in the reaction feed.[11,14,18] On the other hand, metal carbides can be

very active for the breaking of the C-O bond in carbon monoxide[11,22] and, in the presence of hydrogen, hydrogenate the produced C atoms to yield methane or higher alkanes.[10,13,15,16,23] Our study indicates that the 1:1 metal-to-carbon ratio in TiC gives stability to this carbide substrate and prevents the cleavage of C-O bonds. Strong metal-support interactions make Au/TiC(001) a highly active and selective catalyst for the low-temperature WGS reaction.

Fig. 1 shows the WGS activity for clean TiC(001) and Au/TiC(001) surfaces as a function of Au coverage. We found that the clean TiC(001) surface is able to catalyze the WGS, in agreement with the predictions of previous DFT calculations.[17] In fact, at 450 K, TiC(001) displays a WGS activity larger than that of Cu(111), a typical benchmark in WGS studies.[24] Metallic Au does not catalyze the WGS.[25,26,26] In spite of this, the addition of Au to TiC(001) produces a drastic increase in the WGS activity of the system. A maximum in the production of H_2 and CO_2 is observed at θ_{Au} ~ 0.15 ML. After this point, there is a gradual decrease in the WGS activity of Au/TiC(001). Studies of STM have shown that at coverage of 0.1 ML a large fraction of the Au particles exhibits a height of ~ 0.2 nm with respect to the carbide substrate (Fig. 2).[8,19] These small particles are two dimensional (i.e. one single Au layer) and have a diameter below 0.6 nm.[8,19]

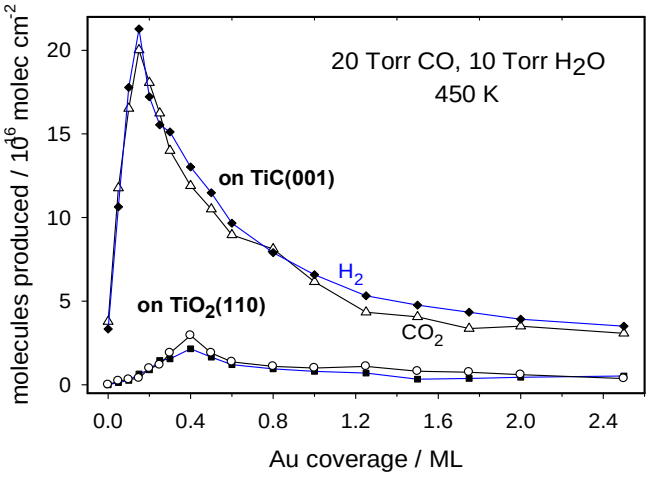

Figure 1. WGS activity of Au/TiC(001) and Au/TiO_2(110) as a function of Au coverage. The reported values for the production of H_2 (filled symbols) and CO_2 (empty symbols) were obtained after exposing the catalysts to 20 Torr of CO and 10 Torr of H_2O at 450 K for 5 min.

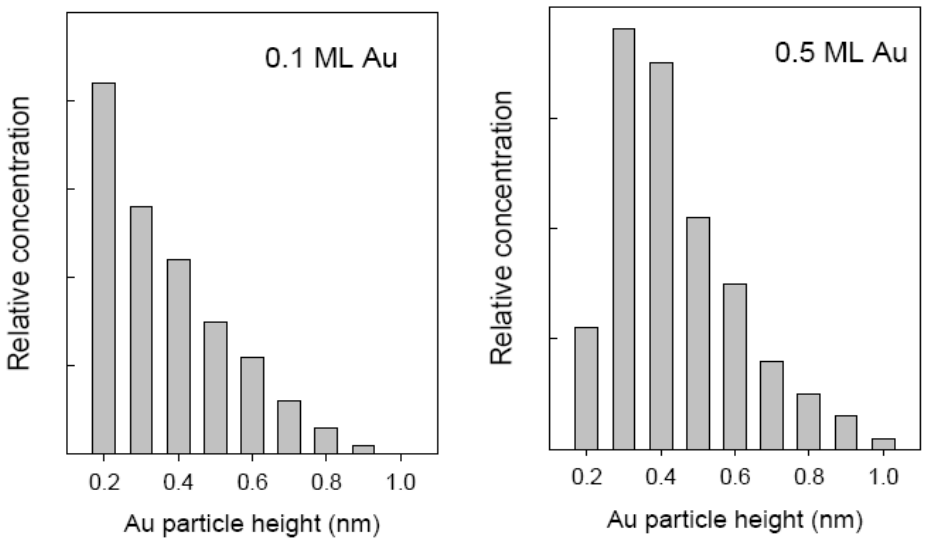

Figure 2. Distribution of Au particle heights seen in STM images for 0.1 and 0.5 ML of gold on TiC(001). Au was vapor deposited at 300 K and the Au/TiC(001) surfaces were annealed to 550 K before taken the STM images (ref. 19 in main text).

The Au atoms in this particles are in direct contact with the C sites of the TiC(001) substrate undergoing a charge polarization[25] that shifts electrons towards upcoming molecules (Fig. 3) and enhances their chemical reactivity.[8,9,19]

At coverages above 0.2 ML, the gold form predominantly three-dimensional particles on TiC[7,8,26] (i.e. the Au atoms exposed to the reactants are not electronically modified by interactions with the carbide support) and the chemical reactivity of the system decreases.[8,19] In XPS experiments for the partial dissociation of water on Au/TiC(001), $H_2O \rightarrow OH + H$, we found an extremely high reactivity for surfaces that had a gold coverage below 0.2 ML (Fig. 4).

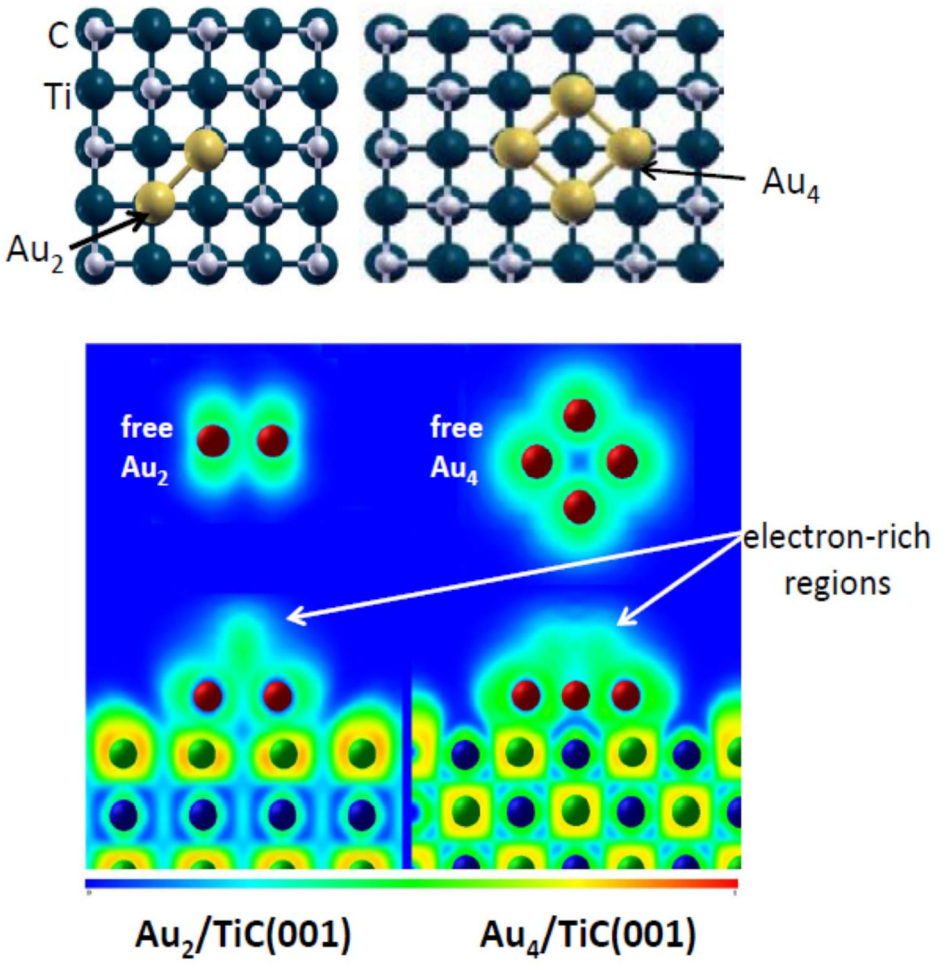

Figure 3. Top: Bonding configurations for Au_2 and Au_4 on TiC(001). Bottom: Topological analysis of the electron localization function (ELF map, ref 25 in main text) for Au_2 and Au_4 on TiC (001). On the right side is shown a cut along a diagonal of the Au_4 cluster.

This is quite interesting because extended surfaces and isolated nanoparticles of gold do not dissociate the water molecule.[27] Upon the dissociative adsorption of water on the Au/TiC(001) (θ_{Au} < 0.2 ML) systems, we observed a shift of 0.7-0.8 eV in the Au $4f_{7/2}$ binding energy in XPS (Fig. 4), which is consistent with the formation of Au-(OH)x compounds on the surface.

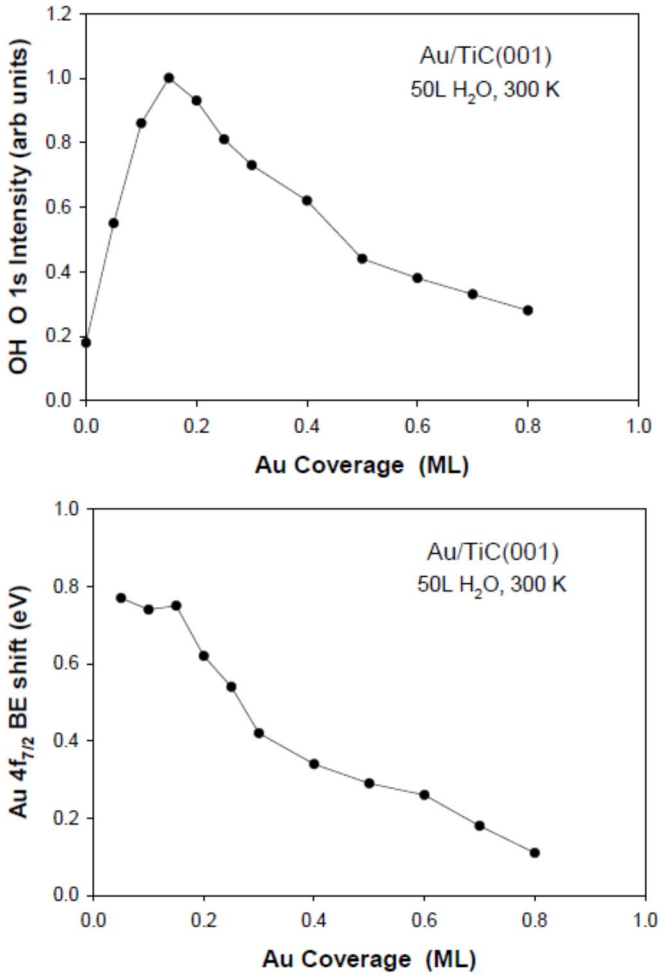

Figure 4: Top: Intensity of the OH signal in the O 1s region of XPS after dosing 50 L of water at 300 K to TiC(001) and Au/TiC(001) surfaces with different coverages of gold. Bottom: Corresponding shift in the Au $4f_{7/2}$ binding energy upon the dissociative adsorption of water on the Au/TiC(001) surfaces. At Au coverages above 0.2 ML, the reactivity of the Au/TiC(001) surface for water dissociation decreased with increasing Au coverage.

These compounds are active species for the WGS reaction on Au/oxide catalysts.[21,28] In Fig. 1, we compare the WGS activity of a series of Au/TiC(001) and $Au/TiO_2(110)$ surfaces with similar coverages of the admetal. At temperatures of 550 - 625 K, Au/TiO_2 is known to be a very good catalyst for the WGS[28,29] with an activity that is higher than that of Cu/ZnO[30] which is used as an industrial WGS catalyst.[20] The results in Fig. 1 indicate that Au/TiC(001) is a much better low-temperature WGS catalysts than $Au/TiO_2(110)$. This is corroborated

by the data shown in the Arrhenius plots of Fig. 5. The apparent activation energy for the WGS process decreases from 18 ± 2 kcal/mol on Cu(111) to 10 ± 3 kcal/mol on Au/TiO_2(110) and 8 ± 2 kcal/mol on Au/TiC(001).

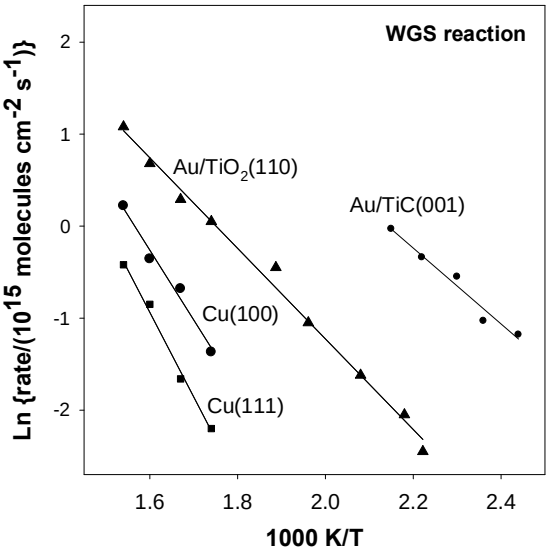

Figure 5. Arrhenius plots for the WGS on Cu(111), Cu(100), Au/TiO_2(110) and Au/TiC(001) catalysts (20 Torr of CO and 10 Torr of H_2O). Surfaces of metallic Au are not active for the WGS reaction. The data for Cu(111), Cu(100), Cu(111) and Au/TiO_2(110) were taken from refs.[26,27]. The coverages of Au on TiO_2(110) and TiC(001) were 0.4 and 0.15 ML, respectively. At these coverages maximum catalytic activity was observed for Au/TiO_2(110) and Au/TiC(001).

The apparent activation energy on Au/TiO_2(110) is close to that found on Au/TiO_2 powders, 11 kcal/mol.[21,28] At relatively low temperatures (< 470 K), Au/TiC(001) exhibits a WGS activity that is observed on copper surfaces and on Cu/oxide or Au/oxide (oxide= TiO_2, ZnO, CeO_2, MgO) catalysts only at elevated temperatures (> 500 K).[29,30] From the data points in Figure 5, we estimated turnover frequencies (TOFs) for Au/TiC(001) assuming that all the gold atoms in the catalyst were involved in the WGS process. This is a valid assumption since STM shows that at a low coverage of Au (~ 0.15 ML) the admetal grows forming a substantial amount of 2D islands on TiC(001).[8,19] The estimated TOFs at different temperatures are shown in the top panel in Fig. 6. The bottom panel compares TOFs for several catalysts.

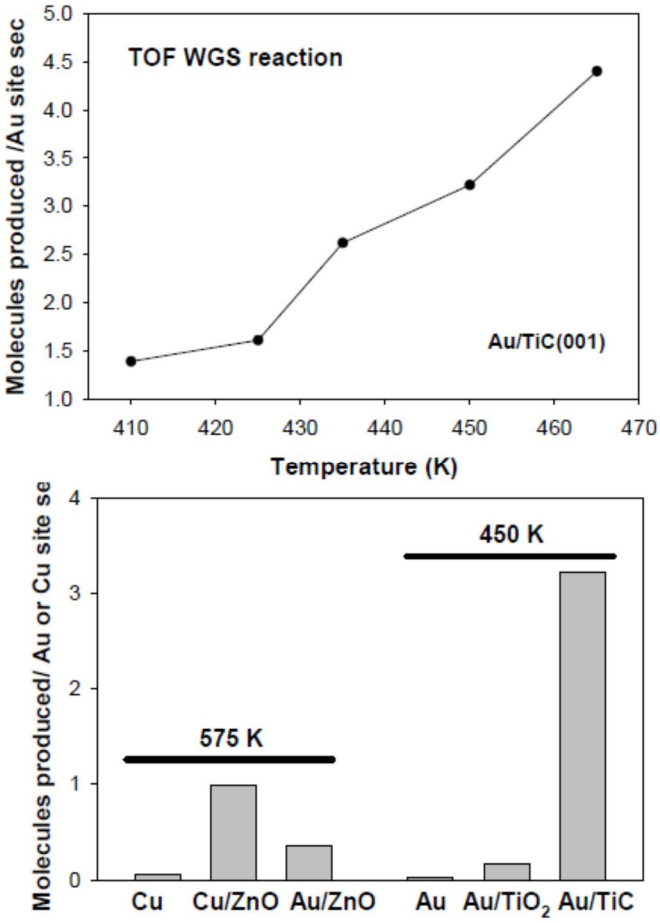

Figure 6. Top: TOFs for the WGS reaction on Au/TiC(001) at different temperatures. Bottom: Comparison of the TOFs for the WGS on Cu(111),[26] Cu/ZnO(000ī),[27] Au/ZnO(000ī),[27] Au(111),[26] $Au/TiO_2(110)$[26] and Au/TiC(001). In all cases, the pressures of CO and H_2O were 20 and 10 Torr, respectively.

Again it is clear that Au/TiC(001) is an excellent catalyst for the WGS reaction. At 450 K, the $Au/TiO_2(110)$ surface exhibits a TOF close to that reported for Au/TiO_2 powder catalysts, ~ 0.2 s^{-1},[21] but much smaller than that seen for Au/TiC(001), 3.2 s^{-1}. Furthermore, a Cu/ZnO(000ī) surface, which models industrial Cu/ZnO catalysts,[30] displays a TOF ~ 3 times smaller than that of Au/TiC(001) in spite of an increase of 125 K in the reaction temperature. As mentioned above, two important issues when dealing with the use of metal carbides as possible catalysts for the WGS are selectivity and stability.[14,15,16,17,18] In many industrial operations, the WGS is performed under hydrogen rich conditions with mixtures of $CO/H_2O/H_2$ that come from the reforming of hydrocarbons.[6,14] Under hydrogen rich conditions metal carbides such as Mo_2C transform CO into

methane as a side reaction.[15,22] Indeed, after exposing a $Mo_2C(001)$ surface to a $CO/H_2O/H_2$ mixture, we found products for the WGS and CO methanation (Fig. 7). We carried out studies comparing the WGS process on Au/TiC(001) and $Au/Mo_2C(001)$ using $CO/H_2O/H_2$ mixtures. A gold coverage of ~ 0.15 ML was deposited on TiC(001) and on a $Mo_2C(001)$ surface.[13] The results are summarized in Fig 7. Neither TiC(001) nor Au/TiC(001) produce methane as a reaction product. These catalysts only produce CO_2 through the WGS reaction.

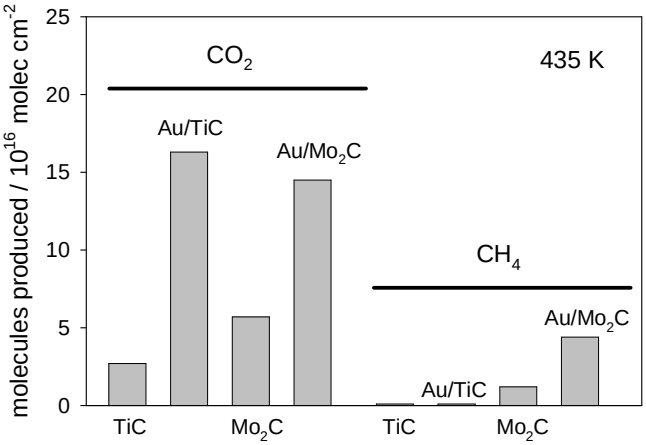

Figure 7. Production of CO_2 and CH_4 after exposing TiC(001), Au/TiC(001), $Mo_2C(001)$ and $Au/Mo_2C(001)$ catalysts to a mixture of 20 Torr of CO, 10 Torr of H_2O and 100 Torr of H_2 at 435 K for 5 minutes.

In general terms, $Mo_2C(001)$ is more active than TiC(001) for the conversion of CO, but the molybdenum carbide produces a significant amount of methane. The addition of Au to $Mo_2C(001)$ produces an excellent catalyst for the conversion of CO at low temperature, but it increases simultaneously the production of CO_2/H_2 and methane. In Figure 7, Au/TiC(001) is the best WGS catalyst in terms of activity and selectivity. It is known that the 1:1 metal-to-carbon ratio in TiC(001) makes very difficult the cleavage of the C-O bond in carbon monoxide ($CO_{ads} \rightarrow C_{ads} + O_{ads}$, ΔE= + 1.65 eV).[9,13] This 1:1 metal-to-carbon ratio also makes TiC(001) less sensitive to the presence of water in the reaction feed.[17] After 6 hours of operation we found no signs for deactivation of the Au/TiC(001) catalyst during the WGS (Fig. 8).

In contrast, the $Au/Mo_2C(001)$ catalyst lost ~ 30% of its activity during the same period of time (Fig. 8). Mo_2C powders and $Mo_2C(001)$ decompose the water molecule to form films of oxycarbides which have low catalytic activity.[14,18] This deactivation process was negligible on TiC(001) and Au/TiC(001).

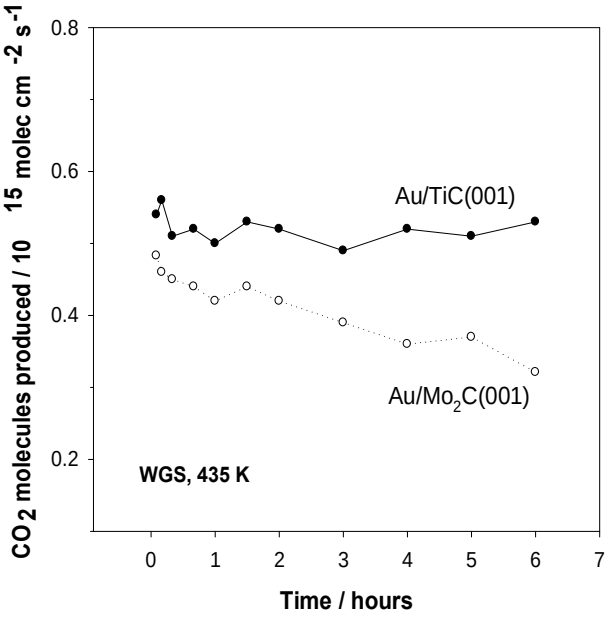

Figure 8 Production of CO_2 as a function of time after exposing Au/TiC(001) and Au/Mo_2C(001) catalysts to a mixture of CO/H_2O/H_2 at 435 K. Initial pressures: 20 Torr of CO, 10 Torr of H_2O and 100 Torr of H_2. A coverage of 0.15 ML of Au was deposited on the TiC(001) and Mo_2C(001) surfaces to generate the catalysts.

DFT calculations were used to study the mechanism of the WGS reaction on Au/TiC(001). First, the bonding of CO and water was examined on Au_4, Au_{13} and Au_{29} clusters supported on a TiC(001) slab (Fig. 3 and 9). Au_{13} consisted of two layers of 9 and 4 metal atoms. Au_{29} contained three layers of 16, 9 and 4 Au atoms. Both clusters ended in a Au_4 unit as seen in Au_4/TiC(001), Fig. 3, but in the case of Au_{13}/TiC(001) and Au_{29}/TiC(001) the tip of the gold cluster was not in contact with the carbide substrate, Fig. 9. The strength of the bonding interactions of water with the Au clusters increased following the sequence: Au_{29}/TiC ≈ Au_{13}/TiC << Au_4/TiC, in agreement with the trend seen in our experiments for adsorption of water on Au/TiC(001), Fig. 2 and 4.

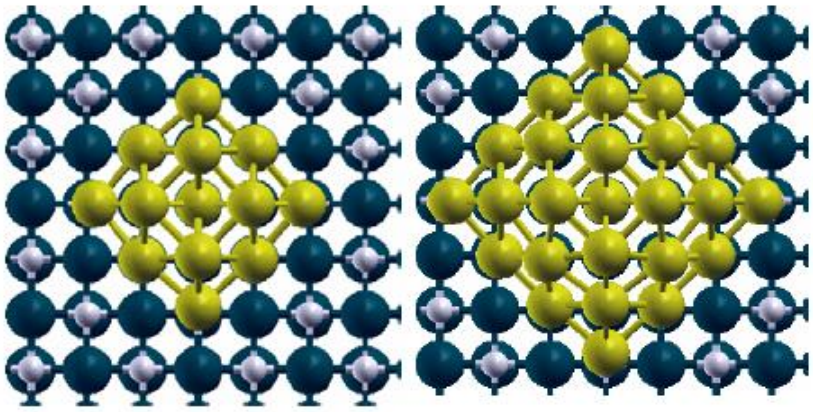

Figure 9: Au_{13} and Au_{29} clusters used to investigate the bonding of water to a Au/TiC(001) catalysts.

Thus, the active sites for the WGS on Au/TiC(001) are small metal clusters in close contact with the support. Something similar has been reported for Au/oxide catalysts.[21,28] Fig. 10 compares the calculated reaction profiles for the WGS on clean TiC(001)[17] and Au_4/TiC(001). The corresponding molecular structures for the reaction intermediates and transition states are displayed in Fig. 11. Our theoretical study indicated that the WGS reaction prefers the Au sites. The optimal path for the WGS on Au/TiC(001) follows and associative mechanism in which a HOCO species is formed after reacting CO with an OH group produced by the dissociation of water. The formation of a key HOCO intermediate has also been proposed in previous theoretical studies for the WGS on Cu(111),[31] CeO_x/Cu(111)[32] and Au/TiO_2(110).[33] Table 1 lists the calculated reaction rate constants for the main steps of the WGS on Au_4/TiC(001) based on the DFT calculations. It is remarkable that on Au_4/TiC(001) the formation of the HOCO intermediate is an exothermic process that occurs with extremely low activation barriers which are significantly smaller than those found on TiC(001), 0.87 eV,[17] or pure gold, > 2eV.[27] On clean TiC(001), the calculated rate constant at 300 K for the CO + OH → cis-HOCO reaction was only 3.20 s^{-1} $site^{-1}$ [17] while on Au_4/TiC(001) the corresponding rate was $9.63 \cdot 10^7$ s^{-1} $site^{-1}$. Surfaces of pure gold do not dissociate water.[27]

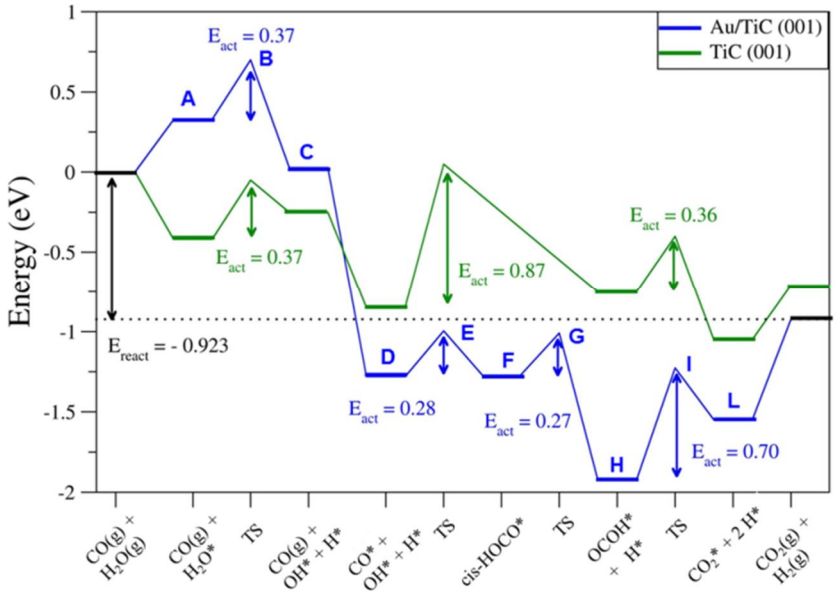

Figure 10. DFT calculated energy profile for the WGS reaction on clean TiC(001)[17] and Au_4/TiC(001). The corresponding molecular structures are shown in Fig. 11.

Table 1. Calculated barriers and rate constants at for main steps of the WGS on Au_4/TiC(001). E_{act} is in eV/molecule and rate constants (RC) in s^{-1} $site^{-1}$.

Reaction	Eact	RC (300 K)	RC(450 K)
H_2O → OH + H	0.37	5.44×10^5	6.49×10^7
CO + OH → cis-HOCO	0.28	9.63×10^7	5.41×10^9
cis-HOCO → trans-OCOH	0.27	1.27×10^7	3.70×10^8
OCOH → CO_2 + H	0.70	1.32	1.06×10^4

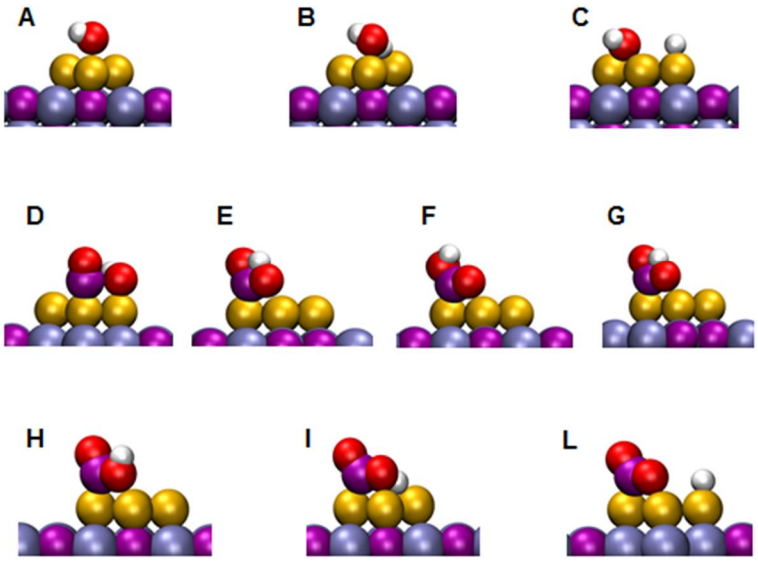

Figure 11. Calculated DFT molecular structures for intermediates and TS of the WGS on a Au_4/TiC(001) model catalyst. The corresponding energy profile is shown in Figure 10. Color code: yellow, Au; purple, C; grey, Ti; red, O; white, H.

In contrast, the rate constant for the dissociation of water on a Au_4 cluster supported on TiC(001) is $5.44 \cdot 10^5$ s^{-1} $site^{-1}$ at 300 K. Thus, the charge polarization at the Au-TiC interface (Figure 3)[8,25] drastically enhances the catalytic properties of gold.

A detailed comparison of the behavior of Au on TiC(001) and TiO_2(110) or ZnO(000$\bar{1}$) in Figure 6 points to stronger metal-support interactions on the carbide surface which make this substrate the best option for enhancing the WGS activity of Au. Charge polarization can also occur when Au is deposited on oxide surfaces,[34,35,36] but it is usually weaker than seen on the TiC(001) substrate[8,25] requiring a modification of the standard properties of the oxide surface. A perturbation of the electronic properties of Au is a preliminary step to enhance its chemical activity, and on oxides this task can be accomplished by introducing structural or electronic defects, by creating O vacancies, and by forming Au-$(OH)_x$ species.[21,28,34,35,36] On the other hand, the simple deposition of Au on stoichiometric TiC electronically perturbs the gold.[8,25] As a result, supported Au is able to dissociate water, a bottleneck on surfaces of pure gold,[27] and the other reaction steps for the WGS proceed on the admetal at a reasonable speed. In addition, the 1:1 metal-to- carbon ratio in TiC provides stability and prevents the transformation of CO into methane. Thus, in Au/TiC(001), one has a highly active and selective catalyst for the low temperature WGS reaction.

Experimental Section

The Au/TiC(001) and Au/Mo_2C(001) catalysts were prepared and tested in an ultrahigh vacuum chamber that has attached a high-pressure cell or batch reactor.[13,30,33] Au was deposited on the metal carbide substrates following the methodology described in refs. 19 and 25. The procedures followed for the cleaning of the TiC(001) and Mo_2C(001) surfaces are described elsewhere.[13,19,25] In the experiments, the WGS activity of the metal/carbide catalysts was tested under mixtures of CO/H_2O or CO/H_2O/H_2.[14,28,29] The CO gas was stored on aluminium tanks and cleaned of any metal carbonyl impurity by passing it through purification traps.

The periodic DFT calculations estimated exchange and correlation energy using the PW91-GGA[37] approximation as implemented in VASP.[38] The wave function was expanded using a plane wave basis set whose associated kinetic energy was lower than 415 eV. A suitable net of 3×3×1 **k** points generated using Monkhorst-Pack algorithm was used to perform integration in the reciprocal space.[39] The Au_4 cluster was adsorbed on a 3(√2×√2)R45º supercell and fully relaxed together with all adsorbates and the two upper layers of the slab until forces were smaller than 0.02 eV $Å^{-1}$. About 10 Å of vacuum perpendicular to the surface avoided interaction between repeated images. Transition states were identified using CI-NEB algorithm.[40] All structures were characterised as proper minima or saddle points by vibrational analysis. Reaction rate constants (T= 300 or 450 K) were estimated from standard transition state theory including the calculation of the vibrational partition function as detailed elsewhere.[17]

Acknowledgements
The work at BNL was financed by the US Department of Energy (DOE), Office of Basic Energy Science (DE-AC02-98CH10086). This work has been supported by the Spanish MINECO grant CTQ2012-30751 grant and, in part, by Generalitat de Catalunya grants 2014SGR97 and XRQTC. INTEVEP and IDB financed the work done at UCV. G.-G. A. thanks the *Universitat Rovira i Virgili* for supporting his predoctoral research. F.V. thanks the MINECO for a postdoctoral *Ramón y Cajal* grant (RYC-2012-10129). F.I. acknowledges additional support through the ICREA Academic award for excellence in research. Computational time at the MARENOSTRUM supercomputer has been generously provided by the Barcelona Supercomputer Centre through a grant from *Red Española de Supercomputación.*

References

1 C. T. Campbell, Nature Chemistry, 2012, 4, 597.

2 S. J. Tauster, Acc. Chem. Research, 1987, 20, 389.

3 A. K. Datye, D. S. Kalakkad, M. H. Yao, D. J. Smith, J. Catal., 1995, 155, 148.

4 A. Bruix, J. A. Rodriguez, P. J. Ramírez, S. D. Senanayake, J. Evans, J. B. Park, D. Stacchiola, P. Liu, J. Hrbek, F. Illas, J. Am. Chem. Soc., 2012, 134, 8968.

5 S. D. Senanayake, J. A. Rodriguez, D. Stacchiola, Topics in Catal., 2013, 56, 1488.

6 N. M. Schweitzer, J. A. Schaidle, O.K. Ezekoye, X. Pan, S. Linic, L.T. Thompson, J. Am. Chem. Soc., 2011, 133, 2378.

7 L. K. Ono, B. Roldán-Cuenya, Catal. Lett., 2007, 113, 86.

8 J. A. Rodriguez, F. Illas, Phys. Chem. Chem. Phys., 2012, 14, 427.

9 A. Vidal, L. Feria, J. Evans, Y. Takahashi, P. Liu, K. Nakamura, F. Illas, J. A. Rodriguez, J. Phys. Chem. Lett., 2012, 3, 2275.

10 M. D. Porosoff, X. Yang, J. A. Boscoboinik, J. G. Chen., Angew. Chem. Int. Ed., 2014, 53, 1.

11 H. H. Hwu, J. G. Chen, Chem. Rev., 2005, 105, 185.

12 S. T. Oyama, Catal. Today, 1992, 15, 179.

13 S. Posada-Pérez, F. Viñes, P. J. Ramírez, A. B. Vidal, J. A. Rodriguez, F. Illas, Phys. Chem. Chem. Phys, 2014, 16, 14912.

14 D. J. Moon, J. W. Ryu, Catal. Lett., 2004, 92, 17.

15 P. M. Patterson, T. K. Das, B. H. Davis, Applied Catal. A: General, 2003, 251, 449.

16 S. V. Didziulis, K. D. Butcher, Coord. Chem. Rev., 2013, 257, 93.

17 F. Viñes, P. Liu, J. A. Rodriguez, F. Illas, J. Catal. 2008, 260, 103.

18 P. Liu, J. A. Rodriguez, J. Phys. Chem. B, 2006, 110, 19418.

19 J. A. Rodriguez, P. Liu, F. Viñes, F. Illas, Y. Takahashi, K. Nakamura, Angew. Chem. Int. Ed., 2008, 47, 6685.

20 R. B. Burch, Phys. Chem. Chem. Phys., 2006, 8, 5483.

21 M. Flytzani-Stephanopoulos, Acc. Chem. Res., 2014, 47, 783.

22 K. - Z. Qi, G. - C. Wang, W. - J. Zheng, Surf. Sci., 2013, 614, 53.

23 J. - L. Dubois, K. Sayama, H. Arakawa, Chem. Lett., 1992, 5.

24 J. Nakamura, J. M. Campbell, C. T. Campbell, J. Chem. Soc., Faraday Trans., 1990, 86, 2725.

25 L. K. Ono, D. Sudfeld, B. Roldán-Cuenya, Surf. Sci., 2006, 600, 5041.

26 J. A. Rodriguez, P. Liu, F. Viñes, F. Illas, Y. Takahashi, K. Nakamura, J. Chem. Phys., 2007, 127, 211102.

27 P. Liu, J. A. Rodriguez, J. Chem. Phys., 2007, 126, 164705.

28 M. Yang, L.F. Allard, M. Flytzani-Stephanopoulos, J. Am. Chem. Soc. 2013, 135, 3768.

29 R. Si, J. Tao, J. Evans, J.-B. Park, L. Barrio, J.C. Hanson, Y. Zhu, J. Hrbek, J.A. Rodriguez, J. Phys. Chem. C, 2012, 116, 23547.

30 J.A. Rodriguez, P. Liu, J. Hrbek, J. Evans, M. Perez, Angew. Chem. Int. Ed., 2007, 46, 1329.

31 A. A. Gokhale, J.A. Dumesic, M. Mavrikakis, J. Am. Chem. Soc. 2008, 130, 1402.

32 K. Mudiyanselage, S. D. Senanayake, L. Feria, S. Kundu, A. E. Baber, J. Graciani, A. B. Vidal, S. Agnoli, J. Evans, R. Chang, S. Axnanda, Z. Liu, J. F. Sanz, P. Liu, J. A. Rodriguez, D. J. Stacchiola, Angew. Chem. Int. Ed., 2013, 52, 5101.

33 J. A. Rodriguez, J. Evans, J. Graciani, J. - B. Park, P. Liu, J. Hrbek, J. F. Sanz, J. Phys. Chem. C, 2009, 113, 7364.

34 D. Ricci, A. Bongiorno, G. Pacchioni, U. Landman, Phys. Rev. Lett., 2006, 97, 036106.

35 M. Sterrer, T. Risse, U. Martinez Pozzoni, L. Giordano, M. Heyde, H.-P. Rust, G. Pacchioni, H.-J. Freund, Phys. Rev. Lett., 2007, 98, 096107.

36 S. Laursen, S. Linic, J. Phys. Chem. C, 2009, 113, 6689.

37 Y. Wang, J. P. Perdew, Phys. Rev. B, 1991, 43, 8911.

38 G. Kresse, J. Furthmüller, Comput. Mater. Sci., 1996, 6, 15.

39 H. J. Monkhorst, J. D. Pack, Phys. Rev. B, 1976, 13, 5188.

40 G. Henkelman, B. P. Uberuaga, H. Jónsson, J. Chem. Phys., 2000, 113, 9901.

Chapter 5

Syngas reactivity on Au/TiC system

This chapter investigates the hydrogenation of carbon monoxide on the clean TiC (001) surface support and on Au_4 and Au_6 nanoparticle models adsorbed thereon. Results obtained are resumed in the draft reproduced after this introduction and will be soon submitted for publication.[1]

Theoretical results presented in the previous chapter together with recent experimental data demonstrated that small gold nanoparticles adsorbed on TiC are able to catalytically hydrogenate carbon dioxide producing CO and, to a lesser extent, methanol.[2] Our periodic DFT study using the Au_4/TiC (001) model system demonstrated that the catalyst is able to cleave one C – O bond from the hydrogenated carbon dioxide at low temperature agreeing with the experimental detection of high quantities of CO that populates the surface of the catalyst and the gold nanoparticles. From previous theoretical studies it is known that small Au nanoparticles adsorbed on the (001) surface of TiC can easily dissociate molecular hydrogen and that carbon monoxide adsorbs slightly stronger on the surface carbons than on the nanoparticle.[3,4] Consequently CO hydrogenation was considered to be one probable way for methanol production.

The first part of the work focused on the reactivity of *syngas* (a mixture of CO and H_2) on the bare support. A wide reaction network was studied including the whole pathway leading to formaldehyde, H_2CO.

This reactive pathway is thermodynamically viable despite of the small endothermicity of the process and it is the kinetically preferred between those explored, but it is still highly hindered due to activation barrier higher than ~1.3 eV. The activation energies calculated for the cleavage of C – O bond of carbon monoxide or HCO were higher than ~2.4 eV make also these processes rare turning TiC (001) inert toward syngas.

HCO formation through carbon monoxide hydrogenation was then studied on two 2D small nanoparticles models: Au_4 and Au_6. The crucial difference between the two models relies on the effect of their structure on the geometry adopted by the reactants during the formation of the new C – H bond. In fact, the smaller Au_4 adopts a square geometry and presents just one kind of atoms here referred as "corner" whereas Au_6, whose atoms occupy two adjacent rows of surface carbons, presents also another kind of gold atoms, defined as "edge". This feature, present on the Au_6 cluster allows the reactants to get closer when co-adsorbed, and the bond formation turns to be a coplanar movement of CO and H. In the case of Au_4 the reactants adsorb on adjacent gold atoms, and need to move along nearly perpendicular planes to form the new bond. This subtle difference results in a change in calculated activation energy that passes from the 1.80 eV, calculated for the reaction on the bigger cluster, to 1.93 eV for the reaction on the smaller Au_4 cluster. Those activation energies are high enough to consider impossible any further hydrogenation. No other path for COH formation was found resulting in a lack of catalytic activity not substrate but reactant dependent.

However this study helps to shed light on the reaction mechanism for methanol synthesis on Au/TiC. Our previous results about the water gas shift reaction (WGS) on Au/TiC, where CO_2 and molecular hydrogen are formed from carbon monoxide and water, pointed out the carboxyl mechanism as the most favourable despite of the redox one, involving the partial dissociation of water followed by the oxidation of CO and the formation of carboxyl. However none was anticipated about the formation mechanism of the methanol detected in the experiments. It can in principle come from subsequent reductions and dissociation of some CO_2 hydrogenation intermediates or from direct carbon monoxide hydrogenation. Considering these last theoretical results this second hypothesis can be definitely discarded.

References

1 G. G. Asara, J. M. Ricart, J. A. Rodriguez, F. Illas, in preparation

2 J. A. Rodriguez, J. Evans, L. Feria, A. B. Vidal, P. Liu, K. Nakamura, F. Illas, J. Catal., 2013, 307, 162.

3 E. Florez, T. Gomez, P. Liu, J. A. Rodriguez, F. Illas, ChemCatChem, 2010, 2, 1219.

4 G. G. Asara, L. Feria, E. Florez, J. M. Ricart, P. Liu, J. A. Rodriguez, F. Illas, J. Phys. Chem. C, 2011, 115, 22495.

Unraveling of the unique pathway of CO_2 reduction on novel Au-TiC catalyst.

Gian Giacomo Asara,[a,b] Josep M. Ricart,[a] Jose A. Rodriguez,[c] Francesc Illas[b]

[a] Departament de Química Física i Inorgànica, Universitat Rovira i Virgili, C/ Marcel·lí Domingo s/n, 43007 Tarragona, Spain
[b] Departament de Química Física & IQTCUB, Universitat de Barcelona, C/ Martí i Franquès 1, 08028 Barcelona, Spain
[c] Chemistry Department, Brookhaven National Laboratory Upton, NY 11973 (USA)

Introduction

CO_2 hydrogenation helps to reduce the high quantities of this extremely pollutant gas emitted every year by human activities and obtain compounds that can be further used as chemicals to produce fuels and alcohols. This is a new, cheap and *green* source of C_1 molecules triggering the latest researches for catalysts that overpasses the nowadays "traditional" coinage metals supported by transition metals and transition metal oxides. A new type of catalyst that showed promising applications is formed by gold nanoparticles supported by transition metal carbides (TMC). From the capital work of Haruta[1] showing the surprisingly high catalytic activity of gold nanoparticles smaller than 10 nm despite the lack of reactivity of the bulk material, a huge number of theoretical and experimental studies arise, investigating activity towards various industrially relevant reactions and size-tunable properties.[2,3,4,5] These studies showed what influence chemical activity, how the structural flexibility plays a very important role in the stabilization of reaction intermediates[6] and demonstrating that it is a common feature of gold nanoparticles in spite of their dimensions.[7] Since the 1970's it is well known that *early* TMC have noble-metal-like properties and shows reactivity similar to Pt, Ru or Rh.[8,9] Many TMC form the same reaction intermediates found on noble metals surfaces, that differs from those found on the parent transition metal surfaces.[10] Their peculiar structural and electronic properties have been studied extensively[11] pointing out the important charge transfer from the metal to the carbon atoms. Also recent studies demonstrated decomposition of ammonia on Mo_2C[12] and on the same carbide hydrogenation of CO was also studied[13]. Catalysts made of metal monolayers supported by TMC substrates have been also explored as a possibility to reduce the amount of

expensive noble metals used. Deposition on TMC enhances the catalyst activity if compared with other supports.[9] Between all possible TMC combinations titanium carbide shows good qualities as support for gold nanoparticles and as catalyst in a variety of reactions.[14,15] Theoretical studies demonstrated how the Au-TiC interaction produces a charge polarization from the support to the nanoparticle that enhances the activity toward the dissociation of small molecules such as H_2, O_2 and SO_2.[16,17,18] Many studies concentrated on the description of the electronic and structural properties of the bulk material, the stability of low index surfaces, the adsorption of atoms and small molecules and reactivity.[11,19,20,21,22,23] From all stated above the composed Au-TiC system is a promising catalyst for CO_2 hydrogenation and in fact a recent study showed how Au-TiC outperforms industrial Cu/ZnO catalyst (under the same experimental conditions) in the synthesis of methanol. State-of-the-art DFT calculations and experiments on single crystals showed that CO_2 is activated after adsorption on the Au-TiC catalyst and that methanol production increases if substituting gold with copper.[24] Later, new experimental and theoretical results highlighted that nanoparticles ability to adsorb and activate CO_2 is sensitive to the noble metal atoms coordination demonstrating that low coordinated atoms increase the catalytic activity of small nanoparticles and one-atom thick clusters adsorbed on the carbide are extremely reactive.[25] This means that the activity is related with the fraction of gold atoms subjected to a strong polarization of its charge density by the support and that small flat nanoparticles are more active that big three dimensional ones. The work identified HOCO as key intermediate in the mechanism for CO_2 reduction to methanol on the Au-TiC system, leaving the open question if methanol was generated from witch of the two traditionally accepted pathways, the hydrogenation of CO generated by reverse water gas shift reaction (RWGS), or the reduction of the formate (HCOO) obtained from HOCO isomerization, or from both.

Analyzing in detail the reaction mechanism of CO hydrogenation on the Au-TiC model catalyst it will be shown that it is possible to exclude the RWGS pathway, pointing out HCOO as the determinant intermediate in CO_2 reduction. Such information is useful to systematically improve the production of methanol or others reduced compounds stabilizing the HCOO species, increasing the effectiveness of the Au-TiC catalyst.

Computational Details

The theoretical results presented were obtained using the VASP package.[26,27] The exchange and correlation contribution to the total DF energy has been calculated using the PW91 form[28,29] of the generalized gradient approximation. Geometrical optimization of the adsorbate structures has been performed using conjugate gradient or Newton-Raphson algorithms until forces on every relaxed atom were smaller than 0.02 eV/Å, where the wavefunction convergence criteria used was 1 10^{-6} eV. The valence electron density has been expanded using a plane wave basis set with an associated maximum kinetic energy of 415 eV. Core electrons have been treated using the projected augmented wave (PAW) method of Bloch [[30]], as in the implementation of Kresse and Joubert.[31] A 3×3×1 **k** points mesh generated using the Monkhorst-Pack algorithm[32] has been used for numerical integration in the first Brillouin zone. The (001) surface of the material has been modeled using a 3(√2 × √2) supercell (72 TiC units plus the 4 or 6 gold atoms of the nanoparticle) constructed with 4 layers, the bottom two frozen to the optimize bulk parameter, 4.328 Å, and the upper two fully relaxed during the optimization together with gold atoms and adsorbates. The surface was separated by 10 Å vacuum from its images repeated along the z-axes avoiding self-interaction. This computational set up and the surface model was already used and described elsewhere22, and have shown to be enough accurate for the purpose of this work. The transition state (TS) structures initially guessed through the CI-NEB[33] method have been refined using the Dimer method[34] and verified by vibrational analysis. During the reaction the nature of adsorbates change together with the strength of the induced surface distortion. For this reason gold atoms where explicitly included in every TS search, and in some cases it was of crucial importance also include the upper layer of the slab. All adsorption energies reported are calculated as:

$$E_{ads} = E_{mol+surf} - E_{mol} - E_{surf}$$

Where $E_{mol+surf}$ refers to the total energy of the molecules adsorbed on the slab model, Emol is the sum of the total energies of the gas phase CO and H_2 molecules, and E_{surf} is the total energy of the relaxed surface. Within this formalism, stronger interactions result in more negative adsorption energy values.

Reactivity on the clean TiC (001) surface.

As stated above, exploring the hydrogenation of CO on the Au-TiC system will enable us to determine the unique pathway for CO_2 reduction. Firstly is important to determine the reactivity of the CO with the bare support because adsorption on (001) clean surface is preferred for low coverage[22] and the surface is already covered by atomic hydrogen that spills over from the nanoparticle,[16] so statistically hydrogenation occurs more probably on the surface of the support than on the nanoparticle. Carbon monoxide experiments an adsorption energy of -1.52 eV, calculated when the molecule interacts with a carbon atom of the surface. Dissociative adsorption of one hydrogen molecule brings the system 2.48 eV beyond the molecular desorption level. Previous studies demonstrated that atomic hydrogen diffuses freely on the surface and can react with species adsorbed. Nevertheless diffusion of CO to the closest Ti atom on TiC (001) is prevented by a very high energy barrier of 1.41 eV.

First hydrogenation of CO is often the rate limiting step in syngas reactivity on a variety of substrates, due to the high adsorption energy and stability of carbon monoxide, and reaction barriers are often higher than 1 eV.[35] The addition of the first hydrogen on the C atom of carbon monoxide is barely endothermic (+0.29 eV), but highly impeded by an activation energy of 1.92 eV. The reaction involves the coordination of the hydrogen by both surface Ti and C atoms, together with the formation of a Ti-O bond (see fig. 1). It was not found any pathway for hydrogen attach on the oxygen atom. The formation of COH is possible only through HCO isomerisation, but the process is endothermic with reaction energy of +0.85 eV and it is prevented by the extremely high energy barrier (2.91 eV).

The addition of the second hydrogen leading to surface HCOH is highly endothermic, and the system have to overcome an energy barrier of 1.38 eV, similar to that calculated for the same reaction on other materials, although the formation of the surface HCOH is favored respect to the gas phase reactants by -1.41 eV. The transition state, where the H atom interacts simultaneously with the oxygen atom of HCO and surface C (see Fig. 2), lies by 0.82 eV under the desorption limit.

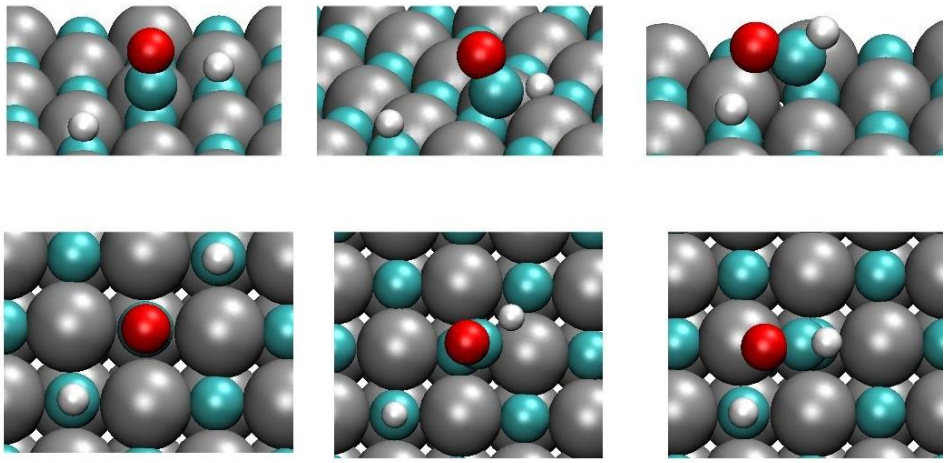

Figure 1 From left to right: reactants, transition state and product of the first hydrogenation of carbon monoxide [CO + H → HCO] on the clean (001) surface of TiC. Side and top view are sketched respectively in the upper and bottom part of the figure. Color legend: Ti (silver), C (cyan), O (red), H (white).

No transition state has been found for addition of the second hydrogen directly on the C atom. The hydrogenation of CO on the surface of the support is highly disfavored by both thermodynamics and kinetics, due to the high activation energies calculated for the attach of the first hydrogen to the endothermicity of the process, so the reaction will not proceed. However a small amount of HCOH will populate the surface, and at this point it is worth to ask if some valuable C_1 product can be obtained. For example HCOH can isomerize to formaldehyde (HCHO) forming the second C-H bond, and the process is exothermic by -0.1 eV.

However the energy barrier calculated is very high (1.84 eV) and the transition state structure, featuring a 3-term-ring (see Fig. 3)fig. SI 2), is unstable respect to gas phase molecular hydrogen and carbon monoxide by 0.44 eV.

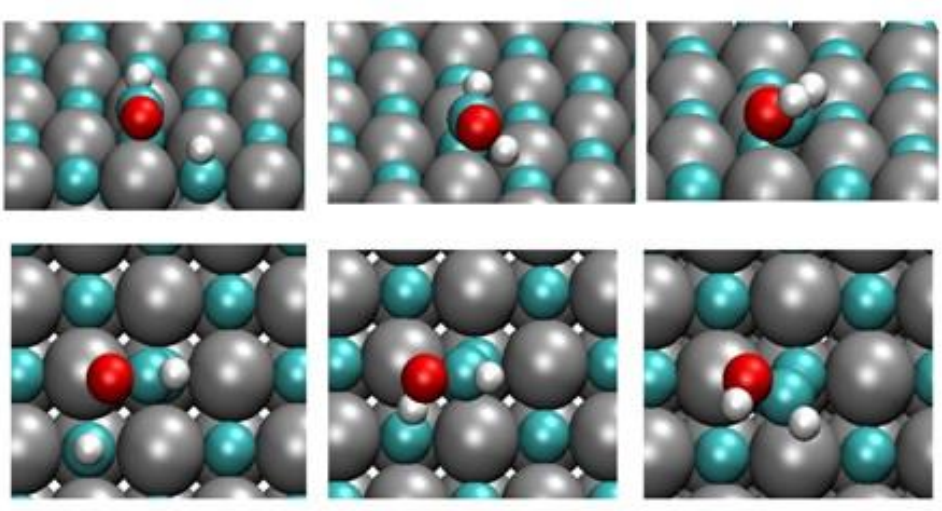

Figure 2: From left to right, reactants, transition state and product for the reaction: HCO + H → HCOH on the clean (001) surface of TiC. Side and top view are sketched respectively in the upper and bottom part of the figure. Colour legend: Ti(silver), C (cyan), O(red), H(white)

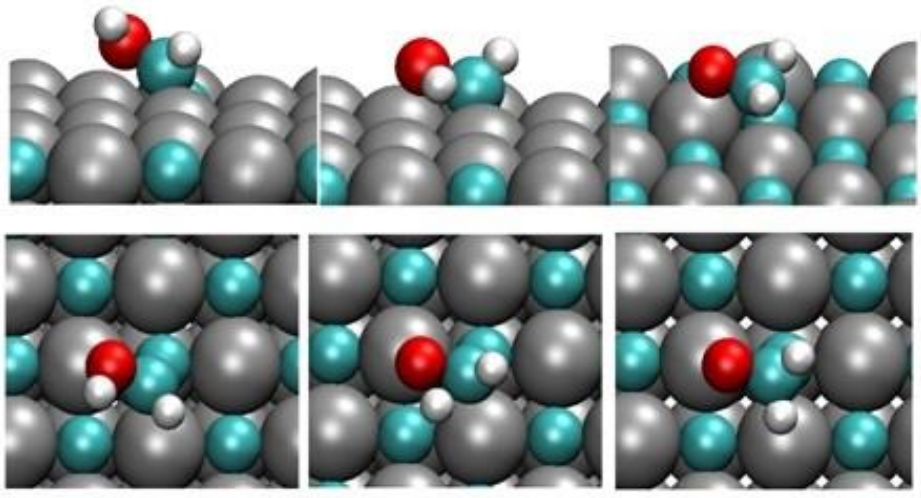

Figure 3: From left to right, reactants, transition state and product for the isomerization of HCOH to produce adsorbed formaldehyde (HCHO) on the clean (001) surface of TiC. Side and top view are sketched respectively in the upper and bottom part of the figure. Color legend: Ti (silver), C (cyan), O (red), H (white)

This means that, at this point, just a small part of the molecules will isomerize to formaldehyde, and the reaction will proceed backwards. Cleavage of C-O bond is necessary step for methane production. Dissociation of adsorbed CO (and HCO) to produce atomic oxygen and carbon (or O and CH units) is generally hindered by activation energy of few eV.[36,37] Experimental results on TiC (001) showed no methane production during CO_2 reduction, in agreement with the activation barrier of 2.99 eV calculated for CO direct dissociation and of 2.44 eV for HC-O bond cleavage. Methane production detected on nanopowders[38,39] can be interpreted as a direct consequence of surface roughness. On a kink site CO adsorbs strongly and the carbon atom substitutes the missing surface carbon. The oxygen interacts with a Ti atom present largely increasing the CO bond distance.[21] A graphical resume of the reaction network studied on the clean surface is reported in Fig. 4.

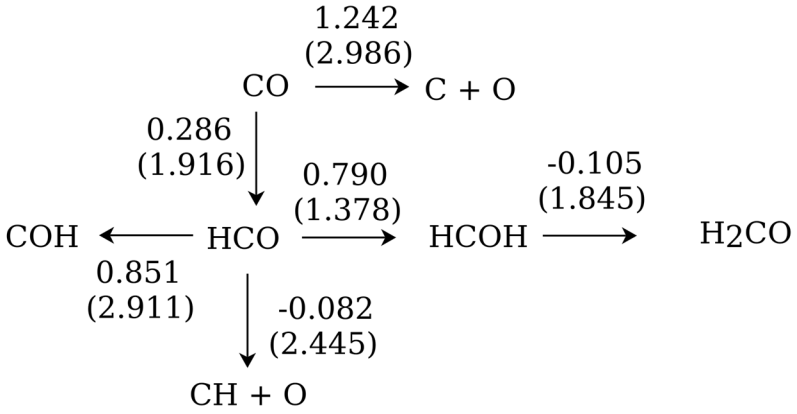

Figure 4: Calculated reactions network on the clean TiC (001) surface. In the model two adsorbed hydrogen atoms were explicitly included. Reaction energies (out of parenthesis) and activation barrier (in parenthesis) are reported in eV.

Reactivity on supported Au nanoparticles

We showed above that the contribution of the bare support to CO hydrogenation is negligible, so the contribution to the total methanol production has to come from the hydrogenation on top of the gold nanoparticles. Latest experiments on CO_2 reduction pointed out that the flat and small gold nanoparticles were more active than the 3-dimensional ones. In this study gold nanoparticles adsorbed on TiC (001) have been modeled with

two flat models of 4 and 6 atoms. The four atoms model has been widely used in previous investigations, predicting dissociation of hydrogen and activation of CO_2. Gold atoms are adsorbed on top of surface carbon showing a square shape, on top of witch hydrogenation can occur. We will focus on attach of the first hydrogen because it seem to be the rate determining step of the process. Let's consider the hydrogenation on the smaller Au_4 flat cluster: CO adsorbs with moderate strength (-1.32 eV), C down, on top of a gold atom.

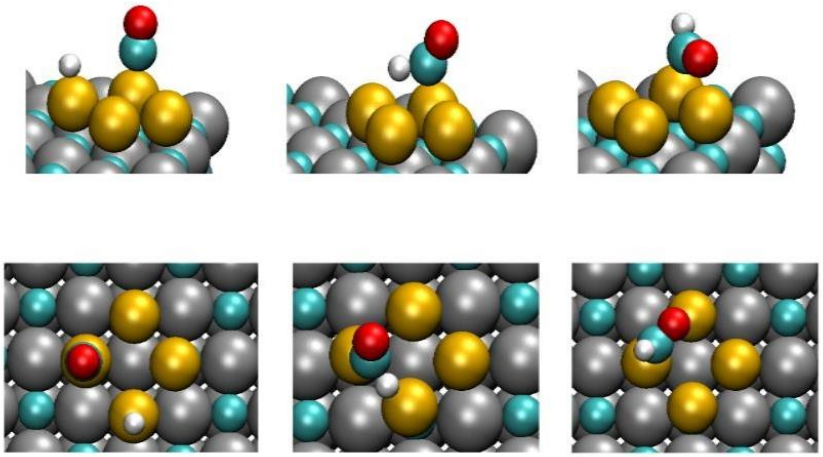

Figure 5: From left to right, reactants, transition state and product of the first hydrogenation of carbon monoxide [CO + H → HCO] on the smaller Au_4 nanoparticle model. Gold atoms are adsorbed on surface carbons in a 4-fold symmetry. Following the mechanism (i) (see text) hydrogen diffuses from a neighboring gold atom, approaching the carbon monoxide. In the transition state H coordinates both gold atoms, CO tilts and oxygen goes closer to the gold atom that will coordinate HCO. Hydrogen transfer and CO tilting occur on nearly-perpendicular planes. Color legend: Ti (silver), C (cyan), O (red), H (white), Au (gold).

Dissociative co-adsorption of H_2 brings the system -2.51 eV beyond the gas phase reactants (-2.46 eV if H and CO adsorb on first neighbors gold atoms, called Au and Au' – refer to the inset in fig 6 for a graphical explanation of this notation, that will be used throughout the following discussion). In this structure, atomic hydrogen directly interacts with one gold atom, where the other remains far from the gold cluster, adsorbed on a surface carbon. HCO formation on top of the cluster is not favorable, being endothermic by 0.66 eV. This means that the reduction on top of the Au4 cluster will be disfavored due to the endothermicity of the process, but still possible. When adsorbed in its

most favored geometry, C and O atoms of HCO interact with two first neighbor gold atoms. Using our model, it can occur with (at least) 3 mechanisms, (i) the migration of the hydrogen on the carbon of CO and the subsequent approach of the oxygen to another gold atom, (ii) the simultaneous migration of both CO and H on an empty first neighbor gold atom in between, or (iii) the diffusion of CO to a neighboring gold atom with subsequent insertion into the Au-H bond.

According with the neighbor notation presented in the inset of Fig. 6:

Mechanism (i) Au'-H + Au-CO → Au-HCO

Mechanism (ii) Au''-H + Au-CO → Au'-HCO

Mechanism (iii) Au'-H + Au-CO → Au'-HCO

Mechanism (ii) and (iii) are depicted in fig. 5. Mechanism (i) and (ii) require the movement of the reactants over two nearly-perpendicular planes impeding the reaction. Mechanism (iii) can be seen as a CO insertion in the Au-H bond. This is a usual mechanism in homogeneous catalysis, although in this case it requires the migration of carbon monoxide from a gold atom to another. In this case the movement of CO and the elongation of the Au-H bond occur along the same plane. Transition states for mechanism (i) have been identified, and characterized with just one imaginary frequency associated to the normal mode that brings the hydrogen atom from an Au' atom to the C atom of CO, that simultaneously tilts, approaching the oxygen to the other Au'. Structures of reactants, transition state and product involved in mechanism (i) are presented in Fig. 5. The energy barrier calculated is 1.93 eV, making this process largely disfavored but in principle possible because the transition state structure lies 0.54 eV beyond the desorption limit. No transition state has been identified for mechanism (ii), even if the co-planarity surely favours the process, nor for mechanism (iii), that implies the simultaneous movement of H and CO. It is possible that the CO migration is the factor that impedes the hydrogenation in both mechanisms. The lack of activity of the Au_4 cluster is possibly due to the high distorted structure of a feasible transition state, imposed by the cluster's 4-fold symmetry. To avoid this geometrical constrain a cluster composed by 6 gold atoms, adsorbed in two adjacent rows of surface carbons, has been constructed and optimized. The model now features 2 different kind of gold atoms, those in the corner and those in the edge of the cluster.

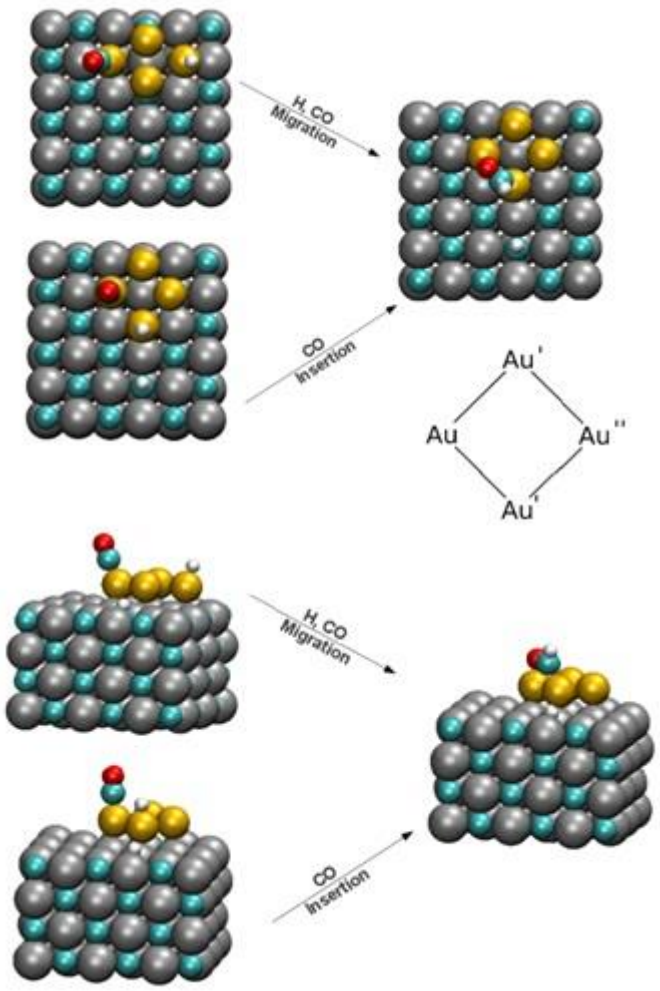

Figure 6: Representation of others possible pathways for the HCO formation on top of the Au_4 cluster model. Mechanisms (i) and (ii) impose a simultaneous movement of CO and H along two different, nearly perpendicular planes, reaching the final structure where the Au-C and Au-O interaction are both present. In the CO insertion -mechanism (iii) in the text- both interactions are produced through a coplanar movement of the reactants. Top and oblique view are reported in the upper and lower part of the figure, respectively. A schematic representation of the gold neighbors notation used in the text is presented in the inset. Colors legend: Ti (silver), C (cyan), O(red), H(white), Au (gold).

Although the difference with the Au_4 model can seem subtle, adsorbate geometry can vary considerably, together with reaction mechanism. On Au_6 HCO prefers to adsorb on an edge gold atom, with oxygen pointing outside of

the cluster. This means that reduction of CO adsorbed on a gold atom in the edge of the Au_6 cluster can occur easily through attach of hydrogen adsorbed on the other row. In this case, attach of hydrogen from behind and simultaneous tilting of CO out of the cluster will occur on the same plane. Reactants, transition state and product identified for the reduction on the Au_6 gold cluster are sketched in Fig 7. On this bigger cluster, the reaction is highly endothermic by 0.56 eV, with activation energy of 1.80 eV. This means that the Au_6 system is just slightly more active than the clean TiC (001) surface to reduce CO.

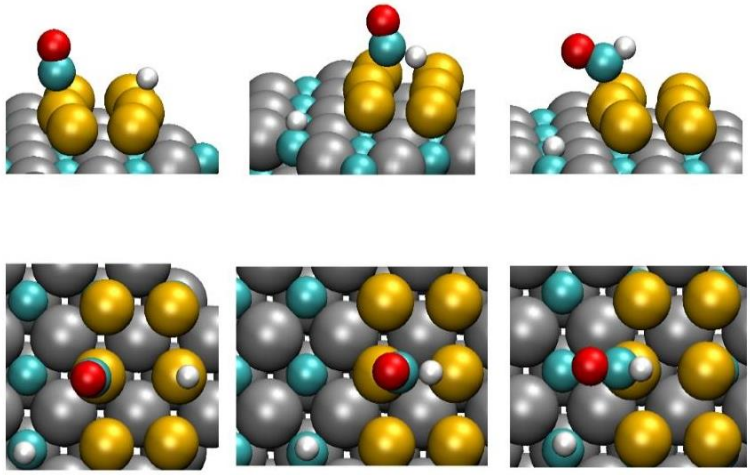

7 Figure 3: From left to right, reactants, transition state and product of the first hydrogenation of carbon monoxide [CO + H → HCO] on the bigger Au_6 nanoparticle model. Gold atoms are arranged in two rows, each atom directly interacting with a carbon of the surface. This geometry presents both edge and corner gold atoms, allowing a coplanar movement of reactants favoring the reaction. Color legend: Ti (silver), C (cyan), O (red), H (white), Au (gold).

The energy barrier decreases of about 0.12 eV respect to the clean surface and 0.13 eV respect to Au_4. These results together with experiments previously reported indicate the role played by HCOO in CO_2 reduction. The formate path for CO_2 reduction on the Au-TiC system can be now identified as the predominant (if not the only) process participating in methanol production. A comparative energy profile for the reaction of the three different substrates used is reported in Fig.8.

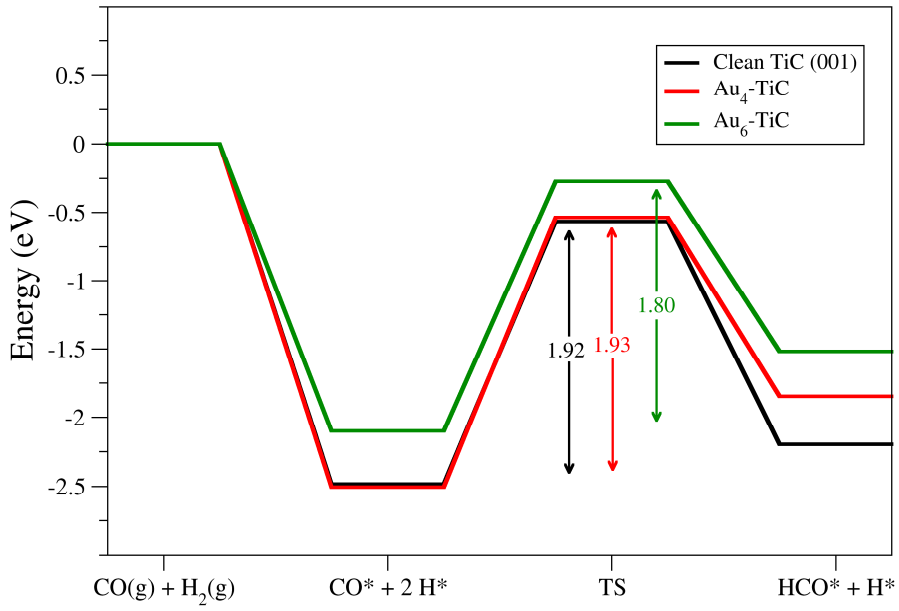

Figure 8: Comparative energy profile for attach of one hydrogen atom to CO on the clean TiC (001) surface and on the two models of gold nanoparticle used (Au_4 and Au_6). Arrows represent the heigh of the activation energy barrier. All energies are in eV.

Conclusions

Recent experimental studies indicated Au-TiC system as a promising candidate for the catalytic hydrogenation of CO_2 to methanol, highlighting how the highest activity was obtained when adsorbing small, flat, one atom thick nanoparticles. Production of CO (but no methane) was detected and DFT calculations identified HOCO as a key intermediate. Nothing was anticipated about the pathway followed during the hydrogenation but that it will follow the two traditionally accepted routes, the hydrogenation of CO generated by RWGS or the reduction of formate produced by HOCO isomerization. In this study the hydrogenation of CO has been studied in detail on the clean (001) surface, where CO prefers to adsorb, obtaining a high reaction barrier of 1.92 eV that prevent the reaction. Hydrogenation on top of Au_4 4-fold cluster occurs with a similar high activation barrier (1.93) probably due to the geometric constrain imposed by the 4-fold symmetry that does not allow a coplanar movement of the reactants. On the bigger Au_6 cluster the presence of both edge and corner atoms allows a

coplanar movement and calculated activation energy for attach of the first hydrogen is lower, but however extremely high. For this reason the quantity of methanol produced by this route will be negligible. The formate pathway can be considered positively as the predominant pathway involved in the methanol production from CO_2 on the Au-TiC model catalyst.

References

1 M. Haruta, N. Yamada, T. Kobayashi, S. Iijima, J. Catal., 1989, 115, 301.

2 M. Haruta, Catal. Today, 1997, 36, 153.

3 M. Valden, X. Lai, D. W. Goodman, Science, 1998, 281, 1647.

4 G. C. Bond, D. T. Thompson, Catal. Rev. Sci. Eng., 1999, 41, 319.

5 A. Sanchez, S. Abbet, U. Heiz, W. D. Schneider, H. Hakkinen, R. N. Barnett, U. Landman, J. Phys. Chem. A, 1999, 103, 9573.

6 H. Hakkinen, S. Abbet, A. Sanchez, U. Heiz, U. Landman, Angew. Chem. Int Ed., 2003, 42, 1297.

7 A. Vargas, G. Santarossa, M. Iannuzzi, A. Baiker, Phys. Rev. B, 2009, 80, 195421.

8 J. A. Rodriguez, F. Illas, Phys. Chem. Chem. Phys., 2012, 14, (2), 427.

9 T. G. Kelly, J. G. Chen, Chem. Soc. Rev., 2012, 41, 8021.

10 R. L. Guenard, L. C. Fernández-Torres, B.-I. Kim, S. S. Perry, P. Frantz, S. V. Didziulis, Surf. Sci., 2002, 515, 103.

11 F. Viñes, C. Sousa, P. Liu, J. A. Rodriguez, F. Illas, J. Chem. Phys., 2005, 122, 174709.

12 W. Zheng, T. P. Cotter, P. Kaghazchi, T. Jacob, B. Frank, K. Schlichte, W. Zhang, D. Sheng Su, F. Schüth, R. Schlögl, J. Amer. Chem. Soc., 2013, 135 (9), 3458.

13 H. Tominaga, Y. Aoki, M. Nagai, Appl. Cat. A: General, 2012, 192, 423.

14 F. Viñez, J. A. Rodriguez, P. Liu, F. Illas, J. Catal., 2008, 260, 103.

15 A. Vojvodic, Catal. Lett., 2012, 142, 728.

16 E. Florez, T. Gomez, P. Liu, J. A. Rodriguez, F. Illas, ChemCatChem., 2010, 2, 1219.

17 J. A. Rodriguez, L. Feria, T. Jirsak, Y. Takahashi, K. Nakamura, F. Illas, J. Am. Chem. Soc., 132, 2010, 3177.

18 J. A. Rodriguez, Liu P., Viñes F., Illas F., Takashi Y., Nakamura K., Angew. Chem. Int. Ed., 2008, 47, 6685.

19 P. Frantz, S. V. Didziulis, L. C. Fernandez-Torres, R. L. Guenard, S. S. Perry, J. Phys. Chem. B, 2002, 106, 6456.

20 S. V. Didziulis, H. I. Kim, J. Phys. Chem. C, 2007, 111, 11275.

21 B. Mant, G. G. Asara, J. A. Anderson, N. Homs, P. Ramirez de la Piscina, S. Rodriguez, J. M. Ricart, F. Illas, Surface Science, 2013, 613, 63.

22 G. G. Asara, L. Feria, E. Florez, J. M. Ricart, P. Liu, J. A. Rodriguez, F. Illas, J. Phys. Chem. C, 2011, 115, 22495.

23 A. Vojvodic, C. Ruberto, B. I. Lundqvist, J. Phys.: Condens. Matter, 2010, 22, 375504.

24 A. B. Vidal, L. Feria, J. Evans, Y. Takahashi, P. Liu, K. Nakamura, F. Illas, J. A. Rodriguez, J. Phys. Chem. Lett., 2012, 3, 2275.

25 J. A. Rodriguez, J. Evans, L. Feria, A. B. Vidal, P. Liu, K. Nakamura, F. Illas, J. Catal., 2013, 307, 162.

26 G. Kresse, J. Hafner, Phys. Rev. B, 1993, 47, 558.

27 G. Kresse, J. Furthmuller, Phys. Rev. B, 1996, 54, 11169.

28 J. P.Perdew, K. A. Jackson, M. R Pederson, D. J Singh, C. Fiolhais, Phys. Rev. B, 1992, 46, 6671.

29 J. P. Perdew, Y. Wang, Phys.Rev. B, 1992, 45, 244.

30 P. E. Blöchl, Phys. Rev. B, 1994, 50, 17953.

31 G. Kresse , D. Joubert, Phys. Rev. B, 1999, 59, 1758.

32 H. J. Monkhorst, Pack J. D., Phys. Rev. B, 1976, 13, 5188.

33 G. Henkelman, B. P. Uberuaga, H. Jónsson, J. Chem. Phys. 2000, 113, 9902.

34 G. Henkelman, H. Jónsson, J. Chem. Phys., 1999, 111, 15.

35 http://suncat.slac.stanford.edu/catapp/

36 Y. Choi, P. Liu, J. Am. Chem. Soc., 2009, 131, 13054.

37 I. N. Remediakis, F. Abild-Pedersen, J. K. Nørskov, J. Phys. Chem. B 2004, 108, 14535.

38 I. Kojima, E. Miyazaki, I. Yasumori, Chem. Comm, 1980, 12, 573.

39 I. Kojima, E. Mayazaki, J. Catal., 1984, 89, 168.

Chapter 6

Adsorption of coinage metals on δ-MoC

The previous chapters presented results obtained on titanium carbide studying structural properties, interaction with gold nanoparticles and the catalytic properties of the novel Au/TiC system. Now we will focus on another transition metal carbide, which shares important properties with TiC but have also crucial differences.

Investigation on molybdenum carbides begun long time ago[1] and are now triggered by new experiments exploring surface activity as well as their applicability as activating support for noble metals. Good results were obtained for hydrogenation of CO and CO_2 [2,,4] but also for processes such as C-C versus C-O scission,[5] water-gas shift reaction,[6] thiophene hydrodesulfurization and methane reforming among others.[7,8]

The plural used above to refer to molybdenum carbides was not casual. In fact various stable and metastable phases exist, such as orthorhombic, hexagonal and rock-salt cubic structures; the former two are found in Mo_2C and the latter corresponds to the stable phase for the MoC stoichiometry. Despite the orthorhombic phase (normally referred as β-Mo_2C) is generally considered as the most stable bulk phase recent theoretical studies predicted lowest cleavage energy for the (001) surface of δ-MoC.[9] Real catalyst nanoparticles are polycrystalline presenting a mix of phases where the cubic is definitely present. The (001) surface of δ-MoC then will be a non-negligible fraction of the surface exposed.

This chapter is focused on the interaction of Au, Cu and Ni noble metal atoms adsorbed on the (001) surface of the cubic δ-MoC. The theoretical results presented here have been obtained in collaboration between the Quantum Chemistry Group at the Universitat Rovira i Virgili, the Computational Materials Science Laboratory, CMSL, of the Universitat de Barcelona, and the Brookhaven

National Laboratory (BNL-USA). They have been published recently and are reported hereafter.[10]

The adsorption of single Au, Cu and Ni atoms is the first step when studying the interaction of bigger metal clusters with some support. It is useful because several properties are normally conserved for bigger clusters, for example preferred adsorption site, adsorption energy trends and direction and entity of the charge transfer between adsorbate and support (if present).

These elements were chosen because of their proved catalytic activity when adsorbed as atoms or small clusters on TMC surfaces.[11] Information about the interaction with MoC cubic phase also helps to rationalize common characteristics of all rock-salt cubic TMC, the majority of the carbides of groups IV-VI. Comparing the adsorption of the same elements on different rock-salt TMC it is possible to evaluate the effect of extra *d* electrons on structural properties or chemical activity of the composed noble metal – TMC system.

Firstly, the interaction of Au, Cu and Ni atoms was studied as a function of the coverage using supercell models of several sizes. We explored coverage ranging from 0.25 to 0.028 ML. The main difference between those models stays in the number of relaxed atoms explicitly included in the geometrical optimization. Higher coverage is reproduced using a smaller surface model and smaller is the number of relaxed degrees of freedom of the surface. It will be shown that this can lead in errors in both adsorption geometry and energies.

This work followed several systematic investigations on the interaction of noble metal atoms with the (001) surface of rock-salt TMC and how different substrates influence the catalytic activity of the composed noble metal – TMC catalyst.[12,13] Unfortunately those earlier works did not account for the in-plane relaxation but just for that along the direction perpendicular to the surface. In this way the principal effect that stabilizes the atom on the surface is lost.

The capability of the surface to accommodate the adsorbed metals and the strength of the interaction depends of the fraction of the sites occupied. For lower coverage the substrate can relax more and the area of the hollow sites where atoms adsorb increases up to ~25%. This fact results in a decrement of the perpendicular distance between the atom and the surface together with an increment of the strength of the interaction. The direction of the charge transfer between the surface and the adatom is always determined by the

electronegativity of the pure elements (i.e. adsorbed Cu and Ni become positively and Au negatively charged). For higher coverage the extent of the charge transfer decreases together with the shift of the *d*-band center to more positive energies getting closer to the Fermi level. This fact infers an increment in the catalytic activity, predicted to be in the order Ni > Cu > Au.

References

1 J. S. Lee, S. T. Oyama, M. Boudart, J. Catal., 1987, 106, 125.

2 A. J. Medford, A. Vojvodic, F. Studt, F. Abild-Pedersen, J K. Nørskov, J. Catal., 2012, 290, 108.

3 H. Tominaga, M. Nagai, Appl. Catal. A Gen., 2005, 282, 5.

4 M. D. Porosoff, X. Yang, J. A. Boscoboinik, J. G. Chen, Angew. Chem. Int. Ed., in press, DOI: 10.1002/anie.201404109

5 W. Yu, M. Salciccioli, K. Xiong, M. A. Barteau, D. G. Vlachos, J. G. Chen, ACS Catal., 2014, 4, 1409.

6 J. Patt, D. J. Moon, C. Phillips, L. Thompson, Catal. Lett., 2000, 65, 193.

7 H. Tominaga, M. Nagai, Appl. Catal. A Gen., 2008, 343, 95.

8 H. Tominaga, M. Nagai, Appl. Catal. A Gen., 2007, 328, 35.

9 J. R. Politi, F. Vines, J. A. Rodriguez, F. Illas, Phys. Chem. Chem. Phys, 2013, 15, 12617.

10 G. G. Asara, F. Vines, J.M. Ricart, J. A. Rodriguez, F. Illas, Surf. Sci., 2014, 624, 32.

11 J. A. Rodriguez, J. Evans, L. Feria, A. B. Vidal, P. Liu, K. Nakamura, F. Illas, J. Catal., 2013, 307, 162.

12 T. Gomez, E. Florez, J. A. Rodriguez, F. Illas, J. Phys. Chem. C, 2010, 114, 1622.

13 E. Florez, T. Gomez, J. A. Rodriguez, F. Illas, Phys. Chem. Chem. Phys ., 2011, 13, 6865.

Surface Science 624 (2014) 32–36

Contents lists available at ScienceDirect

Surface Science

journal homepage: www.elsevier.com/locate/susc

When reconstruction comes around: Ni, Cu, and Au adatoms on δ-MoC(001)

Gian Giacomo Asara [a,b], Francesc Viñes [b], Josep M. Ricart [a], José A. Rodriguez [c], Francesc Illas [b,*]

[a] Departament de Química Física i Inorgànica, Universitat Rovira i Virgili, C/Marcel lí Domingo s/n, 43007 Tarragona, Spain
[b] Departament de Química Física & IQTCUB, Universitat de Barcelona, C/Martí i Franquès 1, 08028 Barcelona, Spain
[c] Chemistry Department, Brookhaven National Laboratory, Upton, NY 11973, United States

ARTICLE INFO

Article history:
Received 4 November 2013
Accepted 23 January 2014
Available online 30 January 2014

Keywords:
Transition metal carbides
MoC
Metal-support
DFT

ABSTRACT

The interaction of Au, Cu, and Ni metal atoms with the δ-MoC(001) surface was studied using periodic density functional (*DF*) calculations to analyze adsorption energies and equilibrium geometries, work functions, atomic charges, projected density of states (*PDOS*), and shifts of the transition metal *d*-band center. The atomic adsorption is found to cause an in-plane distortion of the surface, and, besides, the interaction strength turns to be coverage dependent. A lower coverage allows for a better accommodation of the adsorbate, alongside causing a *d*-band center shift to more negative energies, as shown by plots of the PDOS. Regardless of the coverage, interaction strength diminishes following the order Ni > Cu > Au. Adatom chemical activity can be inferred based on the calculated *d*-band center; Ni being the most active metal, followed by Cu, and then Au for every coverage studied. This result well correlates with experiments on other transition metal carbides. Atomic adsorption also diminishes surface work function.

1. Introduction

The manifold technological applications of transition metal carbides (*TMC*) are nowadays well-known, and they have been the subject of several reviews in the last years [1,2]. For instance, such materials are currently widely used as cutting tools or covering materials, due to their extreme hardness. This feature and other important physical properties like their high electric conductivities and refractory melting temperatures have been interpreted by means of the analysis of the covalent, metallic, and ionic contributions to the chemical bonding between the transition metals and the carbon atoms [3]. From the early seventies, some other promising and more exciting possible uses of TMC captured the attention of the scientific community, including their usage as heterogeneous catalysts for industrial reactions: high activities have been found for both TMC single crystals and nanometric powders. In some cases, the TMC catalytic activity has been estimated to be higher than currently used industrial catalysts, as happened for the water gas shift reaction, where density functional (*DF*) calculations predicted that TiC(001) surface overtake the industrial Cu-based catalyst [4]. In the field of heterogeneous catalysis models, TMC has been explored as well as non-innocent supports for noble and coinage metal catalysts, but also as electrocatalysts in fuel cells [5]. For instance, metal clusters supported on TMC have been used for desulfurization ($DeSO_x$) reactions [6], hydrogenation of CO_2 to obtain methanol or methane [7], and also for oxidation reactions [8,9].

From earlier theoretical works it is found that the carbide–metal adatom interaction induces an important charge polarization in the latter [10–13], partially reducing the admetal and consequently boosting the activation of small organic or inorganic molecules adsorbed on the system [6–9,14–19]. Polarization of the electron density results in a charge accumulation in the proximity of the adsorbed transition metals, which is considered the key aspect in the enhanced catalytic activity of TMC-supported metal clusters [10]. This background is capitally important when designing new catalysts combining transition metals with TMC, together with the linear relation demonstrated among adsorption and activation energies [20]. In many cases simple computational models well-reproduced *in silico* experimental trends for adsorption energies, adsorbate geometries, and preferred adsorption sites, recovering the experimental data on the activity trends of various TMC–metal nanoparticles composite systems.

In this work we present a detailed analysis of the adsorption of single Au, Cu, and Ni atoms on the (001) surface of δ-MoC as carried out previously on a few metal–TMC combinations [10–13]. In these previous works several transition metals were tested on δ-MoC and similar carbides, such as TiC, yet only a high coverage situation was considered. Furthermore, surface relaxation was not properly taken into account, and, although hardness is a common and important feature of TMCs, it has been shown that adsorption can cause an important distortion of the surface, vital for a proper description of adsorptive processes, as found for the relaxation found when adsorbing CO on TiC(001) [21]. The choice of Ni, Cu, and Au transition metals is also motivated by recent theoretical and experimental work on CO_2 hydrogenation to methanol, catalyzed precisely by Au, Cu, and Ni supported on TiC(001) [6,19].

* Corresponding author.
E-mail address: francesc.illas@ub.edu (F. Illas).

0039-6028/$ – see front matter © 2014 Elsevier B.V. All rights reserved.
http://dx.doi.org/10.1016/j.susc.2014.01.015

Molybdenum carbides display interesting catalytic properties [2] which could be enhanced by the deposition of metals such as Ni, Cu, or Au [1]. Here it will be shown that surface reconstruction and in-plane relaxation happen to be determining when supporting metals on δ-MoC(001). In addition, adsorption energy trends and changes in surface properties such as work function or atomic charges have been identified, and connected to the most stable adsorption configurations. The single atom adsorption provides a first idea of the interactions of a certain metal to the carbide surface and, subsequently, how the support can affect the atoms in a larger cluster.

1.1. Computational details

Adsorption of Cu, Ni, and Au metal atoms has been studied using standard state-of-the-art periodic DF calculations. Four-layered slabs of δ-MoC were cut from the bulk perpendicular to the [001] direction and later on optimized. Atoms include in the uppermost 2 layers plus the adatom were fully allowed to relax whereas the two bottom layers were kept fixed at the previously optimized bulk positions [22]. Interaction between translationally repeated slabs was avoided adding 10 Å of vacuum along the [001] direction. Top image of the pristine relaxed surface is shown in Fig. 1. Note in passing that δ-MoC is a metastable phase compared to the hexagonal form. However, due to the high intrinsic stability of the (001) nonpolar surface, confirmed by its very low surface energy, it can be expected to be partially exposed.

Three different slab models have been used to represent diverse coverages. The smallest cell is a $(\sqrt{2}\times\sqrt{2})R45^\circ$ supercell exposing two Mo and two C surface atoms in a square arrangement, see Fig. 1. This latter cell has been renamed (1×1) for simplicity. The other two employed supercells for each surface are — following the above notation — (2×2) and (3×3) supercells. These permits one to scan metal coverages (θ) from 0.25 to 0.028. Following a previous computational strategy [22], we used the Perdew–Burke–Ernzerhof (*PBE*) exchange-correlation functional [23], given its suitability in describing molybdenum carbides. Calculations were carried out using the VASP computational package [24]. All calculations were carried out in a spin-polarized fashion. Valence electrons have been described using a plane-wave basis set with an associated maximum kinetic energy of 415 eV. The effect of the core electrons on the valence electron density was described using the Projector Augmented Wave (*PAW*) method [25]. The electron density was considered converged when subsequent energy minimization steps lead to a maximum difference of 10^{-6} eV. Similarly, structures were optimized until forces calculated on each relaxed atom were smaller than 0.02 eV $Å^{-1}$. For an accurate evaluation of the total energy of the system a Monkhorst–Pack k-point grid of $5\times5\times1$ was used for the sampling of the first Brillouin zone on all the employed supercells.

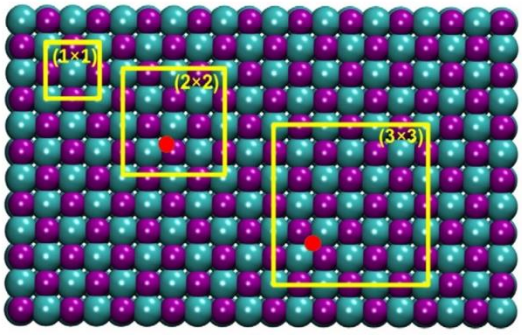

Fig. 1. Top view of the optimized (001) surface of δ-MoC. Yellow lines indicate the vectors of the supercell models used to study adsorption at various coverage θ. The $(\sqrt{2}\times\sqrt{2})R45^\circ$ cell, (1×1) in our notation, exposes 4 atoms in total, 2 Mo and 2 C and represents coverage $\theta=0.25$. (2×2) and (3×3) supercells represent $\theta=0.0625$ and $\theta=0.028$ and expose 16 and 36 atoms respectively. Mo and C atoms are represented by cyan and purple spheres, respectively. In (2×2) and (3×3) supercell sketches the red spots respectively indicate the MMC and Hollow adsorption sites.

The adsorption energy has been calculated as:

$$E_{ads} = E_{M/TMC} - E_M - E_{TMC} \quad (1)$$

where E_{ads} is the adsorption energy, $E_{M/TMC}$ is the energy of the supercell with the metal adatom, E_M is the energy of the metal atom in the vacuum, and, finally, E_{TMC} is the energy of the pristine carbide slab. Within this formalism, the more negative the E_{ads} values, the stronger the interaction. All stable structures have been identified as minima in the potential energy surface by numerical calculation of the Hessian matrix, obtained by finite displacements of the adatom coordinates. Note that a better characterization would include the coupling with the carbide surface atoms. Vacuum atomic energy references were gained by placing the metal atom in a large $9\times10\times11$ Å asymmetric box and calculating the total energy. Atomic charges for adatoms were estimated applying a Bader analysis [26]. The surface work function was calculated by subtracting the Fermi energy value of the system under study from the electron potential value in the vacuum region. The center of the *d*-band was obtained by plotting the projected density of states (*PDOS*) and numerically integrating the density in the *d*-band region of the total density of states (*DOS*).

2. Results

Let us begin with the clean δ-MoC(001) surface. One of its main features is the surface rumpling, a process mostly concerning the atoms of the outermost layer of a surface. Atomic relaxation changes the interplanar distance along the axis perpendicular to the surface, to a different extent for anions and cations. This process has been intensively studied in oxides [27] and in the (001) surface of rock-salt materials such as sodium halides [28], and it is found also in the (001) surface of early transition metals carbides [3]. For carbides, it implies an inward relaxation of the metal atoms at the surface, together with a displacement of the carbon atoms towards the vacuum. It is noteworthy that δ-MoC is the TMC where this effect is most pronounced. DFT calculations using PW91 [29] functional predicted an intralayer rumpling displacement of 0.24 Å (0.26 Å calculated at RPBE level) [3]. Recent calculations performed with the PBE functional confirm both results, with a calculated value of 0.25 Å. However, such relaxation does not imply any reconstruction, that is, the relative in-plane positions of the atoms and long range periodicity do not change. As it will be shown below, an important reconstruction occurs as a consequence of metal atoms adsorption.

Along this line we studied the adsorption of Ni, Cu, and Au atoms on the relaxed δ-MoC(001) surface. Due to its surface symmetry, see Fig. 1, six highly-symmetric adsorption sites have been explored; see previous studies for their definition and notation [30]. However, for these metals only two particular sites happen to be energetically competitive: The three-fold hollow site neighboring two surface Mo atoms and one surface C atom (MMC), and a four-fold hollow site, where metal adatoms are simultaneously bridging two Mo and two C surface atoms (Hollow). Energetic, geometric, and estimations of surface-related properties are encompassed in Table 1, connected to the most stable sites found for each particular case. The adsorption energies are of the same order as compared to other studies of metal adatoms on TiC(001) [13]. A comparison with bulk metal environments reveals that the bond strength of the studied metal atoms to the δ-MoC(001) surface is larger for Cu and Ni at lowest coverage, while at medium coverage it does only for Ni. In the case of Au, the Au–Au bonding is *a priori* stronger [31]. Thus, appearance of Au adatoms can only be feasible if aggregation is kinetically inhibited.

From previous studies [13] on similar surfaces, it is expected that Ni prefers to sit on top of surface C and both Cu and Au prefer MMC adsorption sites. Some of these results are confirmed at our highest coverage

Table 1
Summary of surface properties for Au, Cu, and Ni adatoms adsorbed on the (001) surface of δ-MoC at different coverages.

θ	0.028			0.0625			0.25		
	Ni	Cu	Au	Ni	Cu	Au	Ni	Cu	Au
E_{ads}/eV	−5.42	−3.58	*−2.98*	−4.75	−2.96	*−2.32*	−4.03	*−2.35*	*−2.04*
h/Å	1.32	1.47	*1.98*	1.34	1.51	*1.98*	1.491	*1.83*	*2.21*
A/Å^2	5.86	5.93	*5.93*	5.73	5.71	*5.65*	5.16	*4.86*	*4.90*
Q/e	0.19	0.22	*−0.18*	0.21	0.23	*−0.21*	0.24	*0.19*	*−0.13*
ϕ/eV	4.00	3.98	*3.97*	3.93	3.89	*3.92*	3.43	*3.56*	*3.88*

Adsorption energies (E_{ads}) and work functions (ϕ) are reported in eV; perpendicular distance to the surface (h) and adsorption area (A) are given in Å and Å^2, respectively. Atomic charges (Q) are reported in atomic units. Values in italics correspond to the MMC adsorption geometry, while regular font corresponds to hollow sites. Graphical explanation of adsorption area (A) and perpendicular distance (h) is reported in the inset of Fig. 2 for the particular case of Ni.

calculations, although some other values are in contradiction. It is noteworthy that Au atoms clearly prefer to sit on MMC sites regardless of the coverage, and so it happens for Ni atoms, yet on the hollow sites. At the fringe of both situations we find Cu, whose site occupation is a function of the coverage: At θ = 0.028 Cu clearly prefers to sit on hollow sites, and so does at medium coverage (θ = 0.0625) although at this latter coverage the MMC sites get closer in energy, with an E_{ads} of −2.75 eV, i.e. only 0.14 eV destabilized with respect to the hollow site. At the largest coverage explored (θ=0.25) the difference in energy between both sites is only 0.04 eV, and so they are considered isoenergetic situations, although further discussion centers on the hollow site, in order to get site-independent trends. The results for Ni contradict the earlier work in the sense that here top C adsorption site is disfavored at each studied coverage. Furthermore vibrational analysis showed that top C is only a proper minimum at high coverage, whereas at low and medium coverage it is a transition state associated to the atomic diffusion between two adjacent hollow sites.

It is worth to highlight that, regardless of the coverage and nature of the adsorbed atom, a significant in-plane reconstruction of the δ-MoC surface atoms is observed, quantified in an observed expansion of the hollow area (A), see Table 1 and sketch in Fig. 2 for a practical definition. Note that A has been calculated as $A = (d_{Mo} \cdot d_C) / 2$, where d_{Mo} and d_C are the distance between two surface Mo and or two surface C atoms, respectively. The sketch in Fig. 2 gives a practical visual definition for the hollow area A. Generally speaking, the adsorption of these metal atoms provokes a separation of surface Mo atoms involved in the adatom coordination, yet also on the surface C atoms, but to a lesser extent. As observed in Table 1 and Fig. 2, the atomic adsorption increases A up to ~25% at the lowest coverage treated. This adsorption-triggered deformation also involves neighboring unoccupied hollow sites, where such effect is present but more diluted. However, this medium-range perturbation is at the origin of the lower surface deformation found at (θ = 0.25) given that relaxations cancel with opposite forces of vicinal images. In any case, the stability of Ni, Cu, and Au metal adatoms on δ-MoC(001) is biased by the surface deformation, as shown in Fig. 2. The larger the allowed deformation, the stronger the bonding to the carbide surface.

One consequence of this is that the in-plane relaxation allows the adatoms to sensibly decrease the height (h) from the δ-MoC(001) surface, see Table 1, in perfect line with the featured stronger bonding. Nevertheless, note that the adsorption strength is also affected by the lateral repulsions between adatoms. To this end Bader charges (Q) have been obtained for the adsorbed atoms, and shown in Table 1. Regarding Au adsorption, calculated Bader charges are always negative, implying a MoC → Au charge transfer, as found for other TMCs [10]. The amount of charge transfer seems to slightly increase when decreasing the coverage, or, viewed from another perspective, the charge transfer is hindered at large coverages, given the repulsion of close negatively charged Au adatoms. Thus, at lowest coverage Au adatoms are more negatively charged. This feature is kept for Ni and Cu situations, although here the charge transfer is adatom → MoC, with an apparent increase of such transfer when increasing the coverage, a fact that

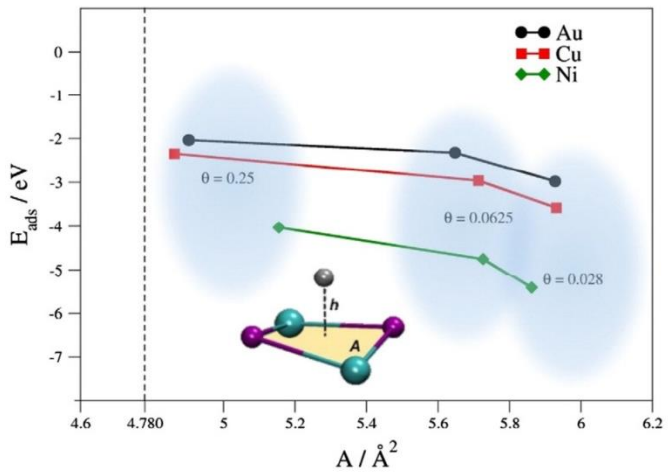

Fig. 2. Scatter diagram for calculated adsorption energies *versus* adsorption areas for each adsorbed metal atom in its most stable adsorption geometry. Vertical dashed line indicates the area of the relaxed naked surface. Graphical explanation of the adsorption area (A), in orange, and perpendicular distance from the surface (h, see Table 1) is reported in the inset for Ni atom, denoted by a gray sphere. Values for adsorption energies and areas are in eV and Å^2 respectively.

allows stating that electron-electron repulsion is governing lateral interactions of the metal adatoms. In any case such trends must be taken in caution since the variations with coverage are rather mild. Last but not least, it is worth to point out that the sign of the charge transfer seems to be intimately related with the transition metal atoms electronegativities. In this sense, the electronegativities of Cu and Ni are similar (1.90 Pauling units), lower than that of Mo (2.16). Au is a particular case which displays an exceptional large electronegativity of 2.55.

The surface charge rearrangement is largely affecting the computed work functions. Indeed, atomic adsorption seems to always lower the work function of the δ-MoC(001) surface, from previous estimations of ~4.4 eV for the naked surface [32] to present values ranging 3.4–4 eV, a feature that goes along with the above-commented electron density depletion when increasing the metal coverage. The variation of the work function induced by the presence of the adsorbate may seem counter intuitive since one normally relates positively/negatively charged adsorbates to decrease/increase the surface work function. However, it must be pointed out that these general trends are normally encountered in metallic surfaces with a highly polarizable conduction band whereas transition metal carbides have large covalent and ionic bonding contributions. Moreover, even in the case of metallic surfaces it is not always possible to relate the adsorbate charge with the change of work function. This was first pointed out by Petterson and Bagus for Cl on Cu(100) [33] and has been later discussed by Michaelides et al. [34] who have shown that a work function decrease induced by N adsorption on W(100) is consistent with a negative charge on N. In a more systematic work, Migani et al. [35] have also shown that the change on the surface work function induced by the presence of adsorbed chloride can be either positive or negative, depending on the surface metal. A recent analysis by Bagus et al. [36] extends these arguments to the case of I on Cu(111) and shows that negatively charged adsorbates can result in a decrease or increase of the surface work function. In any case, these simple charge redistributions arguments help in the understanding of the promising properties of transition metal carbides as supports for noble metal atoms in electrochemical catalytic applications [5], but also extend and recover recent results obtained on Mo_2C [37].

Last but not least, the adsorption energy trends are dependent on the coverage (and degree of surface reconstruction), but also, for any coverage, the bonding strengths decrease in the order $E_{ads}(Ni) > E_{ads}(Cu) > E_{ads}(Au)$. This trend seems to be intimately connected with the generated *d*-band center of the adsorbed metal atoms, as extracted from PDOS shown in Fig. 3, here defined as the center of mass of the projected *d*-orbitals of adsorbed metal atoms. For any of the studied metals the *d*-states shift to more negative energies when decreasing the coverage, coherent with a stronger interaction. Comparing the *d*-band center for the different metals, an approximated ranking of their catalytic activity can be extracted, as for every coverage studied the activity would decrease in the order Ni > Cu > Au, given that *d*-band centers are shifted towards Fermi level in the same order, i.e. *d*-band center of Ni is the least negative, and that of Au, the most. This last relation has been confirmed in ongoing experiments for the activation of methane on M/MoC surfaces (M = Ni, Cu or Au) [38] and such trend also agrees with data for CO_2 hydrogenation on M/TiC(001) [7].

The present results for the interaction of Au, Cu, and Ni with the δ-MoC(001) surface seem to point towards an intrinsic instability of the surface or to an intrinsic high reactivity. This is in agreement with experimental evidence that, up to now, it has not been possible to prepare a well-defined δ-MoC(001) surface. All experiments lead to polycrystalline samples, often with mixed MoC phases [39], which, in any case, include a non-negligible part of δ-MoC(001) surfaces. The shifts in the position of the C atoms of δ-MoC(001) induced by the admetals are important due to the fact that these C atoms are not simple spectators in the presence of C-containing

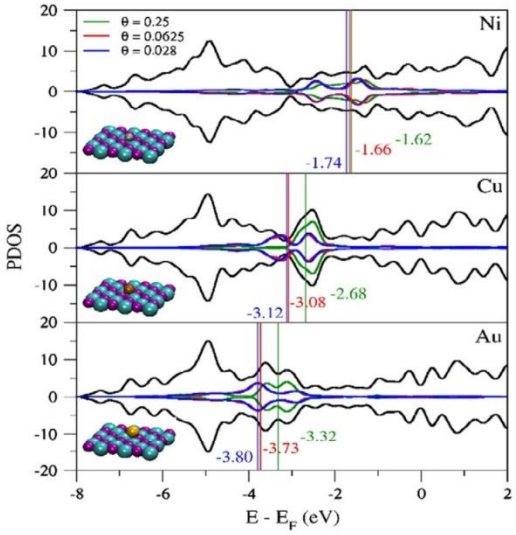

Fig. 3. Total DOS and PDOS at each coverage represented for each adatom adsorbed on its most stable geometry. Vertical colored lines represent the center of the *d*-band for each coverage, and the corresponding values are also reported nearby, in eV. On the left of each panel, eagle-eye view of the optimized structures at low coverage is also reported. Au, Cu, and Ni atoms are denoted as orange, red, and gray spheres, respectively.

adsorbates [7,39,33]. For instance they can make bonds with molecules such as CO or CO_2 and CH_x groups generated during the reforming of hydrocarbons [2,7,39,40], and previous studies point out that small molecules containing C and O atoms prefer a *mixed* anchorage where new C–C bonds including surface C atoms and metal–O bonds involving surface metal atoms are created [32].

3. Conclusions

A systematic DF study of the interaction between the Ni, Cu, and Au atoms and the non-polar (001) surface of δ-MoC has been performed at coverage θ with values ranging between 0.028 and 0.25, and a variety of surface properties such adsorption energies, equilibrium geometries, work functions, atomic charges, partial density of states and shifts of the transition metal *d*-band center have been analyzed.

Au (Ni) atoms show a clear preference for MMC (hollow) sites at any of the considered coverage, whereas Cu prefers to adsorb on hollow sites at low coverage while at MMC sites at high coverage. At medium coverage MMC and hollow geometries for Cu are essentially considered isoenergetic.

Ni, Cu, and Au atomic adsorption always causes a large in-plane deformation of the surface with an increment of up to ~25% of the underlying hollow area, also affecting neighboring hollow sites, although to a lesser extent. The ability to accommodate the adatom turns to be a function of θ, and increasing the coverage causes a reduction of the strength of the adsorbate–surface interaction.

An analysis of the PDOS shows how a higher atomic coverage produces a shift of the *d*-band to more positive energies, i.e. closer to Fermi level, in line with a decrease of the adsorption energy calculated. For every coverage, the calculated *d*-band center suggests that activity decreases in the order Ni > Cu > Au, a similar trend to that recently experimentally confirmed on CO_2 hydrogenation on other TMC [7], and, therefore, transferrable to the (001) surface of δ-MoC.

For all the coverage studied $E_{ads}(Ni) > E_{ads}(Cu) > E_{ads}(Au)$, i.e. adsorption causes a charge transfer MoC → adatom in the case of Au and adatom → MoC for Cu and Ni, but higher coverage affects all adsorbates quenching electronic charges. This result highlights how electron–electron repulsion governs lateral interactions of the metal adatoms. Finally, adsorption of all considered metals lowers the work function of the material passing from ~4.4 eV to ~4 eV.

Acknowledgements

This work was supported by the Spanish MICINN and MINECO (FIS2008-02238 and CTQ2012-30751 grants, respectively) and by *Generalitat de Catalunya* (grants 2009SGR1041 and XRQTC). G.G.A. thanks *Universitat Rovira i Virgili* for supporting his predoctoral research. F.V. thanks MINECO for a postdoctoral *Juan de la Cierva* grant (JCI-2010-06372). F.I. acknowledges additional support through the ICREA Academia award for excellence in research. J.A.R. is grateful for financial support by the US Department of Energy, Basic Energy Sciences Office (DE-AC02-98CH10886). Computational time at the *MARENOSTRUM* supercomputer has been generously provided by the Barcelona Supercomputing center.

References

[1] J.A. Rodriguez, F. Illas, Phys. Chem. Chem. Phys. 14 (2012) 427.
[2] T.G. Kelly, J.G. Chen, Chem. Soc. Rev. 41 (2012) 8021.
[3] F. Viñes, C. Sousa, P. Liu, J.A. Rodriguez, F. Illas, J. Chem. Phys. 122 (2005) 174709.
[4] F. Viñes, J.A. Rodriguez, P. Liu, F. Illas, J. Catal. 260 (2008) 103.
[5] A.L. Stottlemyer, T.G. Kelly, Q. Meng, J.G. Chen, Surf. Sci. Rep. 67 (2012) 201.
[6] J.A. Rodriguez, P. Liu, F. Viñes, F. Illas, Y. Takahashi, K. Nakamura, Angew. Chem. Int. Ed. 120 (2008) 6787.
[7] J.A. Rodriguez, J. Evans, L. Feria, A.B. Vidal, P. Liu, K. Nakamura, F. Illas, J. Catal. 307 (2013) 162.
[8] F. Viñes, C. Sousa, F. Illas, P. Liu, J.A. Rodriguez, J. Phys. Chem. C 111 (2007) 16982.
[9] Y.F. Zhang, F. Viñes, Y.J. Xu, Y. Li, J.Q. Li, F. Illas, J. Phys. Chem. B 110 (2006) 15454.
[10] J.A. Rodriguez, F. Viñes, F. Illas, P. Liu, Y. Takahashi, K. Nakamura, J. Chem. Phys. 127 (2007) 211102.
[11] E. Florez, F. Viñes, J.A. Rodriguez, F. Illas, J. Chem. Phys. 130 (2009) 244706.
[12] E. Florez, L. Feria, F. Viñes, J.A. Rodriguez, F. Illas, J. Phys. Chem. C 113 (2009) 19994.
[13] T. Gomez, E. Florez, J.A. Rodriguez, F. Illas, J. Phys. Chem. C 114 (2010) 1622.
[14] E. Florez, T. Gomez, J.A. Rodriguez, F. Illas, Phys. Chem. Chem. Phys. 13 (2011) 6865.
[15] T. Gomez, E. Florez, J.A. Rodriguez, F. Illas, J. Phys. Chem. C 115 (2011) 11666.
[16] J.A. Rodriguez, L. Feria, T. Jirsak, Y. Takahashi, K. Nakamura, F. Illas, J. Am. Chem. Soc. 132 (2010) 3177.
[17] E. Florez, T. Gomez, P. Liu, J.A. Rodriguez, F. Illas, ChemCatChem 2 (2010) 1219.
[18] L.K. Ono, B. Roldán-Cuenya, Catal. Lett. 113 (2007) 86.
[19] A.B. Vidal, L. Feria, J. Evans, Y. Takahashi, P. Liu, K. Nakamura, F. Illas, J. Phys. Chem. Lett. 3 (2012) 2275.
[20] F. Viñes, A. Vojvodic, F. Abild-Pedersen, F. Illas, J. Phys. Chem. C 117 (2013) 4168.
[21] G.G. Asara, L. Feria, E. Florez, J.M. Ricart, P. Liu, J.A. Rodriguez, F. Illas, J. Phys. Chem. C 115 (2011) 22495.
[22] J.R. Politi, F. Viñes, J.A. Rodriguez, F. Illas, Phys. Chem. Chem. Phys. 15 (2013) 12617.
[23] J.P. Perdew, K. Burke, M. Ernzerhof, Phys. Rev. Lett. 77 (1996) 3865.
[24] G. Kresse, J. Furthmüller, Phys. Rev. B 54 (1996) 11169.
[25] P.E. Blöch, Phys. Rev. B 50 (1994) 17953.
[26] R.F.W. Bader, Atoms in Molecules: A Quantum Theory, Oxford Science, Oxford, UK, 1990.
[27] J. Goniakowski, C. Noguera, Surf. Sci. 323 (1995) 129.
[28] S. Sawada, K. Nakamura, J. Phys. C Solid State Phys. 12 (1979) 1183.
[29] J. Perdew, J.A. Chevary, S.H. Vosko, K.A. Jackson, M.R. Pederson, D.J. Singh, C. Fiolhais, Phys. Rev. B 46 (1992) 6671.
[30] F. Viñes, C. Sousa, F. Illas, P. Liu, J.A. Rodriguez, J. Phys. Chem. C 111 (2007) 1307.
[31] P. Janthon, S.M. Kozlov, F. Viñes, J. Limtrakul, F. Illas, 9 (2013) 1631.
[32] S.V. Didziulis, K.D. Butcher, Coord. Chem. Rev. 257 (2013) 93.
[33] L.G.M. Pettersson, P.S. Bagus, Phys. Rev. Lett. 56 (1986) 500.
[34] A. Michaelides, P. Hu, M.-H. Lee, A. Alavi, D.A. King, Phys. Rev. Lett. 90 (2003) 246103.
[35] A. Migani, C. Sousa, F. Illas, Surf. Sci. 574 (2005) 297.
[36] P.S. Bagus, D. Käfer, G. Witte, C. Wöll, Phys. Rev. Lett. 100 (2008) 126101.
[37] D.V. Esposito, S.T. Hunt, Y.C. Kimmel, J.G. Chen, J. Am. Chem. Soc. 134 (2012) 3025.
[38] J.A. Rodriguez, work in progress.
[39] P. Liu, J.A. Rodriguez, T. Asakura, J. Gomes, K. Nakamura, J. Phys. Chem. B 109 (2009) 4575.
[40] J.A. Rodriguez, J. Dvorak, T. Jirsak, J. Phys. Chem. B 104 (2000) 11515.

Chapter 7

Reconstruction of the C-terminated β-Mo_2C (001) surface

The theoretical investigation presented in this chapter has been made in collaboration between our laboratory in the Universitat Rovira I Virgili, the Computational Material Science Laboratory of the Universitat de Barcelona, CMSL, the Brookhaven National Laboratory, BNL (USA) and the University College London, UCL (UK). Results obtained have been recently submitted for publication.[1]

In this chapter we have used periodic DFT calculations to predict and evaluate the stability of possible morphologies for the C terminated (001) surface of β-Mo_2C. New experimental and theoretical works pointed out the interesting catalytic activity of this material toward CO and CO_2 hydrogenation,[2,,4] methane reforming,[5,6] water-gas shift reaction,[7] thiophene hydrodesulfurization and C-C versus C-O scission.[8] The (001) surface of the β- phase is one of the most studied because of its stability, but also its intrinsic reactivity. Along the [001] crystallographic direction the material is made by alternated C or Mo layers and the simple bulk cut termination will present a finite dipole perpendicular to the surface, due to the different formal atomic charges of C and metal atoms. Following the classic concept developed by Tasker[9] such termination should undergo an important reconstruction that will minimise the mentioned dipole. This is true indeed for metal oxides, although the metallic character of TMC can help to reduce the perpendicular dipole stabilising the polar C terminated surface. Experimental determination of the C-terminated surface is however difficult because the electronic states in the proximity of the Fermi level belong to deeper Mo atoms, where the Mo terminated is highly reactive and after preparation reacts immediately.[10] DFT based calculations can shed light on the surface morphology with no additional bias but the accuracy of the theoretical methods used.

Various polar and non-polar reconstructions of the C-terminated β-Mo_2C (001) surface are analyzed including also the polar bulk-like termination. Non-polar reconstruction halves the number of C atoms in the upper layer of the slab and places it under the bottom layer, obtaining repetition units along (001) direction with no perpendicular dipole. We guessed then several possible motifs, or arrangements, for the surface C atoms of the upperlayer of the non-polar structures.

In all cases the calculated atomic charges are similar, suggesting an important ionicity despite of the metallic character of TMC. Work function also does not change sensibly indicating a similar electronic structure quite independent from the surface morphology. Structural analysis showed that polar surfaces suffer a reduction of the interlayer distance between the upper C layer and the metallic sublayer, where for non-polar surfaces the contraction involves all slab. Such local surface contraction helps reducing the dipole stabilizing the system.

The analysis of the calculated cleavage energy demonstrated that the non-polar C-terminated surfaces are always more stable and, for this reason, most probable. It is predicted by Boltzmann analysis that the non-polar surface represents the extended terminations seen under thermodynamic equilibrium. At low temperature the motif with lowest cleavage energy will be the only present but at higher temperature others non-polar motifs will be present, with a small but not negligible contribution of polar domains. Those motifs qualitatively reproduced the surface structures detected by older STM and LEED experiments.[11,12] For this reason we reproduced STM images for the most stable motifs. Our images nicely agree with the experiments and confirmed the important contribution of the Mo states to the valence band in the proximity of the Fermi energy.

References

1 G. G. Asara, A. Roldan, J. M. Ricart, J. A. Rodriguez, F. Illas, N. H. de Leeuw, submitted.

2 A. J. Medford, A. Vojvodic, F. Studt, F. Abild-Pedersen, J. K. Nørskov, J. Catal., 2012, 290, 108.

3 H. Tominaga, M. Nagai, Appl. Catal. A Gen., 2005, 282, 5.

4 M. D. Porosoff, X. Yang, J. A. Boscoboinik, J. G. Chen, Angew. Chem. Int. Ed., in press, DOI: 10.1002/anie.201404109

5 H. Tominaga, M. Nagai, Appl. Catal. A: Gen., 2008, 343, 95.

6 H. Tominaga, M. Nagai, Appl. Catal. A: Gen., 2007, 328, 35.

7 J. Patt, D. J. Moon, C. Phillips, L. Thompson, Catal. Lett., 2000, 65, 193.

8 W. Yu, M. Salciccioli, K. Xiong, M. A. Barteau, D. G. Vlachos, J. G. Chen, ACS Catal., 2014, 4, 1409.

9 P. W. Tasker, J. Phys. C: Solid State Phys., 1979, 12, 4977.

10 P. Liu, J. A. Rodriguez, T. Asakura, J. Gomes, K. Nakamura, J. Phys. Chem. B, 2005, 109, 4575.

11 K. Fukui, R.-L. Lo, S. Otani, Y. Iwasawa, Chem. Phys. Lett., 2000, 325, 275.

12 R.-L. Lo, K. Fukui, S. Otani, S.T. Oyama, Y. Iwasawa, Jpn. J. Appl. Phys., 1999, 38, 3813.

New insights into the structure of the C-terminated β-Mo_2C (001) surface from first principles calculations

Gian Giacomo Asara,[a,b,c] Alberto Roldan,[a] Josep M. Ricart,[b] Jose A. Rodriguez,[d] Francesc Illas,[c] Nora H. de Leeuw[a]

[a] Department of Chemistry and the Thomas Young Centre for the Theory and Simulation of Materials, University College London, 20 Gordon Street, London WC1H 0AJ
[b] Departament de Química Física i Inorgànica, Universitat Rovira i Virgili, C/ Marcel·lí Domingo s/n, 43007 Tarragona, Spain
[c] Departament de Química Física & IQTCUB, Universitat de Barcelona, C/Martí i Franquès 1, 08028 Barcelona, Spain
[d] Chemistry Department, Brookhaven National Laboratory, Upton, New York 11973

Abstract

Periodic density functional theory (DFT) calculations have been used to study the stability of five different C-terminations of the Mo_2C(001) surface in the most stable orthorhombic (β) phase of this important material. The different terminations all have similar values of the work function or atomic charges, indicating a similar electronic structure, although the analysis of the cleavage energy suggests that the non-polar C-terminated surfaces will be the extended terminations seen under thermodynamic equilibrium. Nevertheless, the calculated DFT cleavage energy values together with statistical arguments indicate that different C-terminated motifs are likely to co-exist even at temperatures just below annealing conditions.

Reconstruction of C-terminated β-Mo_2C (001) surface

Introduction

The catalytic properties of molybdenum carbides have been of interest to researchers for a considerable time[1] but more recently these materials have experienced renewed interest after a number of experiments explored their surface activities towards processes such as CO and CO_2 hydrogenation,[2-4] C-C versus C-O scission,[5] water-gas shift reaction,[6] thiophene hydrodesolfurization, and methane reforming.[7,8] Following previous work that systematically explored the activation of metal nanoparticles supported on *early* transition metal carbides towards molecular O_2 and H_2 dissociation[9,10] or SO_2 decomposition[11,12] (see also ref 13 and references therein), new experimental[8] and theoretical[14] studies employed Mo_2C as an active support for noble metal catalysts.

Molybdenum carbide has various stable and metastable phases such as orthorhombic, hexagonal and rock-salt cubic structures; the former two are found in Mo_2C and the latter corresponds to the stable phase for the MoC stoichiometry. The orthorhombic phase (normally referred as β-Mo_2C) is generally considered as the most stable. Particularly, detailed theoretical studies exploring the stability of the different β-Mo_2C surfaces, have identified that the β-Mo_2C(001) is the most stable surface.[15] Along the [001] direction, the material is made up of alternating carbon and metal layers, allowing two different terminations of either Mo or C; the latter was predicted to be the more stable and consequentially the most common surface.[15,16] The Mo–terminated surface has also been prepared, characterised and used in several experimental works in the past years showing high reactivity,[17] which is frequently attributed to a high surface energy caused by the exposure of Mo atoms with a relatively low coordination number. On the other hand, the C–terminated surface always displayed a less defined structure with the resulting structure strongly dependent on the methodology and temperature of preparation.[18-21] Such intrinsic instability can be ascribed to the inherent polarity

of the (001) surface since Mo_2C exhibits a large degree of ionic bonding character with calculated net charges on the C atoms of approximately -2 (see Table 1) [16] Extending the classic concepts developed by Tasker to estimate the stability of metal oxide surfaces[22] to transition metal carbides, the β-Mo_2C bulk cut through the (001) plane is classified as a type III surface. Hence, once the surface is generated, for instance by sputtering, an atomic rearrangement takes place to avoid the polarity perpendicular to the surface plane leading to other terminations with lower surface energy; one of the possible surface reconstructions is shown in Figure 1. Indeed, this type of surface reconstruction agrees well with findings arising from low energy electron diffraction (LEED) and scanning tunnelling microscopy (STM) experiments, where the bulk-truncated structure is always reconstructed but also depends on the stoichiometry of the surface,[19] namely on the carbon coverage.

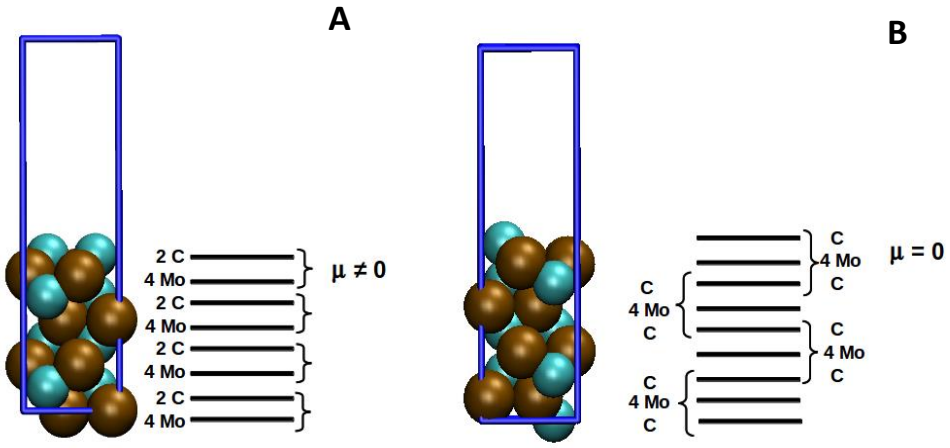

Figure 1. Schematic representation of β-Mo_2C(001) C-terminated, extending the classifications of Tasker to transition metal carbides. (A) is the bulk-cut surface, classified as type III following Tasker notation, and (B) is one possible surface reconstruction to avoid the perpendicular surface dipole μ. Colour code: cyan spheres are C atoms and brown spheres are Mo atoms.

In the present work we report a systematic study aimed at predicting the stability of various atomic rearrangements of the C-terminated β-Mo_2C(001)

surface. In addition to the arguments arising solely from calculated energy values, which do not take into account temperature effects, we also estimate the presence of each motif as a function of the temperature by a derived Boltzmann distribution based on the computed energies.

Methodology and Computational Details

A systematic study of several β-Mo_2C(001) surface terminations was carried out by means of calculations based on the periodic density functional theory (DFT). In these calculations, the effect of the core electrons on the valence electron density was taken into account through the projector augmented wave (PAW) method,[23] whereas exchange-correlation effects were included by means of a generalized gradient approximation (GGA) potential.[24] Thus, the Perdew–Burke–Ernzerhof (PBE) functional flavor was used to obtain the total energy of the system.[25] The valence electron density was expanded in a plane-wave basis set whose associated kinetic energy did not exceed a value of 415 eV. Numerical integration in the reciprocal space was achieved using a Monkhorst–Pack 5×5×1 k-point grid.[26] Electronic energy convergence better than 10^{-6} eV was always reached and the interatomic forces were minimized up to 0.02 eV/Å for structural relaxation calculations. This computational set up was recently shown to be sufficiently accurate for the purpose of this work.[16] All calculations were carried out employing the Vienna ab-initio simulation package (VASP).[27]

First, the bulk lattice of the orthorhombic phase (β-Mo_2C) was optimized, leading to cell parameters of 4.7430, 5.2293 and 6.0623 Å for a, b and c, respectively, in agreement with experimental values.[28] A surface slab model for the polar surface termination was then generated by directly cutting from the bulk through the (001) plane, whereas a model for the non-polar surface was obtained using the METADISE code.[29] In addition, three other motifs were prepared by reconstructing the top atomic layer of the surface supercell; hence,

a total of five different surfaces were considered. These surfaces were modelled by slabs, each containing 8 atomic layers and a 12 Å vacuum width perpendicular to the surface. We have tested both the slab thickness and the vacuum gap to ensure that the centre of the slab behaves as the β-Mo_2C bulk. Figure 2 shows that the centre of the slab does not change when all layers are fully relaxed. Furthermore, the system energy does not change by increasing the vacuum gap between slabs, indicating negligible interaction between the repeated slabs. Therefore, in the rest of calculations, the top 4 atomic layers were allowed to relax without symmetry restrictions until the atoms reached the required accuracy in the forces, whereas the rest of the layers were kept fixed at the bulk geometry.

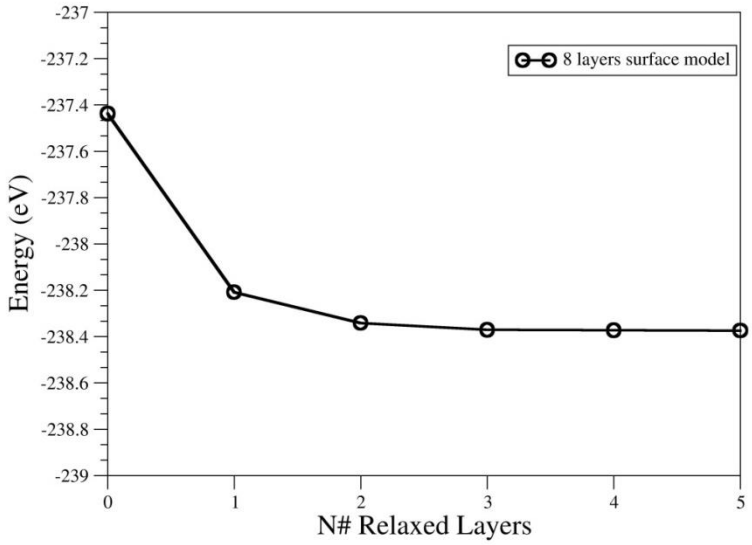

Figure 2. Total energy of the 8 layer polar C-terminated slab *versus* the number of layers relaxed during the geometrical optimisation. The total energy of the system is not influenced by the relaxation of the most internal layers, acting as bulk material. The perfect (unrelaxed) bulk-cut slab is also reported as 0 relaxed layers.

Surface Reconstructions

Various non-polar reconstructions of the C-terminated β-Mo_2C (001) surface are analysed with the polar bulk-like termination included for completeness. Note, however, that because of the particular electronic structure of this material, a bulk-like termination might not necessarily imply a permanent dipole perpendicular to the surface. For instance, the Mo-terminated bulk-like structure is known to be stable, a result arising from the large metallic character of the Mo top-layer. Nevertheless, the underlying carbide confers to the material a particular reactivity, quite different from that of bulk Mo surfaces.

The C-terminated bulk polar surface, hereafter referred to as *C-polar*, presents zig-zag stripes of carbon atoms occupying three-fold hollow sites formed by the underlying Mo layer. The reconstruction of this polar termination, hereafter called *C-polar Reconstructed* consists of moving half of the C atoms in the top surface away from the carbon stripes to the adjacent three-fold hollow sites, creating a new diamond-like motif which is clearly seen in Figure 3. The dipole perpendicular to the surface disappears by halving the number of surface C atoms and placing them in their corresponding bulk-like position at the frozen surface at the bottom of the slab.[22] Due to the geometrical equivalence of the C atoms, the C-terminated surface does not depend on the rearranged atoms. Note also that the *C-non-polar* reconstructed surface presents one surface carbon atom per (1×1) unit cell only (Figure 3). Additional non-polar reconstructions can be constructed using a (2×2) supercell instead. The surface motifs thus created are referred to as *Hexagonal* and *Stripes* and are obtained by sliding along different directions two of the four surface carbons explicitly included in the supercell model. The hexagonal termination shows a slightly distorted C-centred honeycomb structure, while the second reconstruction creates zig-zag stripes similar to the C-polar but misaligned with respect to

those of the carbon layers below. A schematic representation of each surface termination is reported in Figure 3.

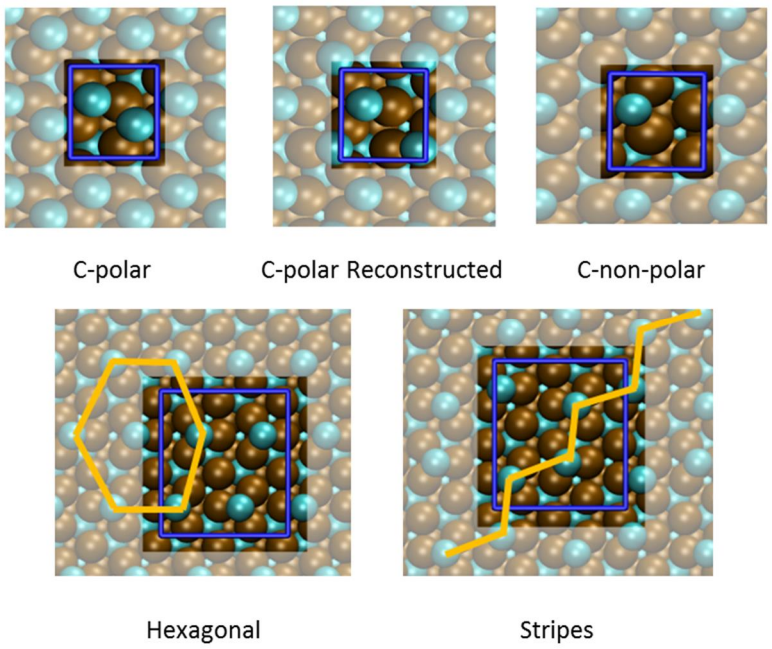

Figure 3: Representation of the different reconstructions of the β-Mo_2C(001) surface. Both polar and non-polar C- terminations are shown. Hexagonal and stripes periodicity are highlighted with yellow lines. The bottom side of the C-polar and C-polar-Reconstructed slab exposes the Mo-terminated surface, where for non-polar reconstructions the bottom of the slab presents always the C-non-polar morphology. Colour code: Cyan smaller spheres are C atoms and brown bigger spheres are Mo atoms. We displayed the cell in dark blue.

It is also important to note that these surfaces have different numbers of surface carbon atoms, and it is therefore logical to assume that carbon coverage resulting from a given preparation method will have a key role in defining the surface structure. In fact, it has been reported that a surface coverage increase from 0.33 ML to 0.5 ML leads to a reconstruction from honeycomb to zigzag structure.[19]

In order to determine the surface stability of different surfaces one would normally rely on the calculated surface energy γ^R obtained as

$$\gamma^U = \frac{E^U_{slab} - nE_{bulk}}{2A} \quad (1)$$

$$\gamma^R = \frac{E^R_{slab} - nE_{bulk}}{A} - \gamma^U \quad (2)$$

where γ^U is the surface energy of the unrelaxed surface model, i.e. using the energy obtained by maintaining the atomic structure at bulk-optimized positions denoted as E^U_{slab}; γ^R is the surface energy of the slab model with the topmost atomic layers relaxed as indicated above, obtained from the corresponding E^R_{slab} energy value; *n* stands for the number of bulk Mo_2C structural units and, finally, *A* is the exposed surface area per unit cell. Unfortunately, the above definition does not apply when the surfaces generated by cleaving the bulk are different, as in the case of the β-Mo_2C (001) where cleavage results in one C- and one Mo-terminated surface. In this situation the stability order of the reconstructed surfaces can be defined from the calculated cleavage energy E_{cleav}, which is simply the energy required to cleave the material in such a way that two different surfaces are exposed, one at the top of the slab and one at the bottom. To obtain E_{cleav} we use a two-step approach where the cleavage energy of the unrelaxed surface is first obtained as

$$E^U_{cleav} = \frac{E^U_{slab} - nE_{bulk}}{A} \quad (3)$$

and, in a second step, the surface of interest (*i*) is relaxed which leads to

$$E^{R_i}_{cleav} = E^U_{cleav} - E^i_{relax} = E^U_{cleav} - \frac{E^U_{slab} - E^{R_i}_{slab}}{A} \quad (4)$$

where $E^{R_i}_{slab}$ is the energy of the slab with the *i* surface termination (*i* = C-terminated or Mo-terminated) relaxed and the bottom layers kept fixed in the

bulk optimised positions. In this work, *i* refers to the C-terminated surface. To obtain the cleavage energy one needs to apply Equation 4 to the case where the Mo-terminated surface is relaxed and then average the two $E_{cleav}^{R_i}$ values. An alternative approach consists in fully relaxing the two surfaces simultaneously with the C-terminated in the desired reconstruction. For a sufficiently thick slab model, the two procedures should provide the same values. The latter approach has already been used before,[16] and test calculations carried out in the present work showed that E_{cleav} calculated by fully relaxing the 8 layer slab and subtracting the energy of the corresponding Mo_2C bulk units differs by only ± 0.02 J m^{-2} from the value calculated using the two step approach. This approach is thus an accurate method for obtaining the cleavage energy, especially as we are primarily interested in the relative stabilities of the different C-terminations. In Table 1 we therefore report the computed cleavage energies without taking into account the relaxation of the Mo-terminated side of the slab. We have also calculated the surface reconstruction amount expressed as in Eq. 5.

$$\%relax = \frac{E_{cleav}^{U} - E_{cleav}^{R_i}}{E_{cleav}^{U}} \quad (5)$$

Structure and relative stability of the reconstructed surfaces

The atomic structure of the different terminations described above has been optimized until full convergence and the calculated surface properties summarised in Tables 1 and 2. For bulk-like and reconstructed polar terminations, we found a uppermost C–C distance of ~3.1 and ~4.5 Å respectively. C-polar reconstructed shows a diamond-like motif. On the C-non-polar slab, C atoms are 5.2 and 6.1 Å far apart, whereas for the Hexagonal and Stripes reconstructions the situation is slightly more complex. In the Hexagonal reconstruction, each C is surrounded by six other atoms, two at 5.2 Å, two at 6.4 Å and two at 6.9 Å, forming a distorted carbon-centred hexagon. We also found peculiar structural features on the Stripes reconstruction termination, the C-C

intra-stripe distance is 4.7 Å, with the angle formed by three carbons at 117 °, and the *inter*-stripe distance is equal to 6.2 Å. The C-non-polar and the Stripes slab showed C-C distances very close to those experimentally reported, 6.03±0.02 Å.[20] Another structural difference among C-terminations is the contraction of the interlayer spacing in the relaxed layers. It is worth noting that significant inward rumpling takes place in the upper layer of the polar terminated surfaces in contrast with the very small relaxation (~5 pm) experimented by deeper layers, which is in agreement with the dipole reduction trend in a Tasker-type reconstruction. Nevertheless, non-polar terminations relax > 0.1 Å inwards in the second layer as well, with a small fluctuation around the bulk values predicted for the more internal layers (Table 1).

Table 1: Differences in calculated interlayer distances (Δ_{ij} in pm) relative to the same values in the bulk crystal. Positive values represent an expansion and negative values a contraction respect to the same bulk distance. Averaged values are marked with an asterisk (*).

Termination	Δ_{12}	Δ_{23}	Δ_{34}
C-polar	-14.473*	-4.879*	4.511*
C-polar Reconstr.	-12.455*	-4.619*	5.414*
C-non-polar	-14.524	-16.161	7.575
Hexagonal	-9.243	-12.188	4.399
Stripes	-8.891	-11.526	4.114

Upon relaxation, all reconstructions lower the total energy of the system with respect to the corresponding value for the polar bulk-cut relaxed C-terminated surface, in agreement with the predictions of the Tasker model for ionic materials. The calculated values of the cleavage energy E_{cleav} in Table 2 suggest that the C-non-polar termination is the most stable surface, which calculated C-C distances are in remarkable agreement with experimental values.[20,30,31] Nevertheless, the relative close cleavage energies, and hence stabilities, of the different reconstructions strongly suggest that fractions of the material surface

are likely to be covered by hexagonal and stripes motifs as these surfaces are normally prepared by annealing at high temperature. It is worth to note that all results reported are obtained considering perfect UHV conditions (absence of any gas in contact with the surface).The stability of each surface will definitely change taking into account possible adsorption, desorption or reactive processes. We will further discuss the presence of each surface as function of temperature in the next section.

The atomic charges on the surface atoms and, in particular, the difference with respect to bulk values provides information about electronic structure modifications arising from surface reconstruction. Net atomic charges have been estimated by means of the Bader analysis,[32] where the electron density associated with each topological atomic basin is integrated.[33] Note that the Bader volume is not a sphere of constant radius; due to the changes in the effective atomic radii with the oxidation state of the ion, it is dependent on the charge density. Nevertheless, one must be aware of the fact that excessive electron delocalization of standard DFT methods, arising from the self-interaction error, usually leads to an underestimation of atomic charges although trends are likely to be correct. Here, the atomic charges of surface atoms are compared to those of the corresponding bulk atoms (Table 2).

Table 1: Surface characteristic quantities calculated for each termination: cleavage energy (E_{cleav} in J m^{-2}), relaxation amount (% Relax), termination degeneracy (Ω), surface work function (ϕ in eV) and atomic charges of the uppermost C atoms (Q_C in a.u.). The value of the atomic charge for bulk carbon atoms is -2.4 *e* for all surfaces. Averaged values are marked with an asterisk.

Termination	E_{cleav}	**% Relax**	**Ω**	ϕ	Q_C
C-polar	3.355	6.6	1	4.8	-1.9
C-polar Reconstr.	3.274	8.8	1	4.9	-1.8*
C-non-polar	3.217	5.4	1	4.9	-1.9
Hexagonal	3.281	3.5	2	4.9	-1.8*
Stripes	3.262	4.1	2	4.9	-1.9*

The calculated values indicate that charge in the surface C atoms is significantly smaller than in the bulk, but with minor differences in the values corresponding to the difference surface terminations. In order to obtain additional information regarding the electronic structure of each termination, we have derived the work function (ϕ) values by subtracting the value of the Fermi energy from the electrostatic potential at the vacuum. Work function is strongly influenced by the extent of surface dipole and variation of this property cannot always be addressed to simple electrostatic arguments.[34] However, it is a global property of the surface under study, and in this case small changes resulting from the different morphologies can be expected. In fact the calculated work function values are all around ~5 eV, comparable to those reported in previous work for the polar termination.[15,16] Clearly, the similarity between calculated values ϕ does not allow us to use this property to characterise each surface motif, either theoretical or experimentally.

Statistical analysis of surface termination distribution

Experimental characterisation of the C-terminated β-Mo_2C (001) surface detected a number of structural changes during annealing processes at different temperatures.[18,,20] Thus, upon annealing the sputtered β-Mo_2C (001) between 840 and 960 K, a honeycomb motif appears as the first well-ordered structure.[19] However, it has been shown that annealing at higher temperatures leads to a change in the surface structure.[18] Further experiments have provided evidence that annealing time also modifies the surface structure.[20] The combination of both temperature and annealing time modifies the carbon coverage on the surface (θ_C), due to its segregation and C oxidation towards CO_2.[31] For instance, it was noted that the honeycomb structure changes to a c(2x4) zig-zag motif.[20]

Following previous work, we assume here that the probability of a given arrangement is described by a Boltzmann distribution and that this governs the extent of occurrence of a particular configuration at the surface.[3537] To obtain the probability distribution of the different surface motifs as a function of the temperature, we employ the calculated DFT energies in a Boltzmann-like probability (P_i) defined as:

$$P_i = \frac{\Omega_i e^{\frac{-\Delta E_i}{k_B T}}}{\sum_j \Omega_j e^{\frac{-\Delta E_j}{k_B T}}} \qquad (6)$$

where ΔE_i stands for the energy of the motif *i* with respect to the energy of C-non-polar, and Ω is the degree of degeneracy associated with each configuration (Table1). The probability of finding each surface motif (or motif surface fraction) of β-Mo_2C (001) at the annealing temperature in thermodynamic equilibrium is represented in Figure 4. Note that entropic contributions, C segregation or C reaction with oxygen are not considered. Therefore, the information from the diagram in Figure 4 has to be taken from a qualitative point of view only.

The analysis of Figure 4 reveals that the C-non-polar pattern is the most stable structure at low temperature. However, for temperatures beyond 500 K the surface area is likely to be shared with the hexagonal and the stripes motifs. Interestingly, the probability of these secondary patterns to cover the surface becomes ~ 20 % at 1000 K. Although other terminations may be present, their contribution to the total surface is negligible. In agreement with Tasker's arguments,[22] we found that non-polar surfaces are the most stable terminations for every temperature. The presence of different patterns at high temperatures agrees well with the experiments where the surfaces were annealed at ~900 K.[19] In these studies it was pointed out how the presence of each surface domain

strongly depends on the annealing temperature used, a feature nicely reproduced by the present modelling study. In fact, a limit of 1300 K was predicted to be crucial to produce the surface composition changes,[21] which is close to the inflection point of curve for the non-polar C-termination. In addition, the increment in the C/Mo ratio seen in the experiments is consistent with the presence of small domains according to the stability of the C-polar Reconstructed.

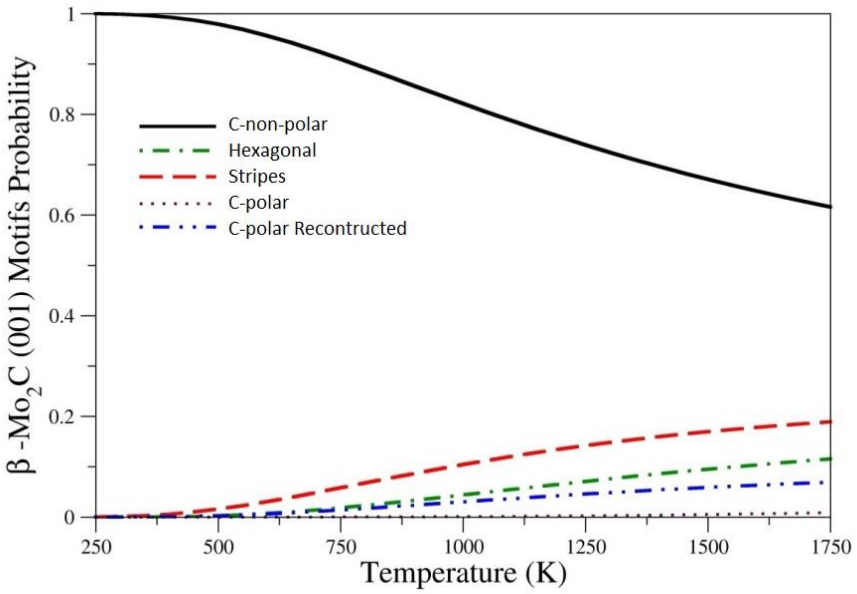

Figure 4. Probability of the different β-Mo_2C(001) C-terminations as a function of the absolute temperature. Entropic contribution has been neglected.

Surface electronic structure and simulated STM images

The electronic structure of the different surfaces can also be analysed in terms of projected density of states (pDOS) profiles. Figure 5 reports the calculated pDOS for the C non-polar surface structure. We use this surface as an example to discuss the pDOS associated with the C-terminated surface as it presents the

most important features seen in the pDOS of all terminations studied. Interestingly, there is no apparent relation between the position of Mo atoms in more external or more internal layers and their contribution to the total DOS. Some interesting features associated with the creation of the surface can be identified if we compare the surface with previously reported bulk DOS.[16] The surface pDOS profile clearly shows two peaks at about -12 and -10 eV, and a wide valence band around the Fermi level, confirming the metallic character of Mo_2C. A further analysis obtained projecting the total DOS on the Mo or C atoms belonging to a certain layer allows us to identify the contribution of surface or inner atoms to the total DOS. The surface pDOS presents an abundance of metallic states in the proximity of the Fermi level. Those states belong to sub-surface Mo layers, where states associated with carbon atoms are found at much lower energies. Such valence states are those that can be easily seen in STM experiments. This behaviour is conserved also in the bulk pDOS profile where the large majority of the valence states close to the Fermi energy are predicted to be associated with Mo 5d states and carbon states are present in much smaller quantities at higher binding energies.

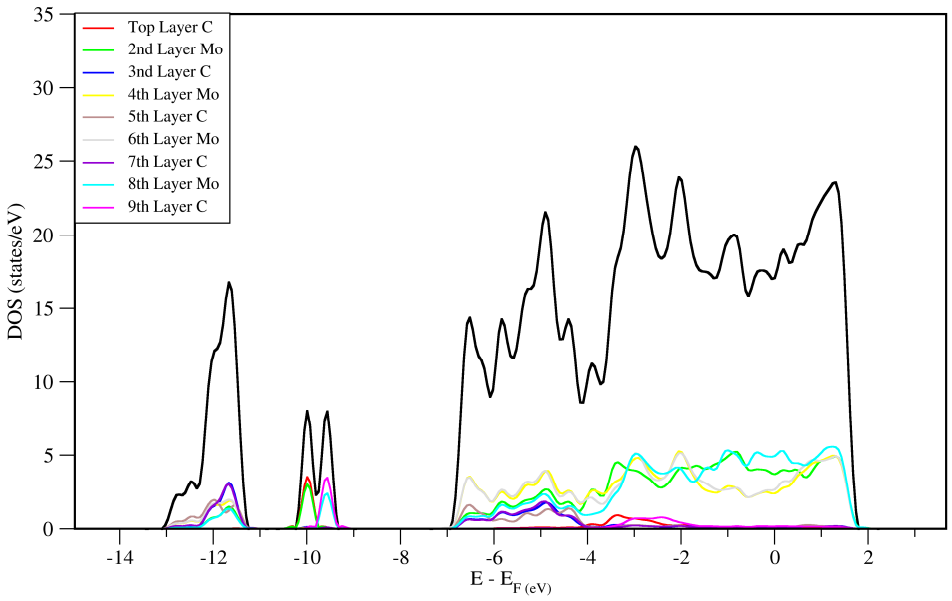

Figure 5: Projected density of states (pDOS) for the non-polar reconstruction of the C-terminated (001) surface. The profile explicitly shows the contribution of each Mo or C layer to the total DOS (displayed in black), highlighting how the large majority of the valence states are associated with Mo atoms.

The bulk DOS presents a clearly marked peak around -12 eV associated with the C 2s states and with a small contribution of Mo 5d bands. In the surface pDOS, displayed in Figure 5, the peak at -12 eV is still present, although another peak arises at about -10 eV. The former is associated with carbon atoms belonging to different layers, and with a non-negligible contribution from Mo atoms in different layers. The second peak has no contribution from carbon atoms but all states come from Mo atoms belonging to different layers. The surface pDOS profile confirms the idea of surface carbon atoms floating on a "sea" of electrons coming from Mo atoms in deeper layers of the material.[19]

The β-Mo_2C (001) surface has been characterised by scanning tunnelling microscopy (STM), showing a honeycomb structure (θ_C= 0.33 ML) with a centred carbon as a sombrero protrusion.[38] The c(2x4) zigzag pattern was also identified by Fukui et al.[19] for a carbon coverage of 0.5 ML on the surface. To further compare the proposed surface terminations with experimental findings, we have modelled the STM images for the motifs predicted to be the most stable: C-non-polar, Stripes and Hexagonal. The topographical STM images were obtained using the well-known Tersoff-Haman approach that links the potential applied between the tip of the microscope and the surface with the electron density associated with a certain energy window from the Fermi energy.[39] The simulated images in Figure 6 provide information about the spatial distribution of the valence band states in the vicinity of the Fermi energy (E_F), which is particularly useful for systems where the ad-atoms can interact with the surface in many different sites. Compared with isodensity plots, they are directly comparable with experimental STM with the advantage that the model does not suffer from external perturbations, such as the electric field of an STM

experimental tip influencing the position and orientation of species adsorbed on a surface.[40]

The STM simulation of the C-non-polar motif shows a protrusion in the centre of distorted hexagons, which is formed by low density peaks of the C atoms. The high density regions surrounding the C correspond to sub-surface Mo atoms whose states lie in the proximity of the Fermi level. In any case, it is important to note that the surface occupied states do not correspond to surface carbon, as initially suggested,[19] but are dominated by sub-surface Mo atoms. This finding is consistent with the pDOS of Figure 5. The motif we denoted as "hexagonal" shows the Mo electron density embedding C atoms corresponding to wells of low density. The intense electron density of Mo atoms largely affects C detection on the surface, strengthening the definition of C atoms floating "upon a calm sea of electrons".[19] Nevertheless, the constant current simulated STM of the Stripes motif shows high signals for Mo sites and depressions where C atoms sit, exposing clear parallel rows. Some structural relations can be seen when we compare the images obtained with the experimental data available, also assenting the inter-atomic distances reported above. The most immediate is the correspondence between calculated and experimental STM images for the "Stripe" motifs at θ_C= 0.5 ML. Here, two different types of C atoms cover the Mo sub-surface layer as demonstrated by the different height of the low density peaks seen in the simulated STM. Nevertheless, the Stripe type structures may lower the surface C coverage and evolve presumably to another non-polar structure, perhaps to the so-called honeycomb structures as previously guessed.[19]

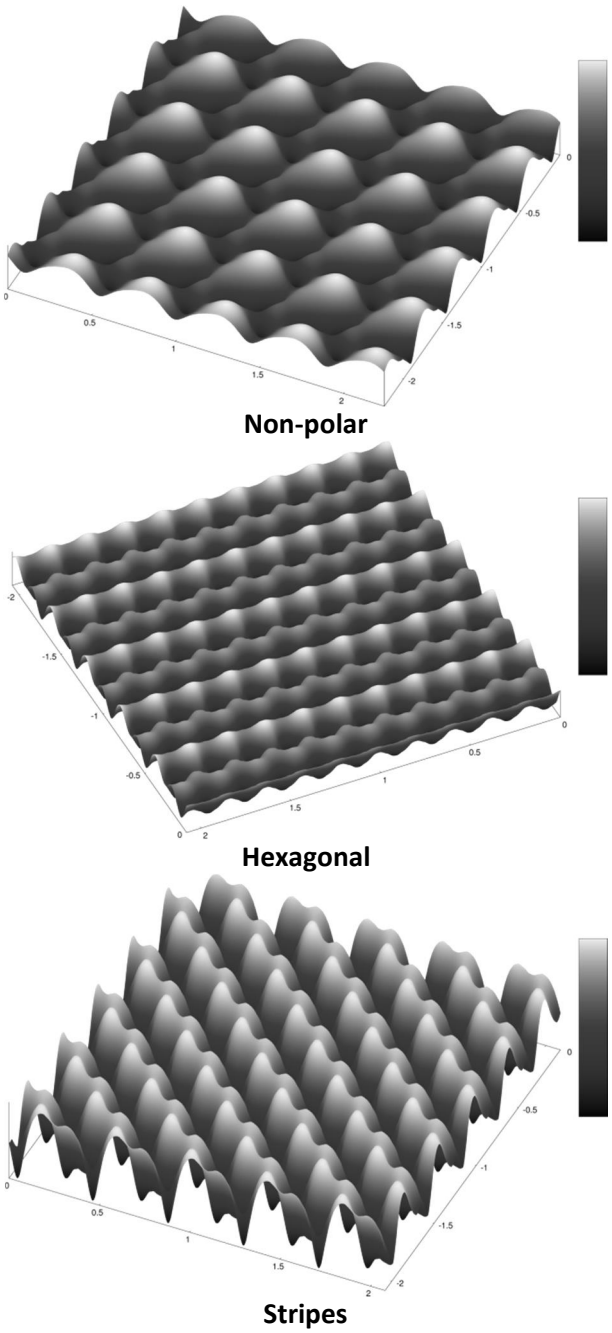

Figure 6. Simulated STM images for the three most stable C-terminations. Images were obtained displaying the electron density associated with the states between up to 0.5 eV at a constant charge density of 10^{-5} $e^{-}/Å^{3}$.

Conclusions

Periodic DFT calculations have been used to study the stability of a number of C-terminated (001) surfaces of β-Mo_2C. Models for this surface termination have been proposed, which include polar and non-polar terminations; the latter are expected to be more stable according to the Tasker classification of polar surfaces of ionic materials.[22]

Various surface properties have been derived for each termination and motif including the cleavage energy (as a measure of the surface stability), work function, Bader atomic charges and atomic structure. Although the differences between top surface atomic charges or work functions are almost negligible, the surface relaxation leads to an important rumpling on the non-polar C-terminated surfaces. Furthermore, from the cleavage energy analysis we suggest that non-polar C-terminated surfaces are the most thermodynamically stable. Nevertheless, other surfaces may be present depending on synthetic conditions favouring or hindering the formation of these surfaces.

A Boltzmann distribution derived from DFT calculated energy values has been proposed to quantify the contribution of each motif to the surface at different temperatures, highlighting that at high temperatures various surfaces may be present although the non-polar C-terminated surface is likely to be dominant. In case of extra carbon at the surface, reconstructed domains may coexist. These results provide a theoretical explanation of previous experimental results that encountered a strong dependence of surface structure on annealing temperature. In these studies, some STM images were presented and various domains identified.[19] Simulated STM images show a straightforward comparison with experiment and, in particular, simulated STM images for the Stripes models nicely compare to experimental ones obtained at θ_C= 0.5 ML, whereas the honeycomb structure is formed at different coverage and, presumably, from a non-polar C-terminated surface.

Acknowledgments

This work has been supported by the Spanish MINECO grant CTQ2012-30751 grant and, in part, by *Generalitat de Catalunya* grants 2014SGR97 and XRQTC. G.G.A. thanks the *Universitat Rovira i Virgili* for supporting his predoctoral research and the London Thomas Young Centre and the UCL Industrial Doctorate Centre for Molecular Modelling and Materials Science for funding. A.R. is grateful to the Ramsay Memorial Trust and University College London for the provision of a Ramsay Fellowship. F.I. acknowledges additional support through the ICREA Academia award for excellence in research. Computational time at the MARENOSTRUM supercomputer has been generously provided by the Barcelona Supercomputing Centre through a grant from *Red Española de Supercomputación*.

References

1 J. S. Lee, S. T. Oyama, M. Boudart, J. Catal., 1987, 106, 125.

2 A. J. Medford, A. Vojvodic, F. Studt, F. Abild-Pedersen, J. K. Nørskov, J. Catal., 2012, 290, 108.

3 H. Tominaga, M. Nagai, Appl. Catal. A Gen. 2005, 282, 5.

4 M. D. Porosoff, X. Yang, J. A. Boscoboinik, J. G. Chen, Angew. Chem. Int. Ed., 2014, 53, 6705.

5 W. Yu, M. Salciccioli, K. Xiong, M. A. Barteau, D. G. Vlachos, J. G. Chen, ACS Catal., 2014, 4, 1409.

6 J. Patt, D. J. Moon, C. Phillips, L. Thompson, Catal. Lett., 2000, 65, 193.

7 H. Tominaga, M. Nagai, Appl. Catal. A Gen. 2008, 343, 95.

8 H. Tominaga, M. Nagai, Appl. Catal. A Gen. 2007, 328, 35.

9 J. A. Rodriguez, L. Feria, T. Jirsak, Y. Takahashi, K. Nakamura, F. Illas, J. Am. Chem. Soc., 2010, 132, 3177.

10 E. Florez, T. Gomez, P. Liu, J. A. Rodriguez, F. Illas, ChemCatChem, 2010, 2, 1219.

11 J. A. Rodriguez, P. Liu, F. Viñes, F. Illas, Y. Takahashi, K. Nakamura, Angew. Chem. Int. Ed., 2008, 47, 6685.

12 F. Feria, J. A. Rodriguez, T. Jirsak, F. Illas, J. Catal., 2011, 279, 352.

13 J. A. Rodriguez, F. Illas, Phys. Chem. Chem. Phys., 2012, 14, 427.

14 G. W. Wang, J. A. Schaidle, M. B. Katz, Y. Li, X. Q. Pan, L. T. Thompson, J. Catal., 2013, 304, 92.

15 X.-R. Shi, S. –G. Wang, H. Wang, C. –M. Deng, Z. Qin, J. Wang, Surf. Sci., 2009, 603, 852.

16 J. R. S. Politi, F. Viñes, J. A. Rodriguez, F. Illas, Phys. Chem. Chem. Phys., 2013, 15, 12617.

17 P. Liu, J. A. Rodriguez, T. Asakura, J. Gomes, K. Nakamura, J. Phys. Chem. B, 2005, 109, 4575.

18 R.-L. Lo, K. Fukui, S. Otani, S. T. Oyama, Y. Iwasawa, Jpn. J. Appl. Phys., 1999, 38, 3813.

19 K. Fukui, R. L. Lo, S. Otani, Y.Iwasawa, Chem. Phys. Lett., 2000, 325, 275.

20 R. L. Lo, K. Fukui, S. Otani, Y. Iwasawa, Surf. Sci., 1999, 440, L857.

21 T. P. St. Clair, S. T. Oyama, D. F.Cox, S. Otani, Y. Ishizawa, R.-L. Lo, K. Fukui Y. Iwasawa, Surf. Sci., 1999, 426, 187.

22 P. W. Tasker, J. Phys. C: Solid State Phys., 1979, 12, 4977.

23 P. E. Bloch, Phys. Rev. B, 1994, 50, 17953.

24 G. Kresse, D. Joubert, Phys. Rev. B, 1999, 59, 1758.

25 J. P. Perdew, K. Burke, M. Ernzerhof, Phys. Rev. Lett., 1996, 77, 3865.

26 J. Monkhorst, J. D. Pack,. Phys. Rev. B, 1976, 13, 5188.

27 G. Kresse, J. Furthmuller, Phys. Rev. B, 1996, 54, 11169.

28 S. Otani, Y. Shigeki, J. Cryst. Growth, 1995, 154, 202.

29 G. W. Watson, E. T. Kelsey, N. H. de Leeuw, D. J. Harris, S.C. Parker, J. Chem. Soc.: Faraday Trans., 1996, 92, 433.

30 A. T. Santhanam, in: S.T. Oyama (Ed.), The Chemistry of Transition Metal Carbides and Nitrides, Blackie, Glasgow, 1996, p. 53.

31 Sr. T. C. Wallace, D. P. Butt., in: S.T. Oyama (Ed.), The Chemistry of Transition Metal Carbides and Nitrides, Blackie, Glasgow, 1996, p. 28.

32 R. F. W. Bader, Atoms in Molecules: A Quantum Theory, Oxford Science, Oxford, U.K., 1990.

33 G. Henkelman, A. Arnaldsson, H. Jonsson, Comput. Mater. Sci., 2006, 36, 354.

34 P. S. Bagus, D. Käfer, G .Witte, C. Wöll, Phys. Rev. Lett., 2008, 100, 126101.

35 R. Grau-Crespo, N. H. de Leeuw, C. R. A. Catlow, Chem. Mater., 2004, 16, 1954.

36 R. Grau-Crespo, A. G. Peralta, A. R. Ruiz-Salvador, A. Gomez, R. Lopez-Cordero, Phys. Chem. Chem. Phys., 2000, 2, 5716.

37 S. Benny, R. Grau-Crespo, N. H. de Leeuw, Phys. Chem. Chem. Phys., 2009, 11, 808.

38 P. Sautet, Surf. Sci., 1997, 374, 406.

39 J. Tersoff, D. R. Hamann, Phys. Rev. B, 1985, 31, 805.

40 Th. Dretschkow, A. S. Dakkouri, Th. Wandlowski, Langmuir, 1997, 13, 2843.

Chapter 8

Summary and concluding remarks

In this thesis we have investigated several TMC systems. In some case we focused on the adsorption and reactivity of molecules on surfaces, in others on structural properties of carbides and on their interaction with noble metal atoms.

Adsorption of molecules

Throughout this thesis adsorption of several molecules (CO, CO_2, H_2, H_2O) was studied on various TMC and noble metal clusters supported thereon. In a first moment we concentrated just on carbon monoxide. We considered the extended (001) surface of TiC but also terraces, monatomic steps and kink defective sites. In all cases the surface carbon atoms demonstrated to be favored sites for the adsorption and not simple spectators.

Despite the characteristic high hardness of TMC materials, the surface is largely distorted upon adsorption. Our DFT study predicts that the underlying surface C atom is pulled out of the surface plane of about 0.5 Å. This strong interaction destabilizes the system influencing the calculated adsorption energy. For lower coverage the distortion energy associated to the new C-C double bonds formed is reduced because a smaller number of molecules are adsorbed on the surface and so the adsorption energy value for low coverage situations is converged using big supercell models.

Results obtained[1] pointed out the importance of using reliable models that well describe the surface relaxation upon adsorption. Our periodic slab model where the uppermost 2 layers are fully relaxed and the bottom 2 are fixed to the optimized bulk position demonstrated to offer accurate results for both adsorption energies and geometries.

Adsorption on defective sites[2] resulted in a confirmation of the surface carbons as the preferred CO adsorption sites on TiC. The lower coordination of the adsorptive atoms corresponds with an increment of the bond strength.

Trends obtained with the highly computational demanding extended models used to study adsorption on edge or kink sites where qualitatively reproduced with the cheaper finite nanocube model. This opens to a systematic study of the effect of the reduced coordination on the adsorptive properties of other rock salt TMCs.

Reactivity of adsorbed molecules

The important information achieved about CO-TiC (001) interaction was used to set up a consistent methodology to study the reactivity of adsorbed molecules on clean TiC (001) surface and on two gold clusters models, Au_4 and Au_6, adsorbed on TiC support.

The relaxation of the TiC substrate is needed to obtain reliable results about adsorption energies and geometries. Studying the reactivity of *syngas*,[3] a mixture of CO and H_2, on the clean (001) surface such relaxation demonstrated to be crucial to properly identify intermediates and transition state structures. However the energy barriers calculated for methane or formaldehyde formation where by far too high and those processes are unviable on the clean support.

Gold clusters supported by TiC (001) improve the catalytic activity of the system. In fact, the calculated reaction barrier for the first hydrogenation of CO is reduced on the bigger Au_6 cluster respect to the clean support or the smaller Au_4 cluster by consequence of both electronic and structural features, but however the reaction continues to be highly hindered. Despite of these results CO_2 activation and hydrogenation is predicted to be fast on the Au_4 system.[4] Ab initio estimation of the reaction rates for the Water Gas Shift Reaction at industrial conditions was used to compare results obtained for the Au_4/TiC (001) model catalyst with experiments confirming the high catalytic activity found. These results point out the high catalytic activity of small gold nanoclusters and their activation upon interaction with TiC but also spread light on some possible controversial results obtained. Lack of catalytic activity of the Au_4/TiC (001) system toward CO hydrogenation does not have to be imputed just to the heterogeneous catalyst but to the interaction with the reactants that causes a structural hindering impeding the reaction.

Interaction with noble metals

Information obtained up to now confirmed that the interaction with TMC activates noble metal nanoparticles adsorbed thereon. In particular Ni, Cu and Au clusters are strongly perturbed upon adsorption resulting in extremely active catalysts.[5,6]

For this reason, our research continued focusing on the interaction of those atoms with another rock–salt TMC: the δ phase of the molybdenum carbide catalyst. Such phase is predicted to be metastable although the (001) surface has the lowest cleavage energy of all low index surfaces commonly considered when studying molybdenum carbide materials.[7,8] This study showed how the interaction is stronger for lowest coverage considered but, most important, that the relaxation of the surface is needed to well describe low coverage adsorption. Adsorption energies calculated are in the order of 2 - 5.5 eV, increasing when reducing the coverage and in the order Au < Cu < Ni. Indeed adsorption causes a strong distortion of the underlying surface, proved by the increment of about 25 % of the hollow area where noble metal atoms adsorb. The calculated *d* band center shifts to more positive energies for higher coverage inferring an increment of the catalytic activity. For all coverage considered the activity is predicted to increase in the order Ni > Cu > Au. These predictions agree with recent experiments performed using titanium carbide as support for small Au, Cu or Ni clusters.[5]

Structural investigation of β-Mo_2C (001) C-terminated morphology

The experimental confirmation of our theoretical results obtained for adsorption, reactivity and catalytic activity trends strengths the reliability in the computational models used. It opened a way for the prediction of possible morphologies of the (001) surface of Mo_2C, an important less studied carbide whose interesting application are stimulating recent investigations.[9,10]

When studying the catalytic activity of small metal nanoclusters adsorbed on any support the first necessary step is the determination of the structure of the surface under study. In this part of our research we studied the applicability of the classical concepts developed by Tasker for oxide material to transition metal carbides.[11] Following classical electrostatics the polar low index surfaces of TMC

should undergo reconstruction in order to minimize the finite dipole perpendicular to the surface due to the polarity of the TM-C bond.

Our study[12] guessed possible non-polar reconstruction for the (001) surface of Mo_2C focusing on the calculated cleavage energy, proportional to the stability of each termination considered. In these sense smaller cleavage energies corresponds to more stable surface structures.

All non-polar reconstructions decreases the calculated cleavage energy, confirming the applicability of Tasker's concepts to TMCs. Boltzmann distribution was then used to predict the abundance of each guessed termination as function of the temperature. At low temperature the non-polar reconstruction is by far the most abundant of the surface where for higher temperature it is expected the presence of others non-polar reconstructed domains together with a small fraction covered by the polar C-terminated surface.

References

1 G. G. Asara, L. Feria, E. Florez, J. M. Ricart, P. Liu, J. A. Rodriguez, F. Illas, J. Phys. Chem. C, 2011, 115, 22495.

2 B. P. Mant, G. G. Asara, J. A. Anderson, N. Homs, P. Ramírez de la Piscina, S. Rodríguez, J. M. Ricart, F. Illas, Surf. Sci., 2013, 613, 63.

3 G. G. Asara, J. M. Ricart, J. A. Rodriguez, F. Illas, in preparation.

4 J. A. Rodriguez, P. J. Ramírez, G. G. Asara, F. Viñes, J. Evans, P. Liu, J. M. Ricart, F. Illas, submitted.

5 J. A. Rodriguez, J. Evans, L. Feria, A. B. Vidal, P. Liu, K. Nakamura, F. Illas, J. Cat., 2013, 307, 162.

6 A. B. Vidal, L. Feria, J. Evans, Y. Takahashi, P. Liu, K. Nakamura, F. Illas, J. A. Rodriguez, J. Phys. Chem. Lett., 2012, 3, 2275.

7 J. R. S. Politi, F. Vines, J. A. Rodriguez, F. Illas, Phys. Chem. Chem. Phys., 2013, 15, 12617.

8 X.-R. Shi, S.-G. Wang, H. Wang, C.-M Deng, Z. Qin, J. Wang, Surf. Sci., 2009, 603, 852.

9 Yu, W.; Salciccioli, M.; Xiong, K.; Barteau, M. A.; Vlachos, D. G.; Chen, J. G., ACS Catal., 2014, 4, 1409.

10 J. Patt, D. J. Moon, C. Phillips, L. Thompson, Catal. Lett., 2000, 65, 193.

11 P. W. Tasker, J. Phys. C: Solid State Phys., 1979, 12, 4977.

12 G. G. Asara, A. Roldan, J. M. Ricart, J. A. Rodriguez, F. Illas, N. H. de Leeuw, submitted.

Gian Giacomo Asara

List of publications[1]

Thesis related papers:

Gian Giacomo Asara, Leticia Feria, Elizabeth Florez, Josep M. Ricart, Ping Liu, José A. Rodriguez, Francesc Illas, Theoretical Study of the Interaction of CO on TiC (001) and Au Nanoparticles Supported on TiC (001): Probing the Nature of the Au/TiC Interface., The Journal of Physical Chemistry C, 2011, 115, 22495–22504.

Barry P. Mant, Gian Giacomo Asara, James A. Anderson, Narcis Homs, Pilar Ramírez de la Piscina, Sònia Rodríguez, Josep M. Ricart, Francesc Illas, Theoretical and experimental study of the interaction of CO on TiC surfaces: Regular versus low coordinated sites., Surface Science, 2013, 613, 63–73.

Gian Giacomo Asara, Francesc Viñes, Josep M. Ricart, José A. Rodriguez, Francesc Illas, When reconstruction comes around: Ni, Cu, and Au adatoms on δ-MoC (001), Surface Science, 2014, 624, 32–36.

Gian Giacomo Asara, Alberto Roldan, Josep M. Ricart, Jose A. Rodriguez, Francesc Illas, Nora H. de Leeuw, New Insights into the Structure of the C-Terminated β-Mo_2C (001) Surface from First-Principles Calculations, The Journal of Physical Chemistry C, 2014, 118, 19224−19231.

José A. Rodriguez, Pedro J. Ramirez, Gian Giacomo Asara, Francesc Viñes, Jaime Evans, Ping Liu, Josep M. Ricart, Francesc Illas, Charge Polarization at Au–TiC Interface and the Generation of Highly Active and Selective Catalysts for the Low-Temperature Water–Gas Shift Reaction, Angewandte Chemie International Edition, 2014, 53, 1–6.

Gian Giacomo Asara, Josep M. Ricart, Jose A. Rodriguez, Francesc Illas, Unraveling of the unique pathway of CO_2 reduction on novel Au-TiC catalyst, in preparation.

Gian Giacomo Asara, Alberto Roldan, Josep M. Ricart, Jose A. Rodriguez, Francesc Illas, Nora H. de Leeuw, Theoretical study of synthetic gas reactivity on Au, Cu and Ni atoms supported by δ-MoC (001), in preparation.

Other papers:

Gian Giacomo Asara, April D. Lewoczko, Andrei Burnin, Joseph J. Bel Bruno, Stefan T. Bromley, Interplay between Magnetism and Magic-ness in Nanoclusters, The Journal of Physical Chemistry C, 2012, 116, 20625–20632.

Courses and conferences[1]

Chemical bonding in real space. Quantum Chemical Bonding and beyond. Universitat Rovira i Virgili, 2013.

15th International Conference on Theoretical Aspects of Catalysis (ICTAC15). University College London, 2014.

Theoretical Modellng of Materials - WATOC 2011 Satellite. Universitat de Barcelona.

New Trends of Computational Chemistry for Industry Application, 2011, 2012, 2013, Universitat de Barcelona.

AFM Microscopy. PARALAB - Independent Coursework, Barcelona, 2013.

During the Master in Theoretical and Computational Chemistry (2010-2011) and the following three years of Ph. D. I attended group seminars and conferences organized by both the Quantum Chemistry Group (QCG) of Universitat Rovira i Virgili (URV) and the Computational Material Science Laboratory (CMSL) of Universitat de Barcelona (UB). I also attended the annual meetings of the Reference Network on Theoretical and Computational Chemistry of Catalonia.

Research abroad

Between September 2013 and January 2014 I joined the group of the Professor Nora H. de Leeuw at the Department of Chemistry, UCL, in London. Our collaboration resulted in one published paper [JPCC, 2014, 118, 19224–19231] about the non-polar reconstruction of C-terminated β-Mo_2C (001) surface; another research article, about CO hydrogenation on noble metal atoms supported by δ-MoC (001), will be soon submitted for publication.

[1] Updated to September, 9th 2014

Acknowledgments

Firstly I would like to thank Prof. Josep Manel Ricart Pla and Prof. Francesc Illas Riera for the help and the support they gave me during the last four years. With different times and intensities they showed me how research works! Focus my work to obtain interesting and valuable results, nicely report it and finally resume it in an effective way.

Then I want to acknowledge the Universitat Rovira i Virgili for the Predoctoral Grant that allowed me to live and work here in Catalunya during the last four years. I like to thank all professors of the Quantum Chemistry Group of Universitat Rovira i Virgili and of the Computational Material Science Laboratory of Universitat de Barcelona.

Last but not least, I would like to thank my whole big family spread out around Europe, who helps and supports me every day, and all the people and colleagues who shared with me offices, laughs and processors.

Obviamente las personas que he conocido y que me han ayudado en estos casi cinco años son muchas, y aunque seguramente me olvidaré de alguien vale la pena intentar de agradecerlos todos y cada uno, y para hacer esto de la mejor manera ya me tocó cambiar idioma...

A mis jefes les debo mucho más que las dos líneas que escribí un poquito más arriba en inglés.

Xino confió en mí desde el principio, durante la tesis cuando las cosas no iban bien y los resultados no llegaban, y también cuando las cosas iban mejor, tanto que de estudiante erasmus recién llegado me ayudó a hacerme todo un doctor. A Ricart le reconozco y le agradezco el tiempo que consiguió dedicarme y encontrar en medio de los miles de compromisos que tiene. De haberme demostrado en muchas, muchísimas ocasiones que confiaba en mi seriedad como trabajador (cosa no siempre fácil) y en mis capacidades como científico. Y por último, por haberme ayudado tanto en esta última fase de redacción de la tesis.

A Stefan Bromley le agradezco todas las discusiones que tuvimos, de ciencia como de muchas otras cosas, pero también las comidas, las cenas y las fiestas, y el hecho de haber sido el primer profesor con que trabajé aquí en España. A Iberio Moreira de haberme ayudado de manera completamente desinteresada en esta fase final de la tesis, corrigiéndome y enseñandome. A todos los profesores del QCG por haberme ayudado y escuchado a lo largo de todos estos años

Toca empezar con los compañeros de la uni. De Alberto, Xavi, Marçal, Albert, Nuria, Fransis, Jess, Pablito, Mire, Eva, Marçal, Albert, Idoia, Miriam, Sergi V., y muchos otros que simplemente pasaron por aquí o por allí aprendí mucho, de ciencia y de vida. Con ellos eché muchas risas y siempre serán parte de los buenos recuerdos que me llevaré de Catalunya.

A los míos, Pablosan, Uri, Marc, Arnau, la verdad es que no sé qué decir más que parte de esta tesis es vuestra también, tan solo por aguantarme las locuras, los nervios, las dudas y los agobios que se

pusieron en medio de las tantos buenos momentos que pasamos juntos, para ayudarme cuando me sentía solo y el trabajo iba mal. Al Pablo además para haberme acogido tantas veces demostrando ser uno de los mejores compañeros de piso de los muchos que tuve. A Sergey, Pedro y Melchor, con que también compartí muchas risas, tanta ciencia y buenos momentos, pues les auguro de acabar la tesis pronto y bien!

Y luego me gusta saludar y agradecer a los jóvenes que jóvenes no son, sino que simplemente empezaron su investigación un(os) año(s) después. Sergi S., Laura, Jason, Magda, Diego, Sergi P., Mariano y Josep, y a las recién llegadas Noe y Almu. A los primeros que el doctorado, la música, el deporte y la vida siga igual o mejor de cómo ha ido hasta ahora, a las segundas de que el doctorado que acaban de empezar sea ruidoso divertido e interesante por lo menos como ha sido el mío. A todos sé que debería haberle dedicado más tiempo. Aun así os agradezco los ratos que pasamos juntos.

Obviamente también hay vida a fuera de la universidad y también mucha gente que, conscientemente o no, me ha ayudado en estos años.

A ese gordo con que comparto piso hace mucho tiempo, Javier Rincón, y a toda su fantástica familia que me ha acogido aquí y que tantas veces sustituyeron la familia que he dejado en Cerdeña, y con ellos toda la manada de sardos, napolitanos, colombianos de pasaporte o adquiridos, mexicanos catalanes, italianos, españoles y un marroquí, con que sigo pasando tanto buenos momentos aquí.

Luego hay más personas a que agradecerle infinitas ayudas.

I miei amici e colleghi di universitá e dottorato “virtuale” Andrea G. e Salvatore C. Senza di loro molte cose in questi quattro anni sarebbero state enormemente piu difficili. A loro devo molta parte della mia passione per la scienza, del mio ~~amore~~ odio per Linux, e anche parte della scelta di fare il dottorato. Dilly in questi casi rientra nei ringraziamenti perchè è troppo toga e sempre presente, qui come in terra inglesa. A Valo e Sergio ringrazio i falliti tentativi di raddrizzarmi sulle strade della vita e sulle sedie del soggiorno, le interminabili discussioni e le ancor piu interminabili mangiate e suonate.

Da ringraziare mancano ormai solo i miei genitori, fratello, sorelle, cugini, cugine, zii, zie,cognati e cognate che mi hanno sempre ricordato quanto importante fosse quello che sto fancendo e quanto sia necessario cercare di farlo al meglio.